Fall 2014

Intranuclear strain measured by iterative warping in cells under mechanical and osmotic stress

Jonathan T Henderson
Purdue University

Graduate School Form 30
(Updated 11/20/2014)

PURDUE UNIVERSITY
GRADUATE SCHOOL
Thesis/Dissertation Acceptance

This is to certify that the thesis/dissertation prepared

By Jonathan T. Henderson

Entitled
Intranuclear strain measured by iterative warping in cells under mechanical and osmotic stress

For the degree of Doctor of Philosophy

Is approved by the final examining committee:

Corey Neu

Alexander Veress

Joseph Wallace

Young Kim

Sophie Lelievre

To the best of my knowledge and as understood by the student in the Thesis/Dissertation Agreement, Publication Delay, and Certification/Disclaimer (Graduate School Form 32), this thesis/dissertation adheres to the provisions of Purdue University's "Policy on Integrity in Research" and the use of copyrighted material.

Approved by Major Professor(s): Corey Neu

Approved by: George R. Wodicka 11/25/2014

Head of the Department Graduate Program Date

INTRANUCLEAR STRAIN MEASURED BY ITERATIVE WARPING IN CELLS UNDER MECHANICAL AND OSMOTIC STRESS

A Dissertation

Submitted to the Faculty

of

Purdue University

by

Jonathan T. Henderson

In Partial Fulfillment of the

Requirements for the Degree

of

Doctor of Philosophy

December 2014

Purdue University

West Lafayette, Indiana

For my wife and kids
and in loving memory of Doyle Dean Henderson –
father and friend.

ACKNOWLEDGEMENTS

The race is won more often by perseverance than by pure genius. This is a quote that I found one late night on the confocal microscope that was hidden behind a taped up sign that fell down. My motivation and perseverance is not mine alone but provided by so many. First, Corey – thank you for your guidance through this discovery process. Thank you for sending some of my images across the county to Alex to see if warping could be used. Alex—thank you for your tutoring and many skype calls to discuss warping. Without your advice and knowledge this dissertation would not be possible. Many thanks to my committee members: Young Kim, Joey Wallace, and Sophie Lelievre for their conversations and guiding comments. Thanks to the Weldon staff that have been so kind to me and my family. For the treats they provide to my kids when they visit dad at work. Thanks to my lab mates past and present. Your comradery has made graduate school and the lab bearable when everything goes wrong. Thanks to the third floor late nighters that became my family when mine left for the summer. Your presence on the third floor in the early morning hours made the madness of long hours fun and competitive. My deepest thanks go to my partner in this race of life, my wonderful wife Jessica.

PREFACE

This dissertation includes several chapters that have already been published in or are in final preparation for submission in peer-reviewed journals. Chapter 2 is based upon the published book chapter in CRC Press *Handbook of Imaging in Biological Mechanics*[1]. Chapter 3 is an edited version of the already published research paper in the *Biophysical Journal*[2]. Chapters 4, 5, and 6 are manuscripts that are under final preparation. Additional information that has been added for clarity in the chapters that have already published is italicized.

TABLE OF CONTENTS

Page

Page

ABSTRACT

Henderson, Jonathan T. Ph.D., Purdue University, December 2014. Intranuclear strain measured by iterative warping in cells under mechanical and osmotic stress. Major Professor: Corey Neu.

The nucleus is a membrane bound organelle and regulation center for gene expression in the cell. Mechanical forces transfer to the nucleus directly and indirectly through specific cellular cytoskeletal structures and pathways. There is increasing evidence that the transferred forces to the nucleus orchestrate gene expression activity. Methods to characterize nuclear mechanics typically study isolated cells or cells embedded in 3D gel matrices. Often report only aspect ratio and volume changes, measures that oversimplify the inherent complexity of internal strain patterns. This presents technical challenges to simultaneously observe small scale nuclear mechanics and gene expression levels inside the nuclei of cells embedded in their native extracellular environment. Therefore, a hybrid imaging and model based image registration technique has been developed to enabled us to explore links between biomechanical and biochemical signaling within individual cells. The hybrid technique uses an iterative warping deformable image registration to measure intranuclear strain fields that are correlated to nuclear structures. Three cell mechanics methods were developed to examine the mechanical response of the nucleus under different mechanical conditions. 1) Strain transfer from tissue to nuclei in a cartilage tissue deformation model paired with nascent RNA expression, 2) strain transfer to the nucleus with different cell types on a stretchable membrane, and 3) force traction microscopy of cells during osmotic stress. Intranuclear strain fields provide spatial details of the nucleus that when paired with single cell biochemical assays will provide insight into how mechanical forces transferred to the nucleus influence gene expression.

CHAPTER 1. MOTIVATION FOR MEASURING INTRANUCLEAR MECHANICS

The motivation for the work in this dissertation is to further explore the shifting paradigm that the nucleus is a mechanosensor and not just the large inert abstract object that is counter stained in cell images to provide contrast. To discover new mechanisms of how the nucleus is a mechanosensor new measurement techniques are needed to measure such small mechanics within the nucleus. Hallmark papers nearly two decades ago have shown that the nucleus is deformed when the extracellular matrix around it is deformed[3,4]. This was state of the art technology using new confocal microscopy to measure 3D nuclear volumes. The nuclear mechanics were measured as change in aspect ratios and volumes and have been since. Much has been discovered about the connectivity of the nucleus through the cytoskeleton to the surrounding matrix. Through this mechanical linkage mechanical cues are transferred very quickly to the nucleus[5]. It is thought that these cues can alter the physical location of the chromatin regions, thereby regulating which genes are expressed. An influential paper in the field of cell mechanics discovered that mechanical cues can influence not just cell and nuclear shape but can reprogram cells to change their phenotype based on matrix rigidity[6]. In spite of all the cell mechanistic advances, the state of the art for measuring the nucleus has not changed, but is still to measure the change in aspect ratio and area. Such antiquated measurements can be made by hand with images and a ruler. They provide no spatial information concerning how mechanical forces influence the nuclear structures and gene expression. With the advances in digital image analysis and mechanical modeling, deformable image registration (DIR) techniques have been developed to measure tissue mechanics in the brain and cardiovascular tissues[7,8].

The significant advancement that this dissertation work has provided to the cell/nuclear mechanics field is an accurate intranuclear measurement technique. Based off deformable

image registration, iterative warping was developed to measure intranuclear strain fields of cell nuclei that are deformed. Briefly, the iterative warping technique uses a 3D mesh of the undeformed nucleus image and warps the mesh to register the undeformed image with the deformed image. This is how DIR works but the problem is that local minima can be found when deforming the mesh causing false magnitudes of deformation to be reported. To find the best registration, iterative warping looks for a global minimum in the registration process by varying the stiffness of the mesh and other warping parameters. Iterative warping was validated with a known forward finite element analysis and is discussed at length in chapter 4.

To investigate how intranuclear mechanics of cells are influenced under different mechanical stimuli, several traditional cell mechanics experiments were performed. The different mechanical experiments will be presented in chronological order starting with chapter three. Chapter two is a background of the different nuclear and cell mechanics techniques. Chapter three is the cartilage tissue explant shear experiments where the nuclei are deformed when the tissue is deformed. A biological measurement of nascent RNA was measured and spatially correlated to the intranuclear mechanics. The fourth chapter is a more detailed explanation of the validation of the iterative warping. The fifth chapter is with cells attached to a stretchable substrate and the intranuclear mechanics are measured along with the strain transfer ratio, which increased from passage zero to passage four chondrocytes. To conclude with the sixth chapter a non-mechanical stimulus was used to deform the nucleus. Hyperosmotic challenge causes the cell and nucleus to shrink. To understand the how chemical and mechanical interactions can influence the nuclear dynamics during osmotic loading, cell-substrate adhesion fields and intranuclear strain maps were measured simultaneously. The validation and verification that iterative warping is a meaningful measurement tool was demonstrated by measuring high resolution intranuclear mechanics in three cell mechanics experiments that could not have been resolved with contemporary geometric measurements that are antiquated.

CHAPTER 2. INTRNAUCLEAR MEASURMENT OF DEFORMATION IN SINGLE CELLS

This chapter is primarily a reproduction of a chapter in the book CRC press Handbook of Imaging in Biological Mechanics. A copy of the article is located in the Publications section for reference.

2.1 Abstract

Nuclear mechanics play a pivotal role in cell survival and gene expression. Mechanical stimulation of the cell and nucleus helps to regulate specific mechanotransduction pathways that aid in cell homeostasis. This chapter describes current and emerging methodologies that are used to study nuclear mechanics, and the subsequent mechano-biochemical response, at the single cell level. We highlight a hybrid method based on confocal microscopy and hyperelastic warping, recently developed to measure intranuclear mechanics and newly synthesized RNAs, within individual nuclei maintained in cultured tissue explants. Spatial and temporal resolutions are competing factors in the design of methods to study nuclear mechanics and mechanobiology, and have thus far inhibited insight into specific nuclear mechanobiology mechanisms in the analysis of single cells. We discuss the implementation of methods to measure nuclear mechanics, as well as their potential to increase understanding of diseases involved in compromised nuclear structures, including laminopathies.

2.2 Introduction

Diseases such as osteoarthritis, laminopathies, and specific cancers are shown to have compromised nuclear mechanics, potentially interrupting normal mechanobiological processes and homeostasis, and providing an origin point for disease progression[9-12]. As a specific example, osteoarthritis (OA) of cartilage and articulating joints has a multifactorial etiology resulting in part from a mechanical and biochemical imbalance in

the tissue. Cartilage degradation causes an altered micromechanical environment, altering expression of degrading enzymes that exacerbate the disease state[13]. Alternatively, laminopathies compromise the rigidity of the nuclear envelope and are believed to be the cause of clinical symptoms such as premature ageing and muscular dystrophy. Cancer cells actively alter their nuclear stiffness, aiding to cell mobility to further facilitate metastasis[11,14]. Pluripotent cells alter their nuclear structure and stiffness prior to cell lineage commitment [15]. As stated, differing mechanical environments, degrading nuclear, cellular, and extracellular structures, and actively altered nuclear mechanics contribute to several different disease states. To better understand healthy tissues, and changes following disease, an understanding of nuclear mechanics, and relationships to gene expression, is important in determining how applied mechanical forces to tissues and cells influence individual cell nuclei.

The nucleus is largely occupied by chromatin, dynamic structures that are influenced by many chemical and mechanical signals[16,17]. Chromatin itself is a hierarchical structure composed of DNA sequences wrapped around histones to form nucleosomes, which are then further packed together to from chromatin structures. Within the nucleus, chromatin is often classified as heterochromatin, where tightly packed chromatin structures are thought to be areas of relatively silenced gene expression, or euchromatin, where a lower density of chromatin structures exhibit higher levels of gene expression. Gene expression is altered by nuclear receptors, second messengers, and other chemical cascade signaling that is triggered from chemical binding to cellular receptors. Recently, mechanoregulation of gene expression has been hypothesized to work in parallel with chemical signaling, with direct physical altering of the accessibility of DNA regions to regulate transcription activity[18,19].

Several methodologies have recently been developed to measure the nuclear mechanics under different experimental conditions and to identify the role of nuclear architectural-mediated mechanoregulation of gene expression. Methods to measure nuclear mechanics include: 1) chromatin compaction measured via fluorescence anisotropy, 2) material properties (i.e. moduli) measured by micropipette aspiration or nanoindentation, 3) bulk

morphological deformations measured by changes in nuclear aspect ratios and/or volume, and 4) strain fields measured by texture correlation or deformable image registration using hyperelastic warping (Table 2.1). Understanding the limitations and strengths of each method will help researchers determine the method that is best suited for intended experiment needs and objectives. This chapter will cover different methodologies that are used to investigate intranuclear mechanoregulation, with special attention paid to the new implementation of deformable image registration using hyperelastic warping to measure intranuclear mechanics concurrently with single cell nascent RNA expression.

2.3 The Deformed Nucleus

2.3.1 Connecting the nucleus to the cell and extracellular matrix

The nucleus is a distinct structure inside the cell that is structurally connected through cytoskeletal components to the extracellular matrix (ECM). Among different tissue and cell types, the structural configurations linking the nucleus to the extracellular environment can be very unique. In this chapter, we will largely focus on the primary cell type (chondrocyte) found in cartilage, a load-bearing tissue with significant disease relevance [20,21]. In the chondrocyte, there are multiple structural elements that connect the chondrocyte nucleus to the ECM (Figure 2.1). The cell is anchored to the ECM with cell membrane proteins (e.g. integrins and CD44), which bind to collagen and proteoglycans. These anchoring transmembrane proteins are associated with intracellular cytoskeletal components such as actin, intermediate filaments, and microtubules. The microtubules interact with the endoplasmic reticulum (ER), which is continuous with the outer nuclear membrane. The microtubules, along with other cytoskeleton components are also connected to the nucleus through a group of nuclear transmembrane proteins called the Linker of Nucleoskeleton and Cytoskeleton complex (LINC). These structural connections from the ECM to the nucleus provide a mechanism for stress and strain to directly transfer to the nucleus when applied at relatively distant tissue surfaces (Figure 2.1).

2.3.2 Nuclear structures: form and function

Within the nucleus there are many specific structural components that help to regulate gene expression. DNA nucleotides that code for genes make up the majority of material in the nucleus. Nuclear function is further regulated by transcription factors[22], nuclear pores[23], and the nucleolus[24], about which the referenced reviews provide more in-depth detail. Within the nucleus, distinct regions are more carefully classified as: 1) euchromatin, with less dense chromatin and highly transcriptionally active, 2) heterochromatin, with highly dense chromatin and less transcriptionally active, and additionally 3) the interchromatin space, where nuclear components are located, such as the nucleolus which synthesizes rRNA and assembles ribosomes[24,25]. Like a shell, the nuclear envelope membrane is made up of a network a lamins that provide structural rigidity to the nucleus. Distributed among the nuclear membrane, nuclear pores regulate the transport of molecules in and out of the nucleus (e.g. Ca^{2+} and mRNA) (Figure 2.1). The integration of the nuclear components and global structures provide the biophysical conditions for the nucleus to maintain the integrity of the DNA and regulate cellular biosynthesis by modulating the shape, size, and internal patterns of deformation (e.g. displacements and strain).

Local mechanical deformations within the nucleus are thought to alter early transcriptional activities for gene expression. One proposed mechanism is that intranuclear mechanical deformation alters the structure of the chromatin domains thereby modulating the gene expression in the cell[26]. In this mechanism the tightly bound DNA around the histones are mechanically strained to allow or deny access for transcription factors to transcribe DNA into RNA.

2.4 MEASURING NUCLEAR MECHANICS AND MECHANOBIOLOGY

2.4.1 Nuclear imaging, deformation, and measurement techniques

Imaging of intranuclear mechanics in single cells is challenging. Several contemporary methods attempt to meet this need by performing high resolution imaging (e.g. super-resolution microscopy, scanning electron microscopy), although visualization of cell and subcellular structures does not provide information describing how these structures may

deform under applied loading or during active cytoskeletal or chromatin remodeling. Typically, imaging at the micron scale involves chemical fixation of the cell, preventing a real-time biochemical analysis of deformation and associated mechanotransduction activity. Widefield and confocal microscopy are broadly used techniques to measure nuclei in living cells before and after applied deformations to determine the local strains fields under varying experimental conditions [27]. There are a wide variety of methods used to mechanically deform the nuclei of isolated or tissue/matrix-embedded cells (Table 2.1). Typically, cells in 3D microenvironments are deformed and the nuclei are simultaneously imaged by an microscope-mounted deformation device[28] (Figure 2.2)**.** Isolated cells in 2D culture are often placed either in a flow chamber or on a stretchable membrane, where forces are applied on the cell and transferred to the nucleus. A commonality among the deformation and measurement techniques is that the nuclei are fluorescently imaged pre- and post-deformation, so that motion in a current configuration can be measured from a reference configuration.

Considering the variety of available methods available to measure nuclear mechanics (Table 2.1), there are three distinct ways to measure pre- and post-deformation of the nucleus (Figures 2.2 and 2.3), each with distinct strengths and weaknesses. First, changes in bulk morphology of the nucleus (e.g. aspect ratios, nuclear volume, or major/minor axes) enable a quick average mechanical response of the nuclei after mechanically perturbation, often using automated or semi-automated algorithms for the analysis of large numbers of cells in images. While bulk measurements are commonly used in research fields, e.g. tissue engineering, important spatial information from within the nucleus is not captured or described. Second, texture correlation measures intranuclear strain fields by tracking intrinsic high contrast areas, revealed by spatial distributions of fluorescent markers, in the images depicting undeformed and deformed nuclei [27]. Unfortunately, the small nuclear area, coupled with large subset sizes required to help minimize error [27], limits the ability to reliably quantify intranuclear strain. Third, deformable image registration (e.g. hyperelastic warping) permits intranuclear strain measurements by iteratively deforming a three-dimensional (3D) finite element mesh representing the undeformed nucleus until it matches the deformed nucleus [29]. A 3D

intranuclear strain field is calculated from the displaced nodes of the registered nuclear mesh. Bulk morphology of the nucleus, texture correlation, and hyperelastic warping increasingly predict known nuclear deformations applied in simulations (Figure 2.3).

Compared to the known deformation applied, texture correlation underestimates the magnitude of the strain field, and the (bulk) engineering strain measured by changes in width fails to captures the strain distribution or magnitudes. In contrast, hyperelastic warping best approximated the known magnitude and spatial distribution of the applied known strain field, with decreased error (i.e. higher precision and minimal bias) [29].

2.4.2 Measuring mechanobiology

There are several configurations in the literature describing how cell populations are mechanically loaded, including *in vivo* animal studies of the upper or lower appendage, *in vitro* loading of isolated cells on stretchable substrates, or *in situ* deformation of cells maintained in tissue explants[30-33]. Mechanobiology experiments primarily consist of mechanically loading a tissue or cell population, followed by measurement of cellular biosynthesis assays representing average measures of the population response. The mechanical loading duration is often experimentally varied from either a few minutes to several hours repeated for one or several days, and populations of cells are typically harvested and processed for comparisons of mechanically loaded tissue versus unloaded control tissues [30-32]. Powerful biosynthesis assays are often used at the RNA or protein level, such as quantitative real time polymerase chain reaction or enzyme-linked immunosorbant assays, respectively. Technologies developed for study at the single cell level minimize the variability observed in cell populations, which may better explain how changes in nuclear mechanics alters gene expression.

2.4.3 Design criteria to combine nuclear mechanics and mechanobiology

Limitations in the spatial and temporal resolution of image data, and the impact of these limitations on image quality (e.g. signal-to-noise ratio SNR), must be considered when designing techniques to study nuclear mechanics and mechanobiology in single cells. Trade-offs in spatial and temporal resolutions may be accepted for specific applications, noting that the error of intranuclear deformation depends largely the ability to track the

motion of structures on the organelle interior with sufficient SNR. For example, to capture nuclear mechanics and mechanobiology in a single cell, the measurement technique needs to be fast enough to capture a possible rapid gene expression response to the applied load. The technique also needs to have a high enough spatial resolution to image the nuclear shape changes due to the applied load. Spatial resolution is often sacrificed to improve temporal resolution, and vice versa, when designing techniques for the study of single cells [33].

2.5 HYBRID TECHNIQUE - MICROSCOPY AND HYPERELASTIC WARPING

A hybrid confocal and hyperelastic warping methodology was recently demonstrated to measure and calculate intranuclear mechanics and biophysical activities [29]. Combining the high spatial resolution of optical (e.g. confocal or multiphoton) microscopy with hyperelastic warping to measure intranuclear strain maps has provided a methodology that provides detailed intranuclear strains compared to bulk measurement of nuclear deformation (Table 2.1). Optical microscopy also enables imaging deep within tissues to calculate nuclear mechanics of cells maintained in native tissue cultures. Z-stack images capture the full volume of the nucleus in the undeformed and deformed state. The volume of the nucleus is converted into a finite element mesh that is used in an iterative hyperelastic warping-based method, where the undeformed nuclear mesh is digitally systematically warped until it matches the deformed nucleus, to measure 3D intranuclear deformations (Figure 2.4). Hyperelastic warping has been extensively applied also in tissue scale biological applications [29]. The intranuclear strain map can be spatially and temporally compared to any fluorescent indicator of gene expression that can be imaged concurrently with the nuclei stain in a second imaging channel, such as nascent RNA synthesis (Figure 2.4).

2.5.1 Strain transfer: tissue to nucleus

Strain transfer to the nucleus from an applied mechanical load at a distant tissue surface can be measured as amplification and attenuation in local subnuclear regions by microscopy and hyperelastic warping. When cartilage explants undergo shear loading, there is higher tissue strain in the superficial zone that diminishes in the deep zone[34]

(Figure 2.5). Nuclei in compressed cartilage explants are compressed more near the articulating surface (superficial zone) and progressively less in the middle and deep zones[35]. These bulk nuclear volumetric strain results show that there is a depth dependent strain transfer from the applied tissues strain to the nucleus. However, more detailed intranuclear strains are resolved by using hyperelastic warping that shows amplification and attenuation of strain, that the bulk measurement techniques do not reveal (Figures 2.5). The combined use of optical microscopy and hyperelastic warping provides researchers with a new method that gives 3D local nuclear deformations that were previously immeasurable by bulk measurement techniques.

2.5.2 Measuring single cell 3D intranuclear time dependent strain fields

Single cell intranuclear strain fields show complex strains patterns with time-varying magnitudes being spatially correlated to DNA intensity. Confocal z-stack images of chondrocyte nuclei taken before and at 10 and 60 minutes after a shear load is applied to the articular surface of a cartilage explant show similar strain field patterns within a cell, although the magnitudes of the patterns at the two time points differ from cell to cell (Figure 2.6). The intranuclear strain field patterns are spatially complex, with brighter DNA intensity regions in specific cell populations studied typically corresponding to tensile strain regions (Figure 2.4-2.6). A current challenge is to determine strain transfer mechanisms, including specific cytoskeletal elements for load transmission *in situ*. Also, is it not yet known the role of directionally concentrated strains in the physical regulation of gene expression. However, this hybrid methodology does provide high spatial resolution strain maps of the intranuclear space that will allow for future investigation of these questions.

2.5.3 Detecting nascent RNA synthesis in single cells

Combining measurements of intranuclear mechanics with biosynthesis assays, e.g. detection of nascent RNAs, facilitates analysis of mechano-regulated gene expression within the nuclei of single cells. Nascent RNA detection has been measured in cells embedded in their native extracellular matrix [29] using a commercially available global RNA detection kit (Click-iT® RNA Alexa Fluor® 488 Imaging Kit, Invitrogen, Carlsbad,

CA)[36,37]. The incubation for nascent RNA detection began immediately after the deformation and lasted for 60 minutes, and the sample was subsequently fixed for fluorescent labeling (Figure 2.4). In the cell population studied, the RNA was located in the lower intensity DNA regions, i.e. the interchromatin space, where the DNA is less densely packed and thought to be highly active for transcription[25,38] (Figure 2.7). The spatial location of RNA was typically correlated with the more compressive nuclear regions. However, the spatial correlation of mechanics and biosynthesis should be interpreted with cautioned because it was observed that RNA was also transported outside of the nucleus during the incubation period. In a control study, with no tissue scale deformation applied there were fewer nuclei (26%) with detectable RNA synthesis compared to the deformed nuclei results (59%). The mechanism for why the nuclei in the mechanically strained tissue had more detectable RNA nuclei has not been explained, but it is nevertheless important to employ methods that allow for direct spatial correlation of intranuclear strain fields and RNA synthesis in nuclei to help elucidate pathways for gene expression in single cells.

2.5.4 Specificity and experimental tradeoffs

There is still a need to increase the specificity of hybrid microscopy and hyperelastic warping methods to reveal biophysical and biosynthesis actions at even smaller spatial and temporal scales. Labeling of genes related to disease pathogenesis or tissue regeneration may allow for the discovery of local mechanical factors that can alter clinically-relevant gene transcription. One challenge is the development of high (e.g. super) resolution imaging to better reveal spatial patterns, while also not sacrificing temporal resolution of the desired response. For example, an experimental protocol that captures time consuming high resolution images of cell nuclei and fast calcium signaling is affected by competing spatiotemporal factors. The calcium fluxes can occur on the order of seconds to milliseconds, a time duration that is faster than the time required for image acquisition depicting nuclei at high resolution. In contrast, biosynthesis processes like RNA transcription can occur over longer time durations, and may be more appropriately combined with higher resolution imaging to simultaneously provide intranuclear strains fields (Figure 2.3 and Table 2.1). However, the localization of

specific gene activity or gene products is not often resolved in living single cells [33], and it is likely that biotechnology advances for gene expression profiling, coupled with hybrid microscopy, will only improve our understanding of mechanotransduction overall.

2.6 CONCLUSION

This chapter has demonstrated that a hybrid method combining optical microscopy and hyperelastic warping provides detailed subnuclear strain patterns, and represents a balanced approach to meet the competing acquisition factors of spatial and temporal resolutions. The measurement of nascent RNA synthesis was a fundamental step to show that intranuclear mechanics and gene expression related events can be measured within the same nucleus maintained in the native 3D microenvironment. As research objectives turn towards targeting specific genes or profiling of mRNA expression in single cells, new approaches will be developed and will be easily included for spatial correlation of strain fields measured by hyperelastic warping.

Table 2.1. Common techniques for the measurement of nuclear mechanics.

Measurement Technique	Description	Spatial Resolution	Bulk or Local Measurement	Isolated or Embedded (2D/3D) Cells	Ref
Fluorescence Anisotropy	Local Compaction	High	Local	Isolated/2D	39-41
Aspect Ratio	Morphological Change	Low	Bulk	Isolated/2D/3D	42,43
Volume Change	Morphological Change	Low	Bulk	Isolated/2D/3D	44,45
Micropipette Aspiration	Material Properties	Medium	Bulk	Isolated	46,47
Nanoindentation	Material Properties	High	Local (Surface)	Isolated	48,49
Texture Correlation	Nuclear Strain	Medium	Local	Isolated/2D/3D	27,50
Hyperelastic Warping	Intranuclear Strain	High	Local	Isolated/2D/3D	29

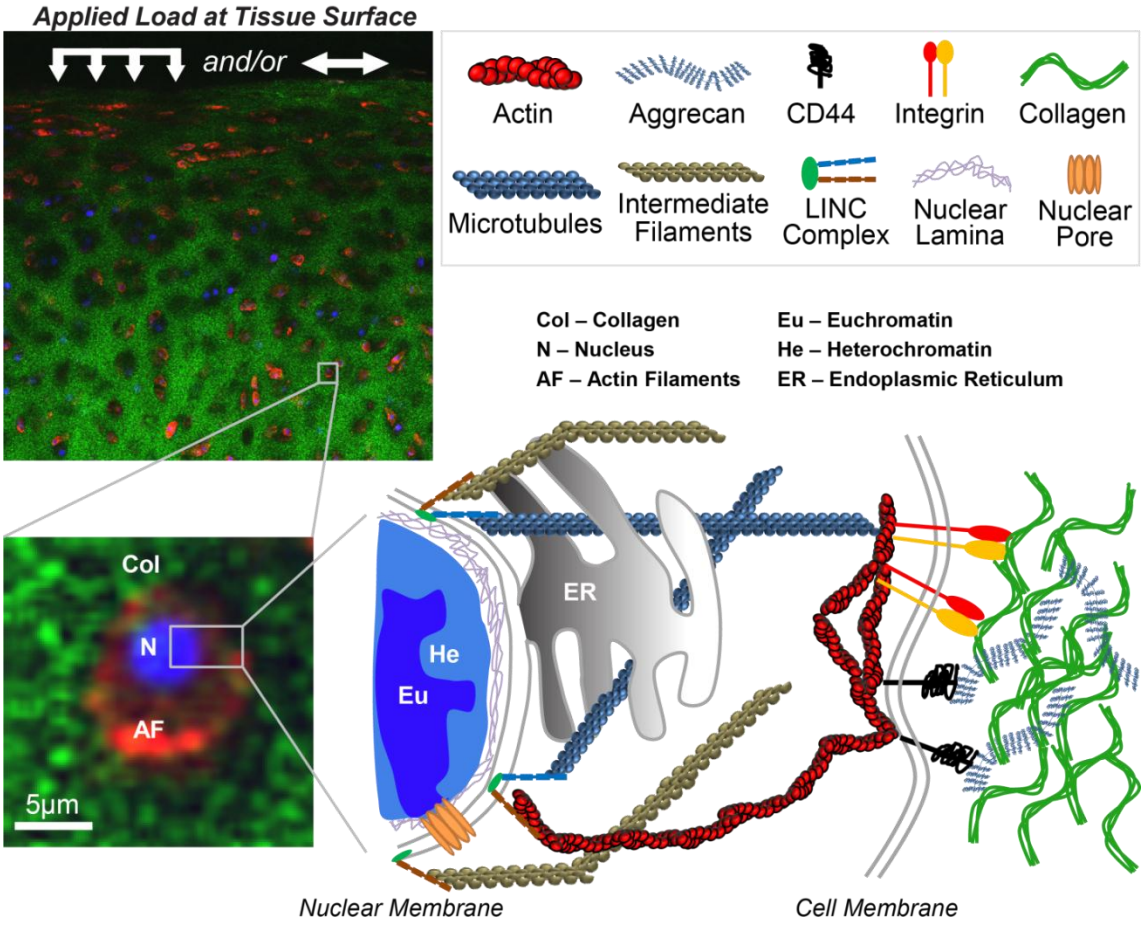

Figure 2.1. Structural components for strain transfer from the tissue and extracellular matrix to the cell nucleus. Strain is transferred from an applied load (e.g. compression or shear) at the tissue surface to the cells and nuclei maintained alive within the interior. Articular cartilage is shown here as a model hierarchical system that normally undergoes many thousands of loading cycles during daily activities like walking. Multiple structural components, including integrins, cytoskeletal proteins, and the nuclear lamina, connect the extracellular matrix to the nucleus.

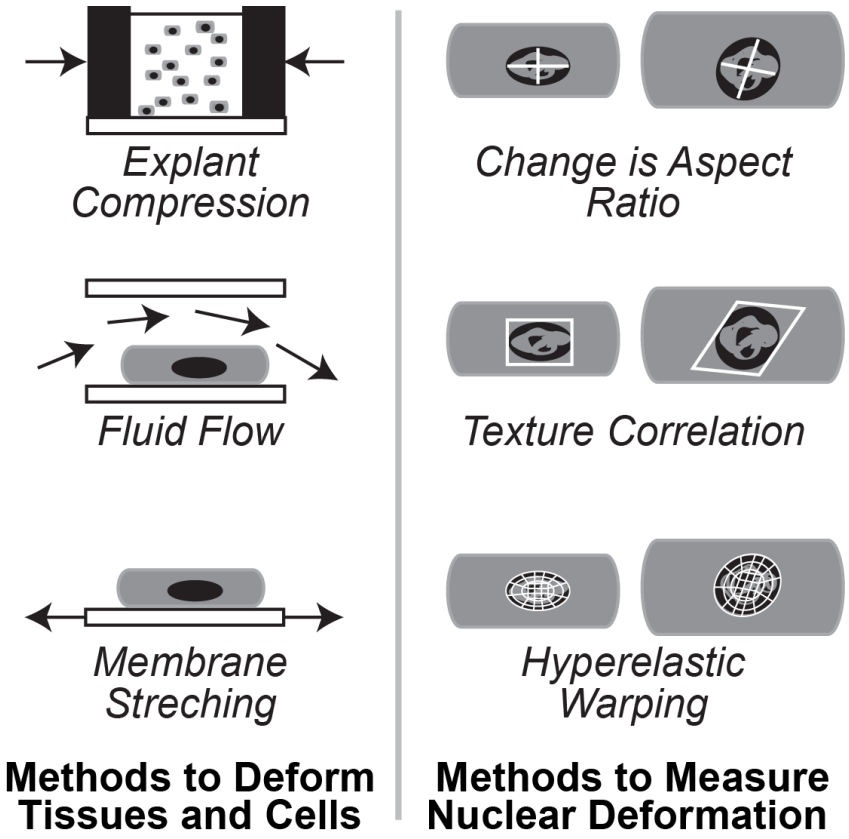

Figure 2.2. Common methods to measure mechanical deformation in the nucleus. Flow and stretch methods deform tissues and isolated cells in 2D (monolayer) or 3D (embedded) native or engineered microenvironments. Simple measures of nuclear shape and morphology changes are documented by changes in aspect ratio. Texture correlation and hyperelastic warping methods provide details of internal strains with different levels of error as described in Figure 2.3.

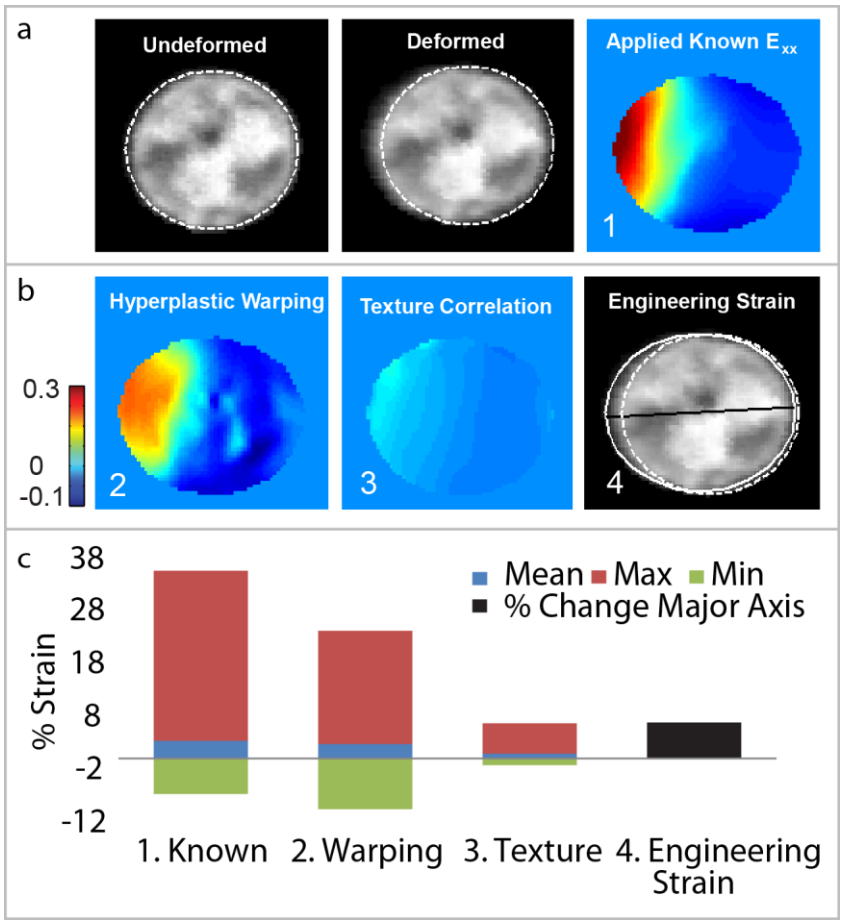

Figure 2.3. Comparison of three techniques to quantify nuclear deformation. A finite element model was used to apply a known deformation (strain) to a nucleus and create the deformed nucleus from the undeformed z-stack images (a). Knowing the applied intranuclear strain (a.1) three contemporary measurement techniques, hyperelastic warping (b.2), texture correlation (b.3) and major axis engineering strain (b.4), where used to measure the strain fields for comparison between the techniques. Results from the hyperelastic warping method best described the known deformation, with decreased sensitivity observed from texture correlation and engineering strain measures.

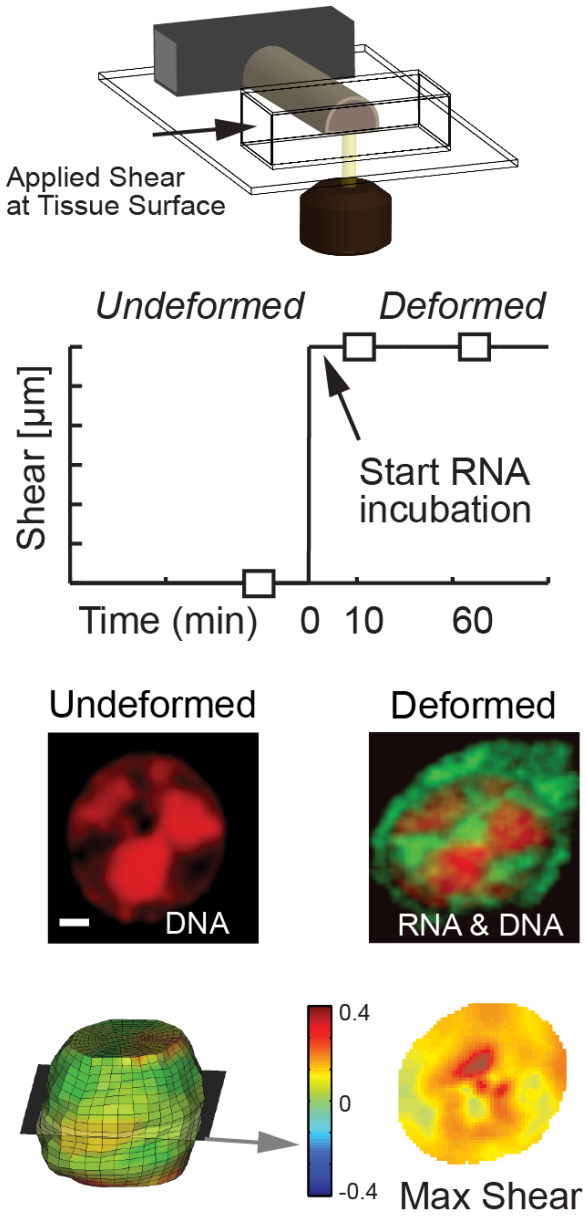

Figure 2.4. Experimental overview for methods to measure single cell intranuclear mechanics and RNA synthesis. For articular cartilage, a tissue explant is created as a half cylinder from a cored osteochondral plug and placed in an electronically controlled deformation device that allows for single cells to by imaged within the deforming tissue using confocal microscopy. Immediately after shearing, newly synthesizing RNAs are labeled using a click chemistry-based incubation. The deformed nucleus is imaged at 10 minutes and then at the end of the incubation time (60 min), and the data are used for the measurement of intranuclear strain using hyperelastic warping. Images of the nucleus are taken from the center z-slice (red=DNA stain, green=RNA stain). (Scale bar = 1 µm)

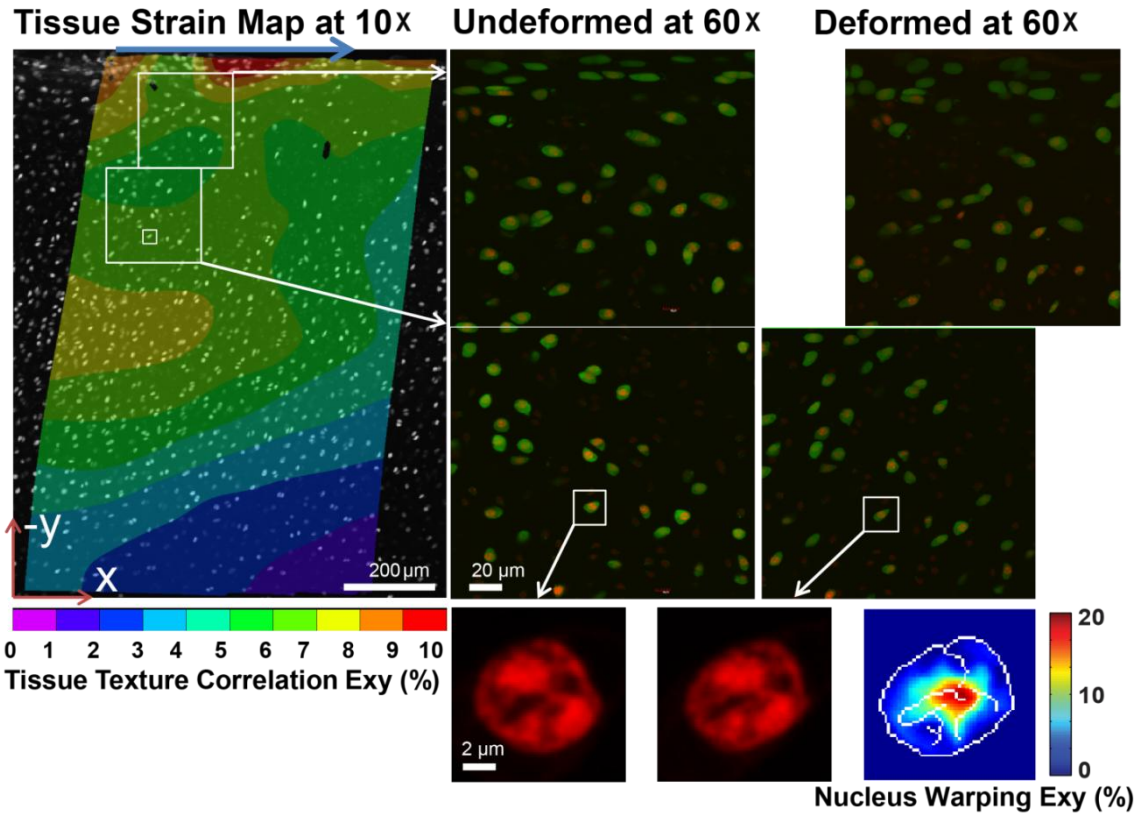

Figure 2.5. Strain Transfer from the tissue surface to the intranuclear regions. A shear load was applied at the articular cartilage surface (blue arrow) and texture correlation was used to measure the E_{xy} strain field for the tissue scale deformation (10×), using cells as fiducial markers. Hyperelastic warping was used to measure the strain fields of the nucleus highlighted by the smaller boxes in the 10× and 60× images. Depending on the intranuclear region, the measured tissue scale strain (5-6%; i.e. Tissue Texture Correlation E_{xy} (%) strain field) was amplified or attenuated when compared to the Nucleus Warping E_{xy} (%) strain field.

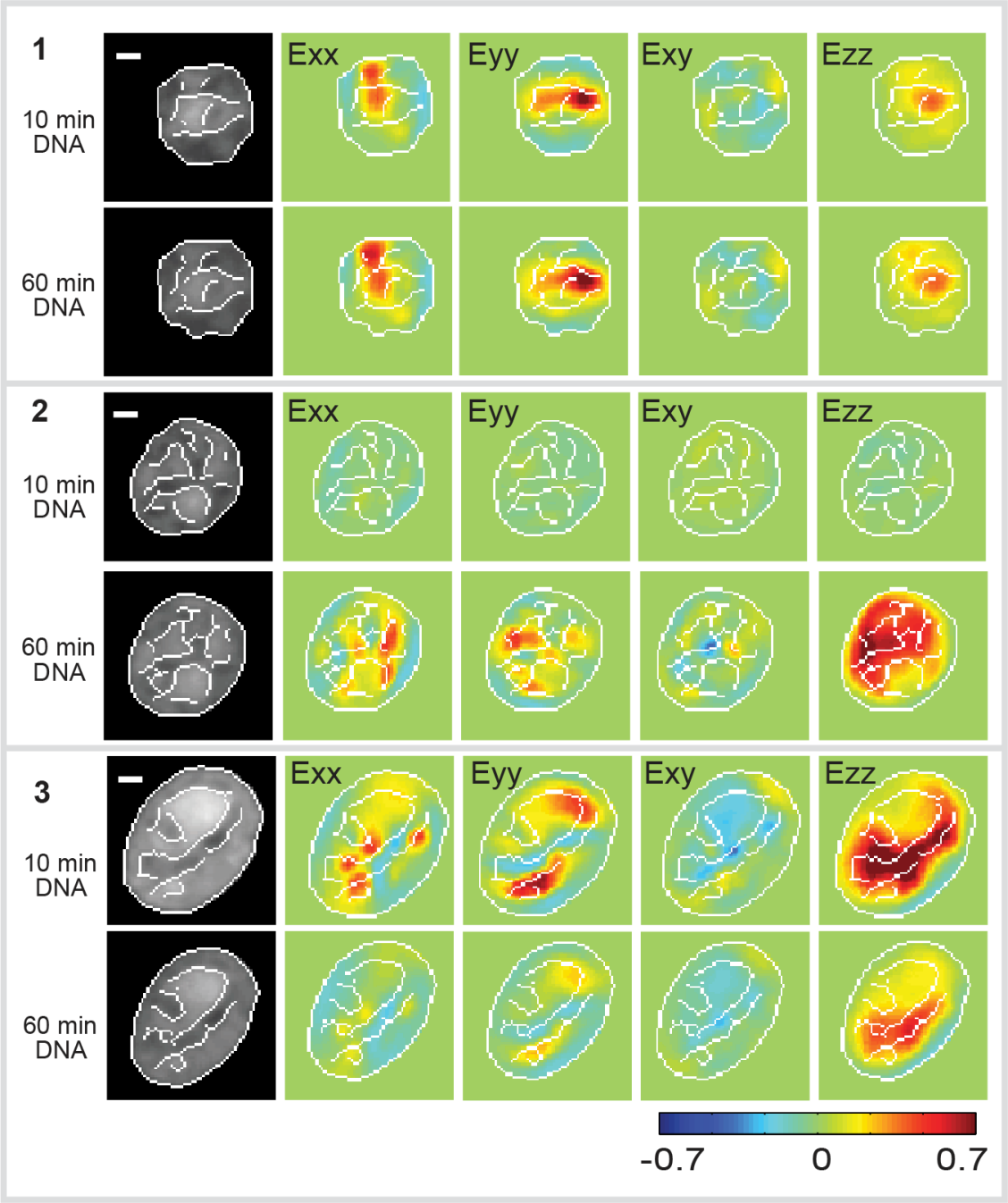

Figure 2.6. Intranuclear strain maps vary with time and among cells**.** Three nuclei were selected from the same imaging region within a cartilage explant for comparison of the strain fields of the deformed nucleus at 10 and 60 minutes after the applied tissue shear strain. White lines are overlaid as visual aids to show the DNA image intensity edges overlaid onto the strain fields. The strain patterns are similar between each time point but the magnitude either, remains constant (1), increases (2), or decreases (3). (Scale bar = 1 μm)

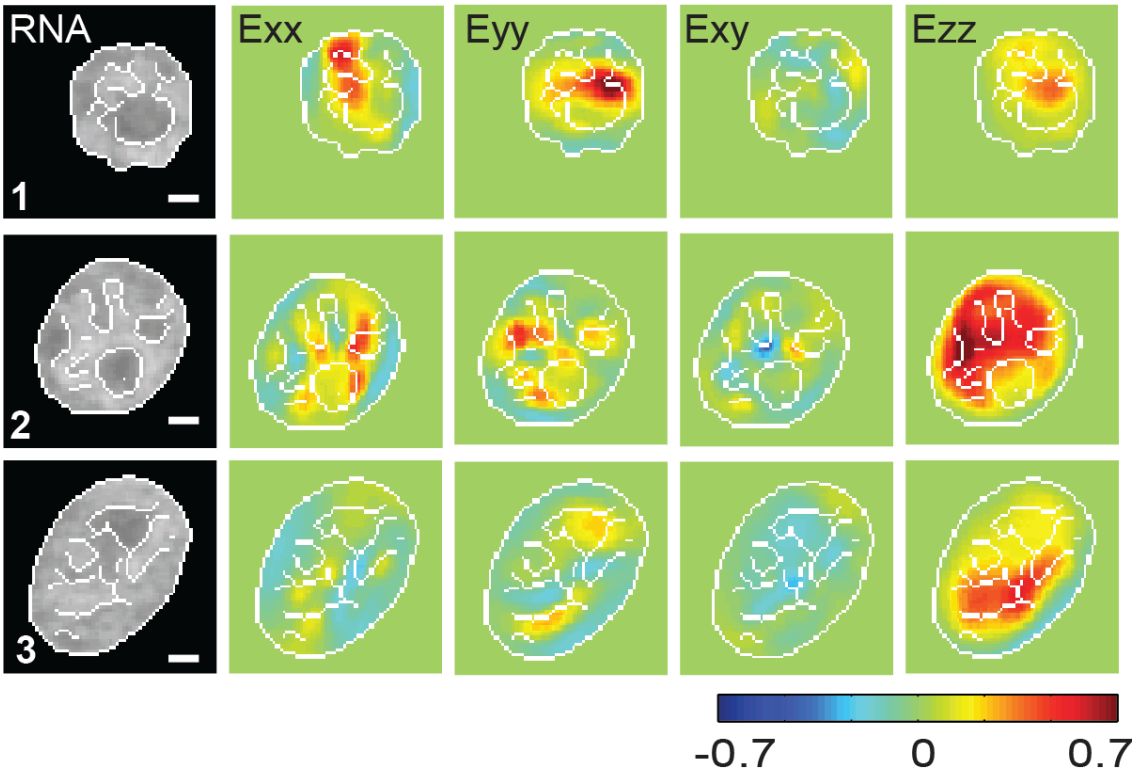

Figure 2.7. RNA images and intranuclear strain maps vary among cells. Nascent RNA was measured in the same nuclei in Figure 6. The same 60 min strain field is overlaid with the RNA edge lines above. (Scale bar = 1 μm).

CHAPTER 3. DIRECT MEASUREMENT OF INTRANUCLEAR STRAIN DISTRIBUTIONS AND RNA SYNTHESIS IN SINGLE CELLS EMBEDDED WITHIN NATIVE TISSUE

This chapter is primarily a reproduction of a published article in Biophysical Journal. A copy of the article is located in the Publications section for reference.

3.1 ABSTRACT

Nuclear structure and mechanics play a critical role in diverse cellular functions, such as organizing direct access of chromatin to transcriptional regulators. Here, we utilized a new hybrid method, based on microscopy and hyperelastic warping, to determine three-dimensional strain distributions inside the nuclei of single living cells embedded within their native extracellular matrix. During physiologically-relevant mechanical loading to tissue samples, strain was transferred to individual nuclei, resulting in submicron distributions of displacements, with compressive and tensile strain patterns approaching a five-fold magnitude increase in some locations compared to tissue-scale stimuli. Moreover, nascent RNA synthesis was observed in the interchromatin regions and spatially corresponded to strain patterns. Our ability to measure large strains in the interchromatin space that reveals that movement of chromatin in the nucleus may not be due to random or biochemical mechanisms alone, but may result from the transfer of mechanical force applied at a distant tissue surface.

3.2 INTRODUCTION

The nucleus is a membrane bound organelle and regulation center for gene expression in the cell [51]. The position of a gene in the interior of the nucleus changes when it becomes highly expressed, and is often found to extend out of its chromosome territory into the interchromatin space [52]. The accessibility of DNA regions by transcription factors may be driven by a variety of mechanisms, including diffusive or thermal conformational

changes [53,54], or through biochemical processes [55], which affects the chromatin structure and the complex local binding affinities of the chromatin and RNA molecules surrounding a gene. Less clear is the role of mechanical force transfer as a directed movement mechanism for DNA accessibility, due perhaps to the technical challenges in measuring small scale mechanics inside the nuclei of cells embedded in their native extracellular environment.

Mechanical forces transfer to the nucleus directly and indirectly through specific cellular pathways and cytoskeletal structures [5,56]. There is increasing evidence that mechanical forces are transferred to the nucleus to orchestrate transcriptional activity [26]. Protein dynamics inside the nucleus are additionally important for maintaining the nuclear structure and in facilitating gene expression at the transcription level [57]. Probing spatiotemporal relationships between distributed mechanical forces and localized gene expression (i.e. biophysical and biochemical interactions) in the nuclei of individual cells is necessary because the individual cells experience different mechanical stimuli resulting from variations in local cell and extracellular matrix interactions. Studies that provide average measures over cells in a given tissue would oversimplify the heterogeneity intrinsic to the population. In order to understand the inherent variability of large cell populations, innovative methods are therefore required for combined measurements of single nuclei biophysical and biochemical interactions in cells maintained in their native three-dimensional (3D) extracellular matrix microenvironment.

Current methods used to simultaneously probe biophysical or biochemical interactions in small subcellular structures like the nucleus are lacking. Methods to characterize nuclear mechanics typically study isolated cells or cells embedded in 3D gel matrices, and often report aspect ratio and volume change measures [28,43,58] that do not easily reveal the inherent complexity of internal strain patterns. Additionally, such methods lack the spatial resolution necessary for the correlation of intranuclear biomechanics and simultaneous internal biochemical activity. Recent approaches to link nuclear mechanics to biochemical responses have explored unique microscopy-based experimental designs, including the use of photobleaching and FRET pairs [59,60].

We simulated physiologically-relevant shear loading to tissues while simultaneously measuring nuclear mechanics and nascent RNA synthesis. Applied dynamic or static tissue shear loading mimics routine activities of cartilage-to-cartilage contact in the body during walking or standing activities. Here, we describe detailed patterns of intranuclear strains and newly synthesized RNA in the nuclei of single cells *in situ* during static tissue-scale loading. The use of a new hybrid imaging technique enabled us to measure biomechanical and biochemical activities in the nuclei of single cells that contribute to our understanding of whether applied tissue mechanical force directly transfers to the nucleus to influence gene expression. Measured subcellular displacements and strains suggest that the nucleus is a complex structure that is actively deformed during mechanical loading at the tissue scale, with large motions and deformations that may regulate DNA accessibility in part by direct physical interactions.

3.3 MATERIALS AND METHODS

3.3.1 Tissue harvesting and sample preparations

Articular cartilage explants with embedded cells (chondrocytes) were chosen as a model system due to their spatially heterogeneous mechanics and ultrastructure [61], with a mechanically-linked and significant disease relevance [62]. This model system was additionally useful to closely mimic physical forces in a common daily activity, i.e. tissue contact during the walking cycle. Briefly, articular cartilage explants were harvested from juvenile bovines within 36 hours of slaughter. Using a cork borer and custom cutting jig, explants (diameter = 5 mm, thickness = 2 mm) were obtained under standard sterile conditions for tissue/organ culture. Explants and embedded chondrocytes were maintained in DMEM/F-12, supplemented with 0.1% bovine serum albumin, 100 units/ml penicillin, 100 µg/ml streptomycin, 50 µg/ml ascorbate-2-phosphate, and 10% FBS (Invitrogen, Carlsbad, CA). After harvesting, the explants were cut along the depth direction to produce hemi cylinder pairs that were incubated and equilibrated for 24 hours before testing.

3.3.2 Mechanical loading and imaging of DNA and newly synthesized RNA

A custom load application device, built for biaxial (compression and shear) loading of tissue samples, was used to apply a 15% simple shear strain at the surface of the cartilage explant while confocal (*z*-slice) images were captured before and at multiple time points during deformation (Figure 3.1). The loading apparatus included two piezoelectric motors with mounted magnetic encoders, and computerized displacement control in small (±61 nm) increments (Nanos Instruments, GmbH; Hamburg, Germany). The device was mounted over a confocal microscope (Olympus Fluoview) to allow for simultaneous loading of the cartilage tissue and imaging of the chondrocyte nuclei in their native extracellular matrix (Figures 3.1 and 3.2).

At the time of testing, a pair of hemi cylinders from the same explant was selected, with one randomly assigned for treatment (mechanical loading) and the other one used as the nonloaded control. The explants were exposed for 8 min to a DNA stain (DRAQ5, Cell Signaling Technology, Inc.). The treated sample was affixed at both ends with cyanoacrylate to the loading apparatus with the cut surface positioned next to the coverslip and near the objective, noting that cell viability was maintained throughout the duration of testing (Figure 3.10). Both samples were placed in respective cell culture dishes and covered with phosphate buffered saline.

For imaging before and following deformation, an area of interest near the articular surface was visualized using a confocal microscope with a 60× water objective (NA=1.20). 3D (*z*-stack) images (matrix=1600×1600 pixel^2; number of slices=19) were sequentially captured with a *z* step of 0.5 μm/slice and a calculated in-plane resolution of 0.132×0.132 μm^2. DNA was visualized by DRAQ5 staining (633 nm) prior to loading (Figure 3.1a). DNA was imaged again 10 and 60 min following shear loading using the same imaging parameters. A Click-iT® RNA Alexa Fluor® 488 Imaging Kit (Invitrogen, Carlsbad, CA) was used to detect RNA synthesis during the 60 min deformation period (described subsequently). Two channels (i.e. DNA at 633 nm and RNA at 488 nm) were acquired in sequential mode to eliminate cross talk. To detect the newly synthesized RNA, a filter bandwidth (520-600 nm) was additionally selected to exclude background from

the autofluorescence of collagen in the extracellular matrix (Figure 3.3). Although the peak of the collagen autofluorescence was around 488 nm, there was still a very weak signal that was detected from the tail of the collagen emissions spectrum at 520 nm, and which was easily removed in image post processing. The untreated control sample underwent the same protocol, except that shear loading was not performed. An additional no tissue deformation time dependent control was implemented to determine what the intranuclear strain maps would be in a mechanically non-perturbed state (supplemental information 3).

3.3.3 Calculating nucleus 3D strain maps by hyperelastic warping

Hyperelastic warping was used to find the displacement field of the deformed nucleus. To measure internal nuclear deformation, a 3D finite element mesh was created from the confocal images depicting DNA, and a hyperelastic warping algorithm (nike3d) was used to calculate displacement and strain patterns throughout the nuclear volume (Figures 3.1 and 3.4) [63,64]. The algorithm deformed a 3D mesh of the *z*-stack image of the nucleus in the reference configuration until it matched the target image of the nucleus in a deformed configuration based upon minimization of the differences in image intensities between the reference image and the deformed image [7,65]. Nodal displacements were used to compute finite Lagrangian 3D strain fields, and principal strains and directions.

3.3.4 Measurement of error in displacement fields using simulations

To validate our hybrid method, in particular the use of hyperelastic warping to quantify strain fields in the interior of small nuclear structures, and to determine the error associated with the hybrid technique overall, we used extensive forward finite element simulations. A 3D mesh was created from the *z*-stack images of a nucleus that was deformed in a finite element simulation with known displacement and strain magnitudes representative of those observed in the nuclei of living cells. A deformed image data set was created based upon the displacements of the forward finite element model. These images were analyzed using hyperelastic warping, and additionally, data was also directly compared to well-known texture correlation techniques. Forward finite element stimulations were used to create a known displacement field and determine error

(quantified in terms of RMSE, bias, and precision) of the hyperelastic warping and texture correlation techniques. The forward simulation generated a known 3D displacement field and images of the deformed nucleus that was representative of experimental data. Gaussian noise was added to the image sets to vary the signal-to-noise (SNR) and contrast-to-noise (CNR) ratios to span the range of experimentally observed values. In-plane (x and y displacement) comparisons between the techniques were made in image slices through the center and at the edge of the image volume. Differences between calculated and known displacements were used to estimate the average RMSE, bias, and precision, over the range of simulated SNR and CNR ratios.

3.3.5 Nascent RNA Synthesis In Situ

A Click-iT® RNA Alexa Fluor® 488 Imaging Kit (Invitrogen) was used to tag and image newly synthesized RNA over a 60 minute period of deformation (Figure 3.1b). Nascent RNA detection was performed by a click chemistry reaction between an RNA incorporated 5-ethynyl uridine (EU) tag and an azide-containing dye after cell fixation and permeabilization [36,37]. Briefly, after incubation during loading, the samples were fixed with 2% formaldehyde in PBS, permeabilized with 0.1% Triton® X-100 in PBS, and exposed to freshly prepared Click-iT® reaction cocktail, while still in the loading apparatus.

To image nascent RNA synthesis *in situ*, two preliminary studies were additionally performed to successfully translate the RNA detection technology from its developed use in monolayer cells [36,37] into a 3D tissue environment. First, we minimized the background autofluorescence of collagen and the non-specific binding of the fluorescent tag. We selected an appropriate emissions range on the confocal detector to minimize signal from collagen, and in addition we applied an image enhancing blocking reagent (Image-iT FX Signal Enhancer, Invitrogen, Carlsbad, CA) to help minimize non-specific binding (Figure 3.3). To remove nonspecific background staining in our studies, a 60 min incubation of the blocking reagent was used prior to the final image acquisition. Second, we determined the duration of EU incubation to enhance RNA signal detection following mechanical shear loading. It should be noted that excessive incubation times resulted in

an observed RNA signal from the combined effects of shear deformation and routine (e.g. housekeeping) cellular RNA synthesis [36]. Using time duration studies, we determined that routine RNA synthesis was detected above background fluorescence levels in the cells of tissues that were unloaded and incubated for 60 min, indicating a time duration that could be used to best detect RNA signal enhancement due to mechanical loading. To further control for sample variation in routine RNA synthesis, one half of the tissue explant (i.e. one half of the hemicylinder) was loaded while the second half was used as the unloaded control (Figure 3.3).

3.3.6 Relationship between intranuclear strains and newly synthesized RNA

To explore links between the internal nuclear mechanics and newly synthesized RNA, the intranuclear strain fields were spatially compared qualitatively and using quantitative correlation analyses with custom MATLAB code. The raw data consisted of strain values that were correlated to the image (DNA or RNA) intensity values at each voxel location of the nucleus. To facilitate correlations between strain and RNA or DNA image intensities, the data was binned according to the image intensity (bin size=0.02). The data was binned for each image slice, and the binned results were additionally averaged for a single slice and averaged *z*-stacks**.** Correlation statistics (e.g. r^2 values) were calculated from the binned data sets.

3.4 RESULTS

3.4.1 Hybrid Microscopy Reveals Complex Intranuclear Displacements and Strains

Intranuclear deformation, defined by displacements and strains, were found to be heterogeneous and complex in living cells embedded within their native extracellular matrix. Intranuclear strains were both amplified and attenuated compared to tissue-scale stimuli. During a 15% simple shear strain, intranuclear displacements overall were consistently sub-micron in magnitude, with differences approaching only 10s of nanometers depending on the size and location of the regions used for comparison (Figure 3.5). Strong displacement gradients resulted in large intranuclear strains, typically less than 75% in magnitude, depending on location in the nucleus (Figure 4, 7).

Microscopy and hyperelastic warping quantified heterogeneous and complex intranuclear strain with minimal error. Importantly, the *x* and *y* displacement fields for the middle slice of the nucleus showed that hyperelastic warping matched more closely to the known (simulated) displacements compared to conventional (1st order) texture correlation algorithms (Figure 3.5). The known displacements were plotted versus the displacements measured by hyperelastic warping (slope = 1.11, $r^2 = 0.958$) and texture correlation (slope = 0.97, $r^2 = 0.477$). Hyperelastic warping and texture correlation were also compared using experimental data of a nucleus in undeformed and deformed states (Figure 3.5b). A comparison of warping and texture correlation displacement predictions with those of the forward model indicated similar qualitative displacement distributions. However, the texture correlation results were lower in magnitude than the hyperelastic warping results. We further noted that texture correlation displacement fields were biased by the bright areas in the image and around the nucleus perimeter, which was qualitatively observed in the known and experimental displacement fields (Figure 3.5). Hyperelastic warping consistently resulted in displacement data with lower error (avg. RMSE = 0.017) compared to texture correlation (avg. RMSE = 0.091), and without sensitive dependences on signal-to-noise and contrast-to-noise ratios (Figure 3.6).

3.4.2 Interchromatin Regions and Nascent RNA Synthesis

Nascent RNA synthesis was observed in the interchromatin regions within nuclei of single cells embedded in their native extracellular matrix during shear loading at the tissue scale. For the nucleus depicted in Figures 3.7 and 3.8, changes in chromatin position, defined in terms of strain, were also found to correspond to regions of nascent RNA synthesis. Magnitudes of principal strains and maximum shear strains approached a five-fold tensile increase over the 15% simple shear strain magnitude applied at the tissue surface in some regions of the nucleus. Different regions within the nucleus exhibited compressive or tensile strains, indicating that the magnitude of the applied shear at the tissue surface was amplified and attenuated depending on the internal region of the nucleus under investigation (Figure 3.7). Principal directions for E_{p2} and E_{p3} were predominately in the imaging plane (i.e. in the *xy* plane), while E_{p1} directions were largely through-plane. Qualitative comparisons of the strain patterns revealed a

correspondence between high tensile strain regions with increased intensities of the RNA and DNA patterns for max shear (RNA) and E_{p3} (DNA), respectively. Strain patterns tended to correspond visually to observed DNA and RNA patterns, suggesting that specific stimuli, e.g. localized maximum strain, may cause changes in the chromatin structure to influence newly synthesized RNA in nuclear regions with low DNA content.

Relationships between DNA, RNA, and strain could be quantified at multiple levels, i.e. within a given image slice through a single nucleus (e.g. Figure 3.7), within an image volume representing a whole single nucleus (e.g. Figure 3.8), or among nuclei from many single cells (e.g. Figure 3.9). For the single image slice in Figure 7, significant correlations (p<0.007) were found between DNA intensities and E_{p1} (r^2=0.238), E_{p2} (r^2=0.506), and E_{p3} (r^2=0.833), but not max shear (r^2=0.000; p=0.984). Significant correlations (p<0.001) were also found between RNA intensities and E_{p1} (r^2=0.617), E_{p3} (r^2=0.754), and max shear (r^2=0.827), but not E_{p2} (r^2=0.214; p=0.096). Similar correlations were observed for a whole single nucleus (Figure 8), after pooling r^2 values from each slice of the image volume, with DNA and RNA related to E_{p1} (r^2=0.543, r^2=0.668), E_{p2} (r^2=0.677, r^2=0.471), E_{p3} (r^2=0.889, r^2=0.473), and max shear (r^2=0.192, r^2=0.694), respectively.

Relationships between strains and DNA and RNA intensities varied among the cell nuclei studied (Figure 9). Nascent RNA synthesis was consistently observed in the interchromatin regions, although specific intranuclear statistical correlations covered a broader range when compared cell-to-cell. Significant statistical correlations (p<0.015) were found in all cells studied between DNA intensities and E_{p1} (r^2=0.575) and E_{p2} (r^2=0.735), and between RNA intensities and E_{p3} (r^2=0.641), with aforementioned coefficients of determination pooled over all nuclei shown in Figure 9. Statistical correlations varied among cells between DNA intensities and E_{p3} (r^2=0.550, p<0.443) and max shear (r^2=0.575, p<0.306), and between RNA intensities and E_{p1} (r^2=0.357, p<0.379), E_{p2} (r^2=0.492, p<0.295), and max shear (r^2=0.374, p<0.954), with 6 of 20 total possible correlations (i.e. 5 relationships for the 4 cells shown in Figure 9) not significant (p>0.040).

3.5 DISCUSSION

Diffusive or biochemical processes are thought to drive the movement of genes to different regions of the nucleus, perhaps due to changes in binding affinities in addition to conformational alterations in the chromatin structure. Additional studies, involving the use of relatively insensitive methods based on texture correlation, indicate that the deformation in the nucleus is minimal compared to cell and extracellular matrix strains [66]. These studies imply that the relative stiffness of the nucleus is high compared to surrounding cellular structures, resulting in minimal internal deformation for a given applied load. The concept of a relatively stiff nucleus would indirectly support the idea that specific (e.g. diffusive) mechanisms alone may drive gene expression, since the nucleus interior would be more isolated from physical deformation occurring in the extranuclear regions, and would require alternative mechanisms for transcription and other regulators to access DNA.

Here, we find that movement of the nuclear structures, quantified by strain, is highly heterogeneous and is both amplified and attenuated during even simple mechanical loading at the tissue scale. Given a reasonable compliance of chromatin, the heterogeneous strains would be expected to shift and reposition the relative internal position of genes, thereby altering the dynamics of regulation. Interestingly, the compliance of individual chromatin fibers has also been noted as a possible physical basis for DNA accessibility [67]. However, we do not yet know the extent that either chromatin remodeling, or passive chromatin deformation in response to the applied load, explains the intranuclear strain patterns described. In light of this current limitation, and in contrast to single molecule studies conducted in controlled *in vitro* experiments, we overcame technical challenges in obtaining measurements within the nuclei of cells embedded in extracellular matrix *in situ*. The experimental set up and hybrid microscopy technique allowed us to propagate realistic and physiologically-relevant mechanical forces through native structures to better quantify the extent that strain transfer may directly influence nuclear mechanics. The hybrid method, based on microscopy and hyperelastic warping, allowed the measurement of internal deformation (displacements and strains) in small nuclear structures at high spatial resolutions, limited most by the

time constraints of image acquisition. Interestingly, the simultaneous detection of newly synthesized RNAs reveal localized expression corresponding to mechanical loading and patterns of principal and shear strains. The measurement of large (e.g. shear) strains in the interchromatin space that spatially correspond to the localization of nascent RNA expression supports the hypothesis that localized movement of chromatin in the nucleus may not be due to random or biochemical mechanisms alone, but instead can occur simply as a result of mechanical force transfer applied at a distant tissue surface. However, significant transport of RNA over the incubation time (e.g. Figure 1) indicates that the nascent RNAs observed may not be a true response of the nucleus to deformation. Additionally, RNA expression was observed in nucleus regions that were expected to be more naturally transcriptionally active. Nevertheless, these regions corresponded with unexpectedly high levels of strain, suggesting that the nucleus structure may be routinely regulated through a variety of casual physical activities that involve tissue loading, which in turn allow for transcriptional and other regulators of biological activity and gene expression.

Our experimental analysis demonstrated the hierarchical transfer of strain over large distances and log scales from the tissue surface to the interior of individual nuclei *in situ*. In our study, simple shear strain applied at a distant tissue surface transfer to individual nuclei, amplifying strain up to five-fold in localized nuclear regions. Interestingly, we note reports of novel quantitative approaches to measure detailed internal biomechanics in individual cells, but these techniques largely ignore the intranuclear strain and gene expression [58]. Quantification of intranuclear strains is important, because they possibly extend the concept of nuclear mechanics arising due to physical links to the cytoskeleton or extracellular matrix [5,56], to also include remote links through pericellular and extracellular molecules, e.g. type VI and type II collagens, respectively, in the hierarchical organization of complex tissues like cartilage. Using the hybrid method, we did not yet in the current configuration tease apart the relative influence of load transfer through solid or fluid phases [68], or specify candidate matrix or cytoskeletal molecules that result in strain transfer. However, candidate molecules may be identified and visualized by fluorescent tagging in subsequent studies. In the present work, it is important to

emphasize the nondestructive nature of the hybrid technique, coupled with the ability to reveal internal spatiotemporal dynamics in living cell nuclei *in situ* for the first time, which enables the study of diverse cell-laden materials, including hydrogel or polymer constructs, and diseased tissues, that contain unique or rare cell populations.

The nucleus-to-nucleus variation of intranuclear strain field patterns (Figures 3.4, 3.8-3.9) suggested that the applied tissue load was not uniformly transferred to every nucleus, possibly due to the spatially heterogeneous mechanics of cartilage explants that arise from cell location and spatial density in the tissue [69]. This observation indicates the possibility of subtle and variable underlying cell-matrix connections or other structural parameters that dictate how load is shared over hierarchical scales. Interestingly, newly synthesized RNA was also observed outside of the nuclear region of the cell, illustrating transport during the short incubation time, which has also been reported in other cell types following treatments with soluble factors [36,37]. Further, intranuclear strain patterns depended on time for some of the nuclei studied (Figure 3.11), suggesting more complicated (e.g. viscoelastic) mechanisms may play a role in RNA expression in some cells. Strain maps measured from DNA images taken at 10 min and 60 min post-deformation indicated an increase, decrease or no change in the intranuclear strain fields and magnitudes between the two time points. While very small differences in aspect ratios of the 10 and 60 minute deformed nuclei indicate no bulk deformation of the nucleus between the two time points (Figure 3.11).

These data suggest that cells *in situ* can sense an applied load that is transferred over relatively large distances and log scales to alter intranuclear deformation and to possibly directly influence new RNA synthesis, and may regulate other actions as well, including the transport of mRNA or other molecules through nuclear pores. The direct correspondence of strain and DNA or RNA patterns may suggest specific mechanical stimuli, e.g. shear strain, that influence spatially-localized gene expression in individual cells, although it remains to be determined the extent that mechanics directly regulate nuclear mechanobiology in large cell populations. We expect that this hybrid method, based on microscopy and hyperelastic warping, will enable a wide variety of future

investigations into mechanotransduction mechanisms, including transcription of specific RNAs, and translation and control of downstream protein synthesis.

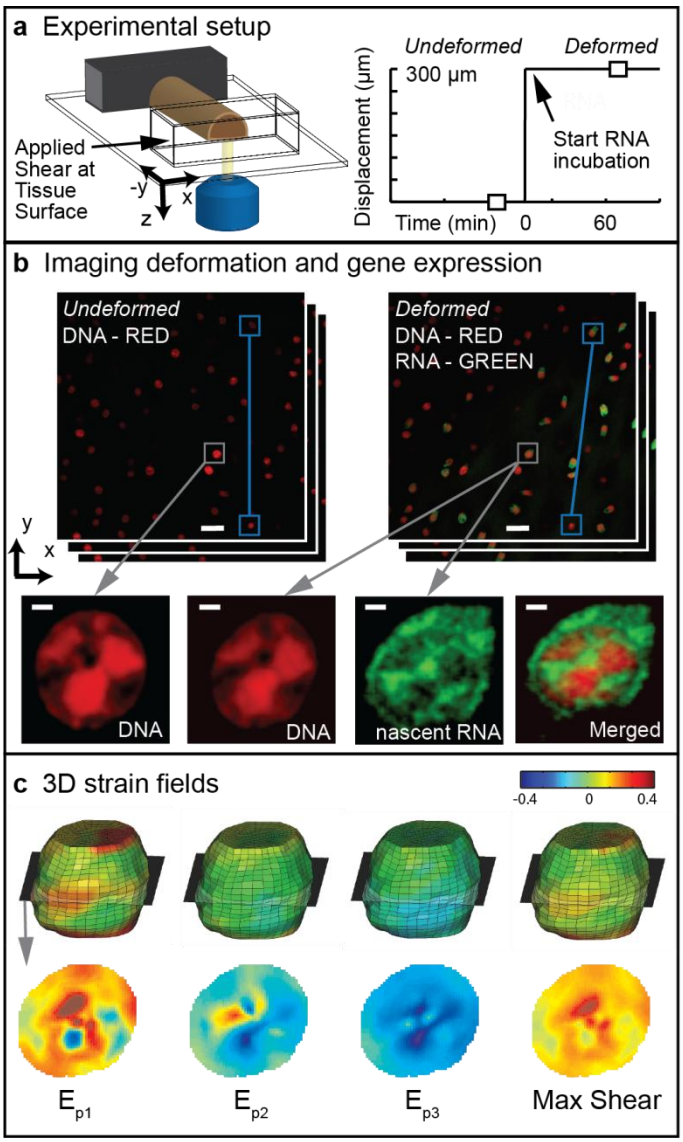

Figure 3.1. Combined confocal microscopy and hyperelastic warping reveals 3D strain fields and nascent RNA expression in the nuclei of single cells. **(a)** A custom tissue deformation device and microscope objective was used to image a cartilage explant during shear loading. **(b)** Projection images were constructed from undeformed and deformed confocal *z*-stack images (Red=DNA, Green=nascent RNA at 60 min, scale bar = 20 µm). Connected blue boxes track two nuclei to show tissue-scale shear deformation. Grey boxes point to a magnified middle slice of the nucleus volume (scale bar = 1 µm. **(c)** The selected nucleus from **(b)** is shown as a warped 3D volume with color maps representing principal strain fields and max shear, with the middle slice cross section detailed below. Importantly, the nuclei aspect ratios (undeformed = 1.08 and deformed = 1.15) do not capture the complexity of the intranuclear deformations.

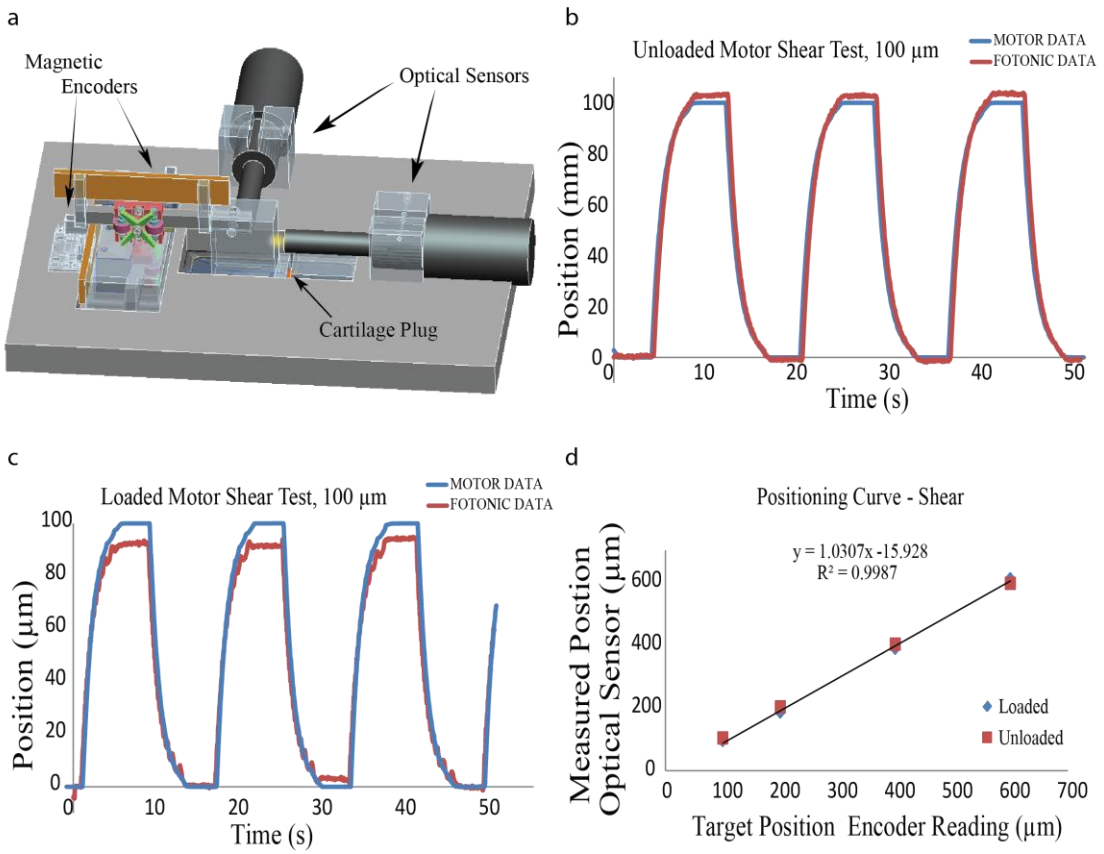

Figure 3.2. The tissue deformation system was validated using a fiber optic displacement measurement system. Motion was provided by two magnetic linear encoders (Nanos Instruments, GmbH; Hamburg, Germany) mounted on Piezo LEGS LL1011A motors (Micromo; Clearwater, FL), and verified using a MTI-2000 Fotonic Sensor (MTI Instruments; Albany, NY). **(a)** CAD representation of the loading device with encoders as well as optical sensor in their respective positions. **(b)** Plot of a representative square-wave (100 µm) displacement profile in control experiments (i.e. actuator motion without a sample present). There was a small, micron-scale offset between the encoder positioning and the Fotonic Sensor readout. **(c)** Plot of a square-wave (100 µm) displacement profile with a sample present. **(d)** Three square wave cycles at each position were averaged to produce the linear calibration curve loading a sample (diamonds) and without a sample (squares).

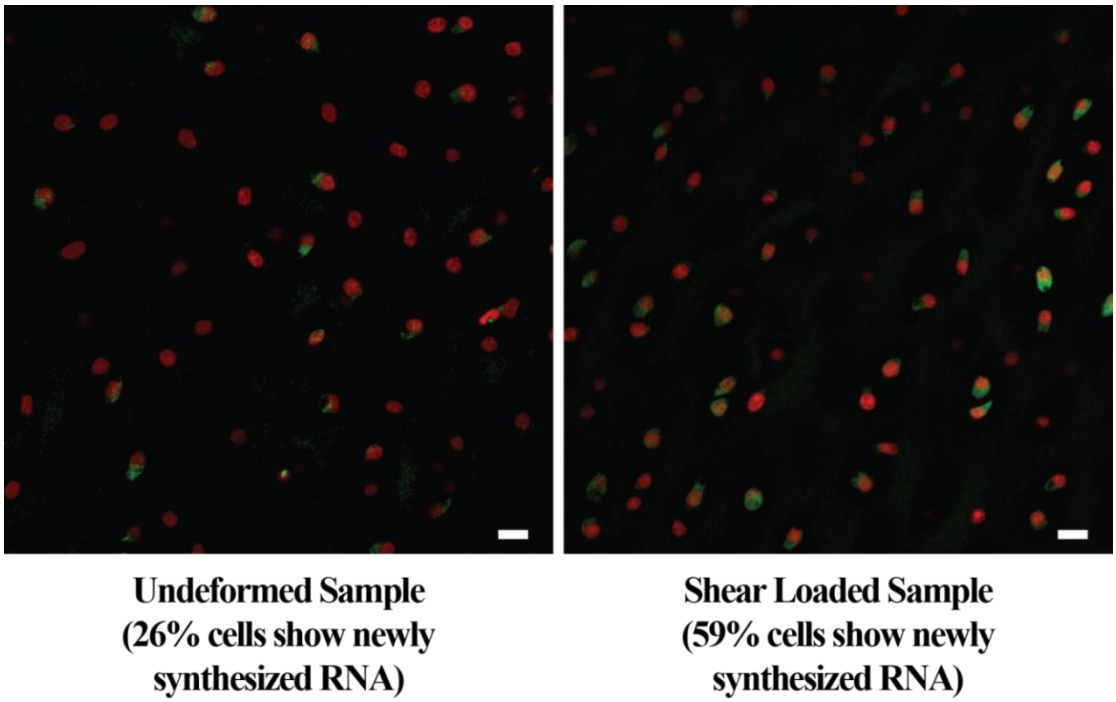

Figure 3.3. Control (non-deformed) tissue explants exhibited a reduce number of cells with nascent RNA expression compared to explants exposed to mechanical shear. The images shown are *z* projections of 20 *z*-slices, and the nascent RNA (green channel) was filtered to eliminate uneven background intensities so that a threshold could be applied to facilitate cell counting. The image post processing was performed with ImageJ (NIH, Bethesda, MD). The control sample showed 14 out of 54 cells (26%) with nascent RNA expression, while mechanical shear of the deformed (treated) sample resulted in 44 out of 75 (59%) cells with nascent RNA expression. Nuclei in Figure 3.4, and 3.7-3.9 were analyzed from this deformed image field of view (Scale bar = 10 μm).

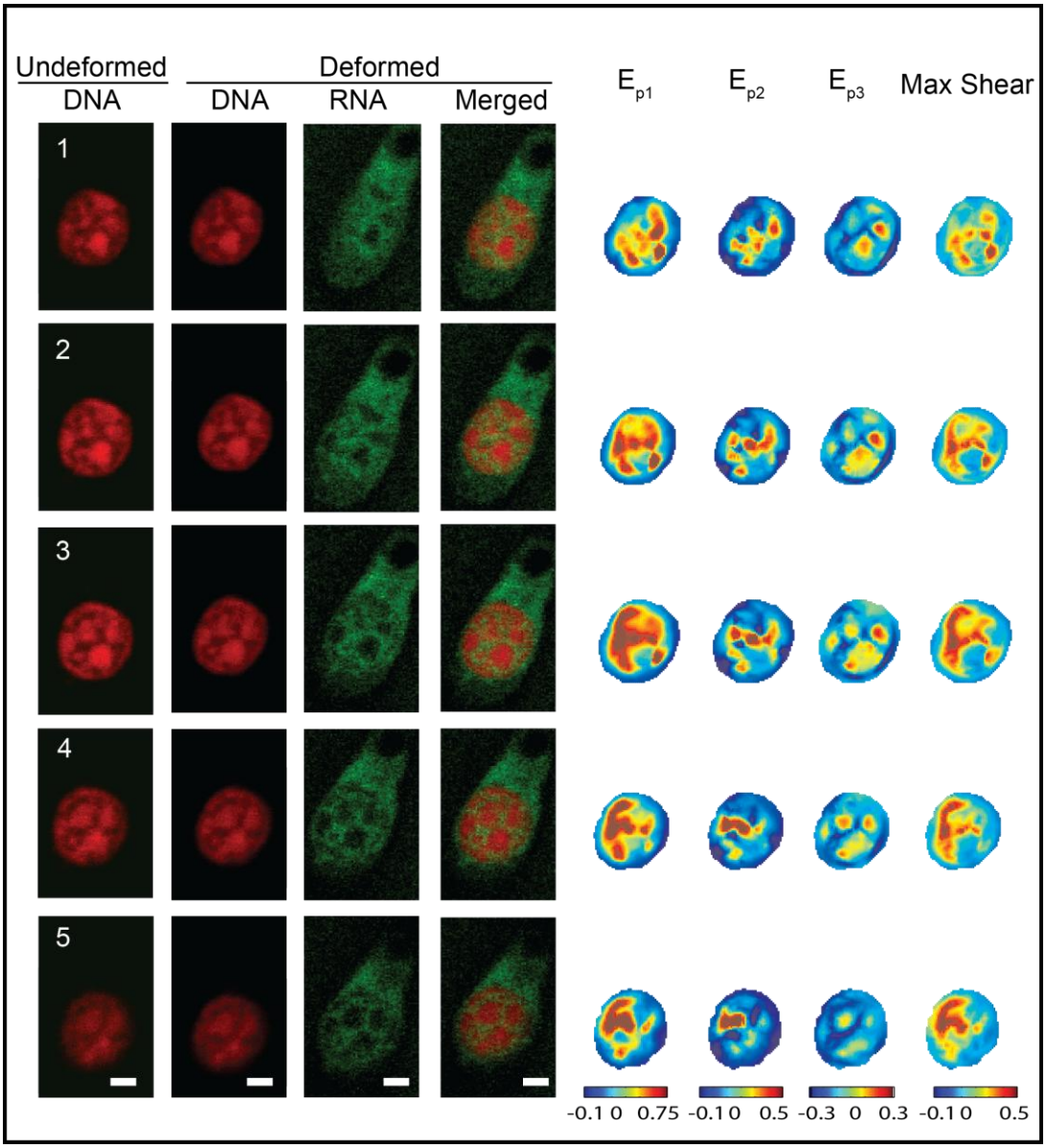

Figure 3.4. Intranuclear strain patterns in a single cell are spatially complex in three dimensions and heterogeneous even during simple shear at the tissue surface. **(a)** Five *z*-slices from an undeformed and deformed nucleus showing nascent RNA and the merged DNA-RNA image. Spatial patterns of strain, and DNA and nascent RNA images, vary by slice location. **(b)** However, overlaid graphs (Figure 8) show that the relationship between strains and RNA or DNA intensity had very little variation between slices. (Scale bars = 2 µm)

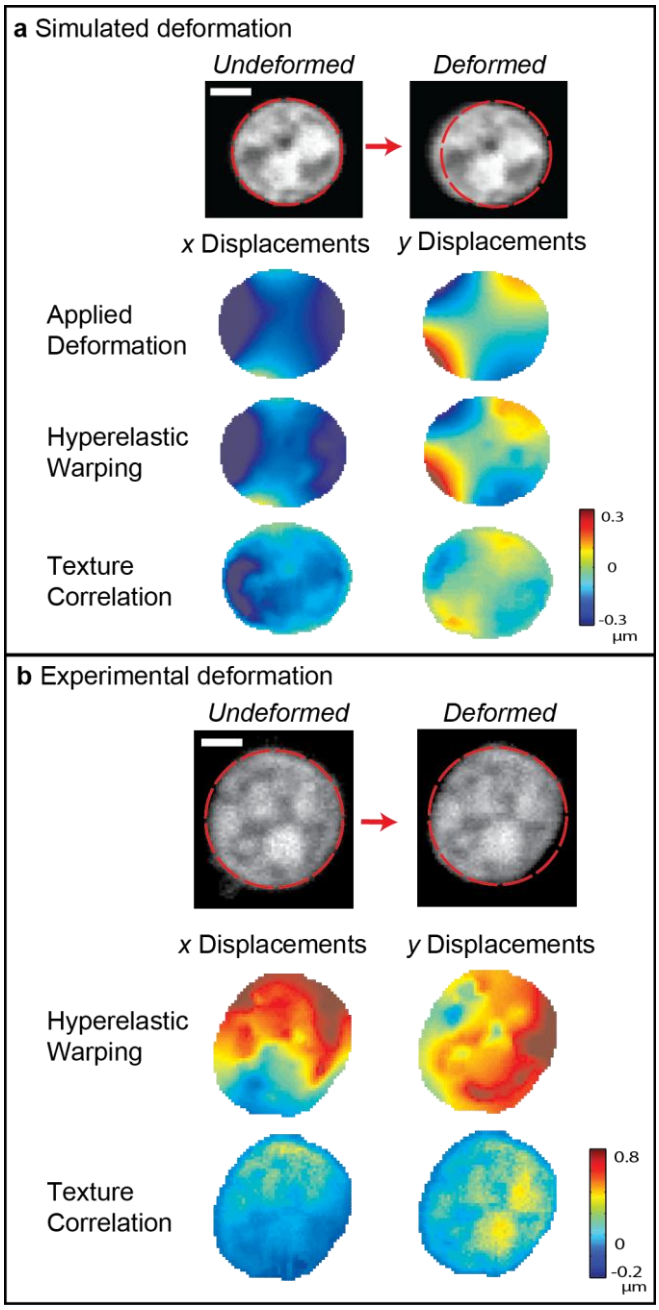

Figure 3.5. Displacement fields from hyperelastic warping, but not texture correlation, match known simulations, thus enabling the measurement of small-scale motion in individual nuclei. **(a)** A simulated deformation was applied to a 3D nucleus, with the middle *z*-slice images shown. The *x* and *y* displacement fields are shown for the known applied deformations, followed by the measured results from hyperelastic warping and texture correlation. **(b)** The *x* and *y* displacement fields from experimental data of a representative nucleus are shown for hyperelastic warping and texture correlation methods. Hyperelastic warping describes deformation with lower bias and increased precision compared to texture correlation (Figure 6). (Scale bars = 2 µm)

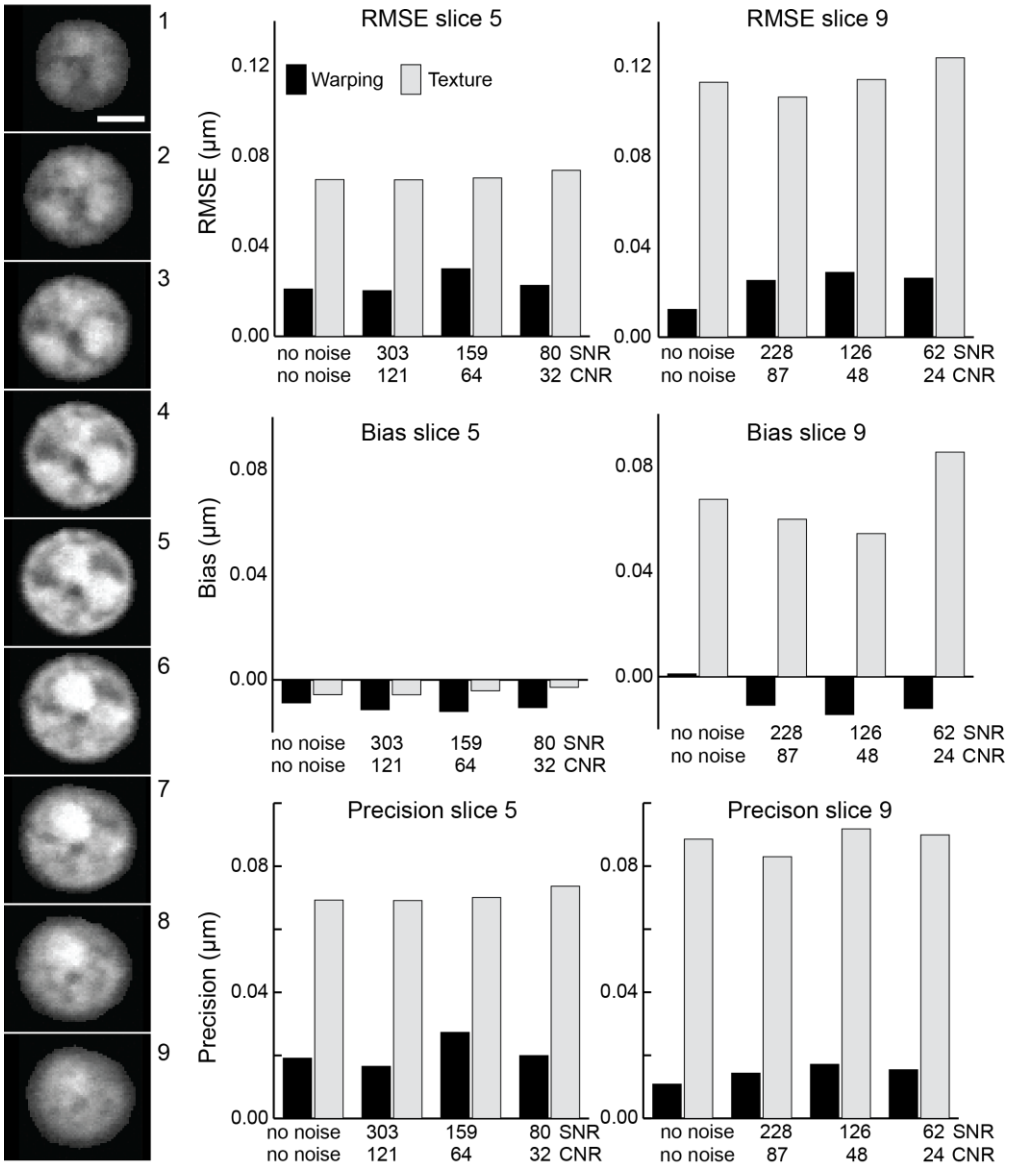

Figure 3.6. Hyperelastic warping consistently provided data with low RMSE and bias, and high precision, compared to texture correlation. Signal-to-noise ratio (SNR) and contrast-to-noise ratio (CNR) were calculated for each image set after the addition of Gaussian (random) image noise. Three error measurements (root mean square error (RMSE), bias, and precision) were used for comparison between the two techniques. The most noticeable difference between the techniques was the increase in bias seen with texture correlation between slice 5 and 9. The other measurements of error show similar performance of the techniques on each image slice. (Scale bar = 2 µm)

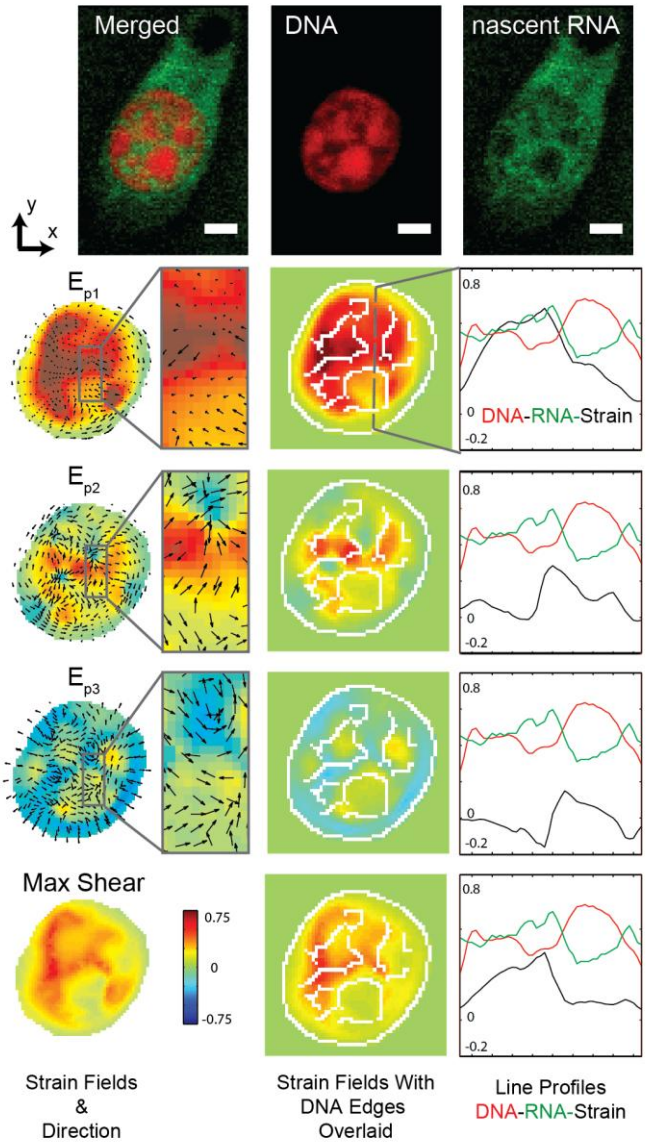

Figure 3.7. Principal strain magnitudes and directions correspond to the intensity of DNA and nascent RNA. A magnification box highlights a nuclear region with heterogeneous (amplified and attenuated) strains. The strain direction for E_{p1} was predominantly through the imaging plane, while the $E_{p2,3}$ directions were largely in the imaging plane. For the nucleus shown, tensile E_{p3} strains correlated with DNA image intensity regions (r^2=0.826), whereas compressive E_{p3} strains correlated with nascent RNA intensity regions (r^2=0.759). While only one representative image slice from the middle of the nucleus is shown, the results were consistent in other *z*-slices (Figure 4 and 8). A single line scan at the right of the strain maps depicts the cross sectional profiles for DNA (red), RNA (green) and strain magnitudes (black). White lines of the strain map are edges of the DNA image intensity calculated by an edge detection function in Matlab to help spatially visualize the high and low DNA regions. (Scale bars = 2 μm)

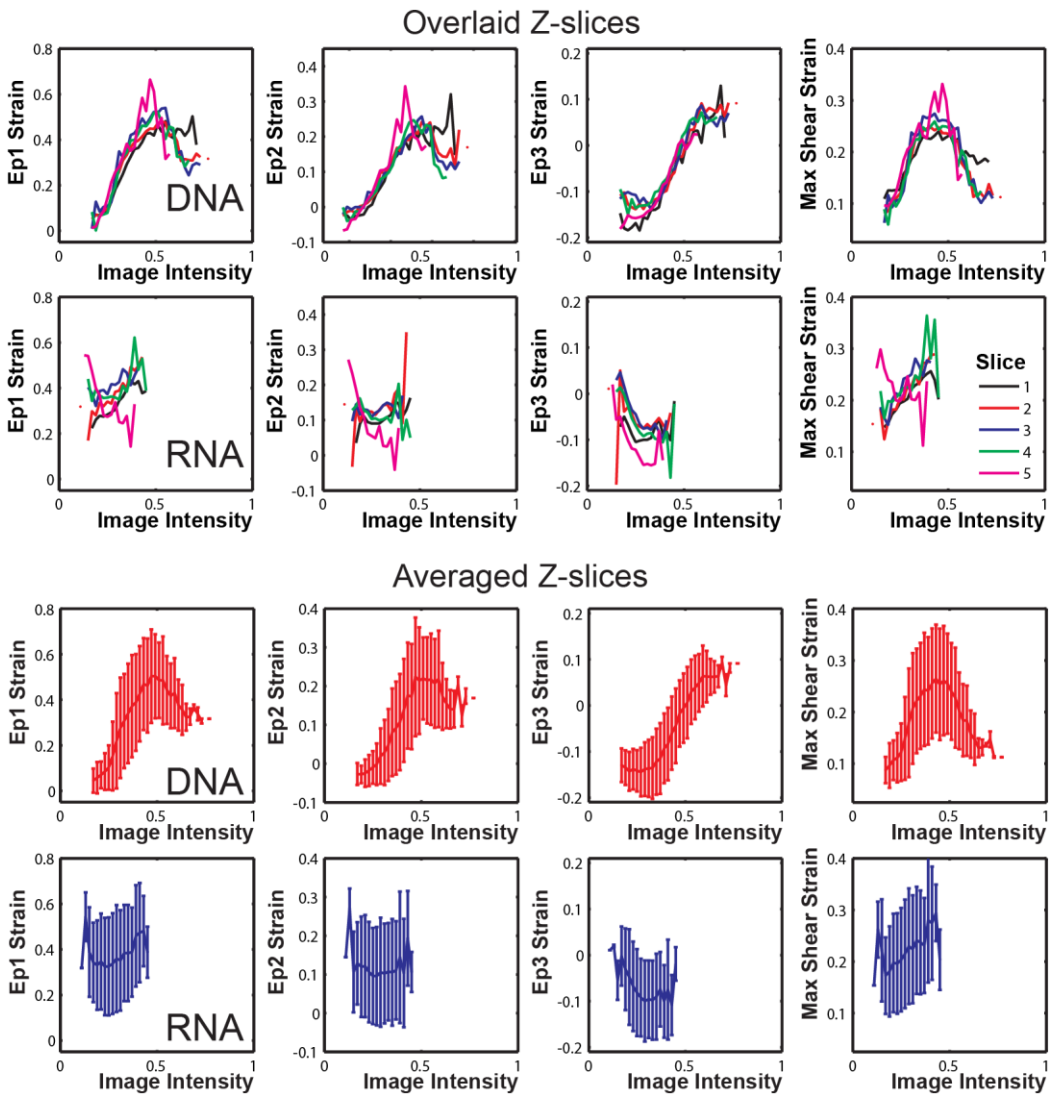

Figure 3.8**.** Complete 3D, DNA and RNA image intensity to strain relationship analysis for a single nucleus from Figure 4. The top graphs shows the image intensity vs. strain results for each z-slice and the bottom graphs are the averaged results.

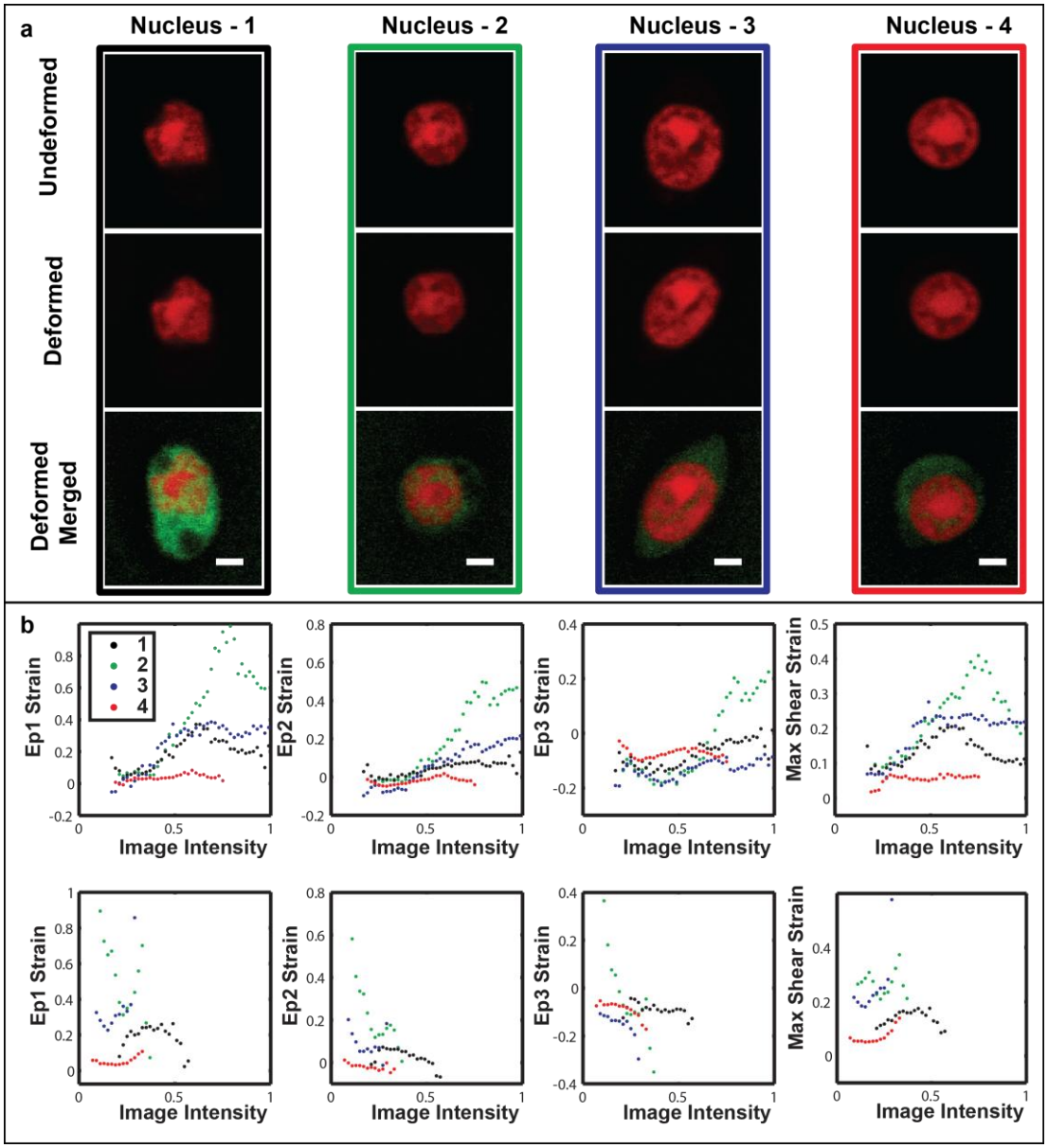

Figure 3.9. Strain magnitudes and nascent RNA expression in nuclei vary among single cells within in a tissue volume subjected to uniform shear. **(a)** The undeformed DNA image, deformed DNA and merged DNA-RNA images are shown for four cells from the same imaging field of view seen in Figure 3. The nuclei were from the same region in the tissue, although there were several physical characteristics, such as shape, size, and long axis orientation that may influence how the strain was transferred from the tissue to the nucleus. **(b)** The average image intensity versus strain for the four nuclei were graphed in matching colors as boxed in **(a)**. Three of the four nuclei (excluding nucleus two) exhibited similar trends in DNA and RNA intensity patterns. The RNA graphs also show that there were different RNA image intensities between nuclei, which were qualitatively observed in panel **(a)**. (Scale bars = 2 µm)

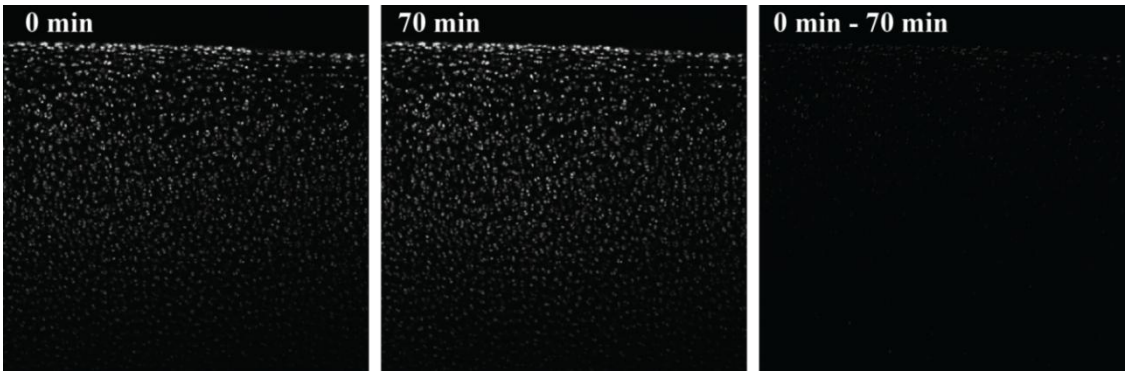

Figure 3.10. Cells remained viable during the time course of experiments. Cell viability was determined using a live/dead imaging kit (Invitrogen) at the beginning (0 min) of the incubation period, and at a later time that exceeded the studies described herein (70 min). A difference image (third panel) demonstrates no change in fluorescence signal in cells.

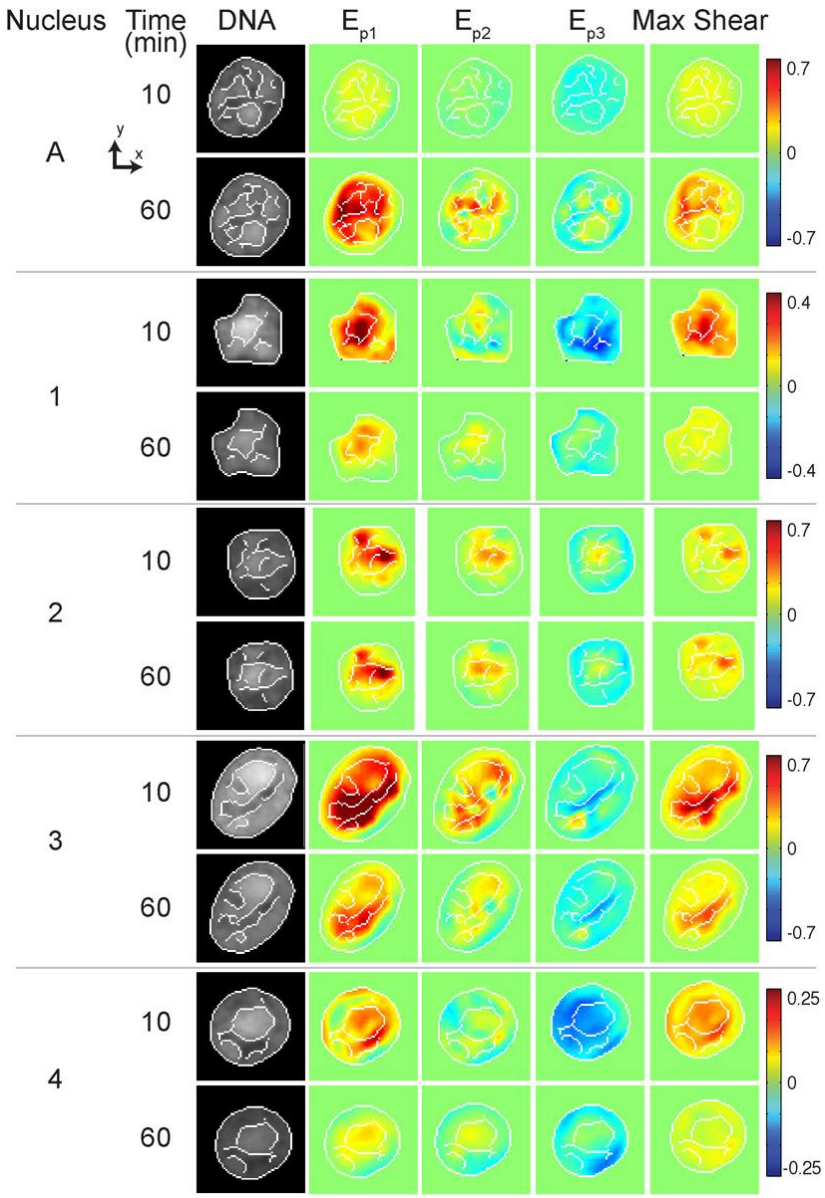

Figure 3.11. The nuclear strain patterns for 10 and 60 minutes after the applied shear loading to the tissue surface varied among cells. Using hyperelastic warping, strain patterns were observed to increase (e.g. nucleus A), decrease (e.g. nucleus 1), or remain unchanged (e.g. nucleus 2) with time Hyperelastic warping measurements provides additional spatial details that the small differences in aspect ratios between 10 and 60 min could not resolve. The small difference in aspect ratio does indicate that the bulk deformation of the nucleus does not change over the experimental time period. The difference in aspect ratios for the slices presented above are: A (-0.008), 1 (0.001), 2 (0.000), 3 (0.006), and 4 (0.064). Please note that nucleus A is also depicted in Figure 7, while nuclei 1-4 correspond to those shown in Figure 9. The white lines were overlaid on the DNA image and strain maps to aid in visualizing the chromatin and interchromatin regions.

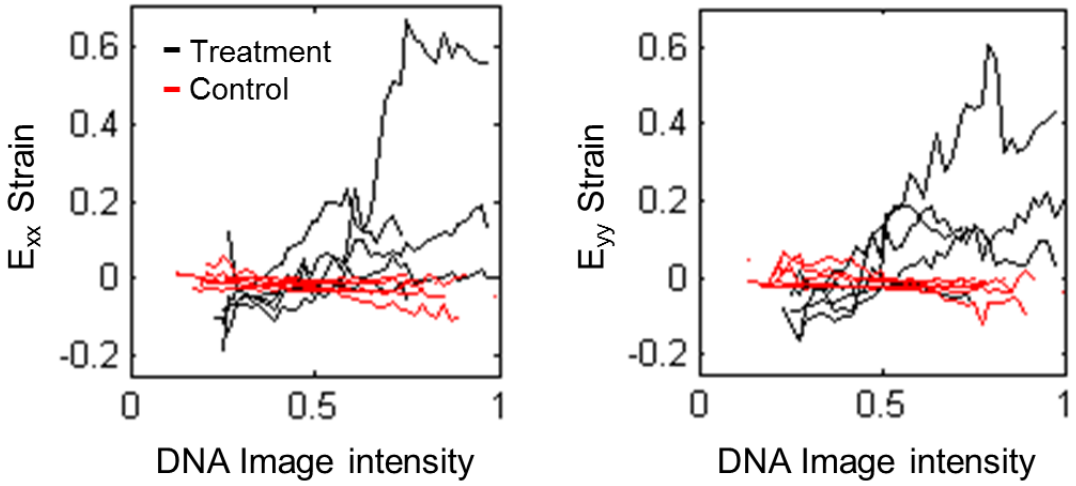

Figure 3.12. Strain versus DNA image intensity plots. The negative control, no tissue deformation (red) nuclei=5, and the treatment, tissue deformation (black) nuclei=5, are plotted for Ex and Ey strain fields of the middle slice of the nuclei. The control nuclei plots are horizontal and show very little changes in strain level with respect to DNA intensity. This shows that there is a low level of internal deformation that the hyperelastic warping measurement technique is detecting in the negative control case. In the applied tissue deformation treatment case there are positive trends of strain to DNA, which varies cell to cell.

CHAPTER 4. VALIDATION FOR MEASURING INTRANUCLEAR STRAIN WITH ITERATIVE WARPING USING DEFORMABLE IMAGE REGISTRATION

4.1 Abstract

The cell nucleus is the stiffest component of the cell. Understand the local mechanics of the nucleus is important to understand how mechanical signal can be transduced to the nucleus and alter chromatin regions and gene expression. Most widely used methods for measuring nucleus mechanics is to measure bulk geometric changes in area and aspect ratios. These values provide not local information that can be spatially correlated to biochemical activity in the nucleus. Iterative warping using deformable image registration is developed to measure local intranuclear strain patterns. A forward finite element analysis was built to great a known deformation "gold standard" that the iterative warping algorithm can be validated with. The forward analysis uses two material properties to represent chromatin and interchromatin regions. The regions material properties were varied between soft and stiff producing a strain field with corresponding pockets of high and low strains. The iterative warping algorithm measured with low error the known deformation patterns in a repeatable way finding the global minimum in the image registration solution space.

4.2 Introduction

The cell nucleus directs the regulation of normal cellular functions as well as the expression of proteins required for adaption to environmental changes. The nucleus can be considered a composite material with the major component being DNA which is classified into two regions 1) heterochromatin regions which are tightly packed and have decreased gene expression activity and 2) euchromatin regions that are lightly packed and have higher gene expression activities[25,52,53]. Mechanical forces are thought to interact with these DNA regions and are an important part in the gene expression process[39,40,70,71].

Current methods to characterize nuclear biomechanics typically rely on bulk measurements. To characterize the nuclear mechanics, microscopy images are taken of the nucleus before and after a treatment and geometric changes in aspect ratio and area is measured. These measurement algorithms are found in many image analyses software packages and provide a quick bulk measurement of the nucleus. However, these methods lack the spatial sensitivity to capture the inherent structural complexity and internal mechanics of the nuclei.

Digital image correlation (i.e. texture correlation) is an approach that provides strain patterns by tracking the unique texture of biological images[50,72,73]. A subset search region of the undeformed image is correlated to a region in the deformed image. The limitation of this technique is that large areas of unique texture are needed. Texture correlation has been used to measure a bulk nuclear mechanics response to a stimulus but lacks the spatial resolution to provide detailed maps of the intranuclear strain[2].

In this study iterative warping using deformable image registration, or warping for short is validated to measure intranuclear deformations. The goal of deformable image registration (DIR) is to match a template image with a target image and obtain a deformation map required to complete registration. DIR has been used in many biological imaging applications such as MRI ultrasound, and microPET imaging to look at the mechanics of the brain and cardiovascular system[7,74]. In DIR a finite element mesh is made of the template image and the mesh is deformed until it matches the target image (Figure 4.1). The deformation or warping of the mesh is governed by the material properties that are assigned. To avoid the registration of getting stuck on predominate features in the image a blurring curve is assigned. The limitation with the load penalty curve is that the registration can be over driven and the solution reaches a local minimum. To find the global minimum, the warping analysis is iterated with incrementing mesh stiffness until there is a reasonable solution found. To validate iterative warping a forward finite element analysis was completed to create a known intranuclear strain field. The objectives of this study are to 1) validate the algorithm in finding the global minimum in the solution space to calculate intranuclear strain fields with the smallest

error and 2) demonstrate the additional spatial information warping provides compared to bulk geometric measurements.

4.3 Methods

4.3.1 Nucleus imaging and forward known data

Passage 4 chondrocyte nuclei images were collected using fluorescent microscopy with the DNA being stained with DRAQ5 (Cell Signaling) or Hoechst 33342 (Life Technologies). Z-projections of confocal or two photon microscopy nucleus images are used in the analysis. When the nucleus is stained the heterchromatin is brighter than the euchromatin due to the compaction of the DNA. For this study the brighter regions are referred to as chromatin and the lighter regions as interchromatin which was set by an arbitrary threshold.

Four sets of images were created with a forward finite element analysis. The mesh was deformed in a finite element simulation with displacement and strain magnitudes representative of those observed in previous studies[2]. The boundary conditions of the model consisted of applying an equal tensile normal force on the outer perimeter. For the forward simulation the nucleus was segmented into chromatin and interchromatin regions (Figure 4.3). The four known data sets were created with chromatin being 2 and 10 times stiffer than the interchromatin and the inverse with the interchromatin being 2 and 10 times stiffer. A linear elastic material model was selected for the forward and warping analysis.

4.3.2 Iterative warping using deformable image registration

The iterative warping algorithm reaches a solution by increasing mesh stiffness and load penalty curves. For each of the DIR iterations there is a normal or error termination which is recorded as a 1 or 0 as seen in Table 4.1, respectively. There are six load penalty curves that the warping algorithm runs in parallel and the mesh stiffness is increased until all six reach a normal termination which is seen as the last row for each of the nuclei in Table 4.1.

A Matlab code was written to automate and connect the software for mesh generation (TrueGrid), DIR (nike3D) and post processing (WarpLab and LSprePost). By using the Matlab code the above iterative optimization routine can be performed in a more manageable time frame, tens of minutes instead of hours for one nucleus. Figure 4.2 provides a visual comparison of the computer mouse movements and clicks that the user saves by the semi-automated Matlab algorithm.

4.3.3 Measurement of error in hydrostatic strain fields

The forward finite element stimulations were used to create known strain fields and served as the "Gold Standard" in the determination of the Root Mean Square Error (RMSE) for iterative warping. The error is qualitatively visualized as the known minus warped difference image (Figure 4.4). Quantitatively the RMSE for known minus measured warped is plotted for the different load curves and mesh stiffness. Also measured is the RMSE of the warped template minus target images. This measure serves as a way to identify when the global minimum is reached (Figure 4.5). In the post processing of the results the total strain distribution is segmented into the percentage of strain carried by the chromatin or interchromatin. Also, plotted is the normalized DNA intensity versus strain at each pixel of the nucleus (Figure 4.5). Lastly, the percent error is calculated for the average, min, and max hydrostatic strain as: $\% \, Error = \frac{measured - known}{known} \times 100$ (Table 4.2).

To compare the results to current methods for nuclear mechanics the engineering strain, change in aspect ratio and area was measured for the template and target images (Figure 4.7). Engineering strain is calculated as the ratio of the change of the major axis over the original major axis length.

4.3.4 Visualizing strain fields

There are several was to represent the strain fields in continuum mechanics (Figure 4.1). Directional strains with respect to Cartesian coordinates in a 2D case are E_{xx}, E_{yy}, and E_{xy}. From the directional strains, strain invariants I_1 and I_2 are calculated and are directional independent. $I_1 = E_{xx} + E_{yy}$ $I_2 = E_{xx} \times E_{yy} - E_{xy}^2$ The hydrostatic strain (E_h) is also

directionally independent and is the average of E_{xx} and E_{yy} or one half of I_1 . The hydrostatic strain can be thought of as the local volumetric changes and was chosen as the strain that will be presented in the figures of this study.

4.4 Results

In the validation analysis the four nuclei deformations from the forward simulation were registered and qualitatively and quantitatively analyzed to determine a percent error. The number of stiffness iterations varied from 2 to 9, to reach 6 normal terminations for the 6 different load curves (Table 4.1). The difference images of the known minus measured warped results show a very good spatial registration for each of the nuclei qualitatively (Figure 4.4). The RMSE for known minus measured deceases and levels off as the mesh stiffness is increased (Figure 4.5). The average of the hydrostatic strain is insensitive to both the changes of mesh stiffness and load curve penalty. The standard deviation does increase with increasing penalty but decreases with increased mesh stiffness (Figure 4.5). The percent error for warping varies between nuclei from over-estimating the average hydrostatic strain by 1.42% to underestimating by 3.24 % (Table 4.2).

To quantify the percentage of the total strain that is distributed between the interchromatin and chromatin components, the stain distributions were analyzed based on a pixel by pixel method or by chromatin segmentation. The warped images show intranuclear strain patterns that match the interchromatin to chromatin stiffness ratios and DNA intensity segmentation (Figure 4.4). The scatter plots of normalized DNA intensity versus hydrostatic strain show similar trends among the pair of chromatin being stiffer or interchromatin being stiffer (Figure 4.6). Qualitatively the strain distributions histograms show the total distribution as a composite of the interchromatin and chromatin portions of the strain. This is quantitatively reported as a stacked bar graph with nucleus chromatin to interchromatin ratio as 25/75 nucleus A, 7/93 nucleus B, 15/85 nucleus C and 30/70 nucleus D (Figure 4.6).

Comparative measurements were made between iterative warping and other bulk geometric measures such as engineering strain, changes are aspect ratio and area. The warping average strain results were nearly identical to the known averages (Figure 4.7).

The engineering strain of the major axis underestimated the average strain for all the nuclei. However, the engineering strain measure was more reasonable than the change in area or aspect ratio measurements which were near zero or dramatically off, respectively.

4.5 Discussion and Conclusions

Iterative warping using deformable image registration measured low error in the intranuclear strain fields created by a forward finite element analysis. Although texture correlation was not used in this validation study, in previous single material validation study, it was used and warping was found to have a lower error[2]. Using a two component nucleus in this validation allowed for a more complex intranuclear strain field with high strain pockets that theoretically better match what is known about the relative mechanics between euchromatin and heterochromatin[75]. The forward simulation with the interchromatin being 10 times stiffer and acting as a shell with no chromatin pockets of high or low strains may be a reasonable estimation because the nucleus is a multi-component material with several structural components such as lamins that are not considered in this validation study.

The strengths of iterative warping are that a large amount of spatial intranuclear deformation is gained and the analysis is semi-automated. The automated iterative process has taken out the guess-and-check procedure of finding DIR parameters that appear like they will give a reasonable solution. It dramatically reduces the time to find a solution by incrementing the mesh stiffness while running in parallel the 6 warping analyses load curves which reproducibly behaves the same way during the stiffness sweep (Table 4.1). There is currently no other technique that can measure the complex intranuclear strain patterns that were simulated in the forward analysis at such a high spatial resolution. By looking at the overlaid perimeter outlines in Figure 4.3, it would appear that the nuclei were deformed in a very similar manner. The method comparison bar graphs, Figure 4.7, quantitatively show that the simple bulk geometric measurements cannot distinguish the complex intranuclear strain information found in the different nuclei.

The weaknesses of this approach are the large solution times and sensitivity to image quality issues. It takes substantially more time to process a single nucleus because a the FE mesh is customized for each nucleus compared to bulk image processing measurements that can measure hundreds of nuclei in a single run. The large amount of data that is gained is worth the effort if processing a relatively low number of nuclei. But for population responses in the thousands, this would be a very computationally expensive process. To get the detailed intranuclear strain fields, high resolution microscopy images are need of the nucleus with good textured quality. Other bulk measurement techniques can have very poor image quality and the results will not change much. A good example of this is where hundreds of nuclei are imaged at low resolution with a high light source that saturates the detector and the image can still be processed. The bulk measurements may not be altered with this imaging setup, but running a warping analysis would be impractical.

A few considerations when running iterative warping is in the preprocessing of the nucleus and selection of the starting mesh stiffness. The warping analysis looks for large image gradients, so when making the mesh it has been found useful to make the mesh a few pixels larger than the nucleus, and this will provide a large gradient for the start of the registration process. Caution has to be made when interpreting the results at the edge of the nucleus because this is where the largest errors are seen (Figure 4.4). As seen in Table 4.1, not all of the nuclei have the same stiffness sweep. To save time when running multiple nuclei from the same experiment, a wider stiffness sweep performed to find a starting point for the mesh stiffness.

Future improvements would be to automate the mesh generation of the nucleus and to do other fine tuning of the post-processing of the analysis. Also, depending on the anticipated material response, other material types such as hyperelastic or temperature dependent properties could be added to the mesh material properties. This analysis will be beneficial in work that focuses on the interactions between mechanical stimuli and biochemical reactions at the intranuclear level, potentially elucidating the mechanotransduction mechanisms affecting the nucleus.

Table 4.1. Warping image registered normal termination for max penalty and mesh stiffness (Pa). Image Registered Yes =1 No = 0

Nucleus A	Max penalty					
Stiffness (Pa)	1	1.5	2	2.5	3	3.5
350	1	0	0	0	0	0
400	1	1	0	0	0	0
450	1	1	0	0	0	0
500	1	1	1	0	0	0
550	1	1	1	0	0	0
600	1	1	1	1	0	0
650	1	1	1	1	1	0
700	1	1	1	1	1	0
750	1	1	1	1	1	1

Nucleus B	Max penalty					
Stiffness (Pa)	1	1.5	2	2.5	3	3.5
350	1	1	1	1	1	0
400	1	1	1	1	1	1

Nucleus C	Max penalty					
Stiffness (Pa)	1	1.5	2	2.5	3	3.5
350	1	1	1	1	0	0
400	1	1	1	1	1	0
450	1	1	1	1	1	1

Nucleus D	Max penalty					
Stiffness (Pa)	1	1.5	2	2.5	3	3.5
350	1	0	0	0	0	0
400	1	0	1	1	0	0
450	1	1	1	1	1	0
500	1	1	1	1	1	0
550	1	1	1	1	1	1

Table 4.2. Hydrostatic strain error analysis statistics

Known			
Nucleus	mean	min	max
A	40.93	34.75	48.73
B	25.71	4.59	43.45
C	33.08	21.7	42.38
D	22.45	15.17	30.66

Measured			
Nucleus	mean	min	max
A	39.6	19.65	49.4
B	24.84	3.72	48.33
C	32.89	18.22	50.62
D	22.77	11.55	34.06

% Error			
Nucleus	mean	min	max
A	-3.24	-43.45	1.37
B	-3.38	-18.95	11.23
C	-0.57	-16.03	19.44
D	1.42	-23.86	11.08

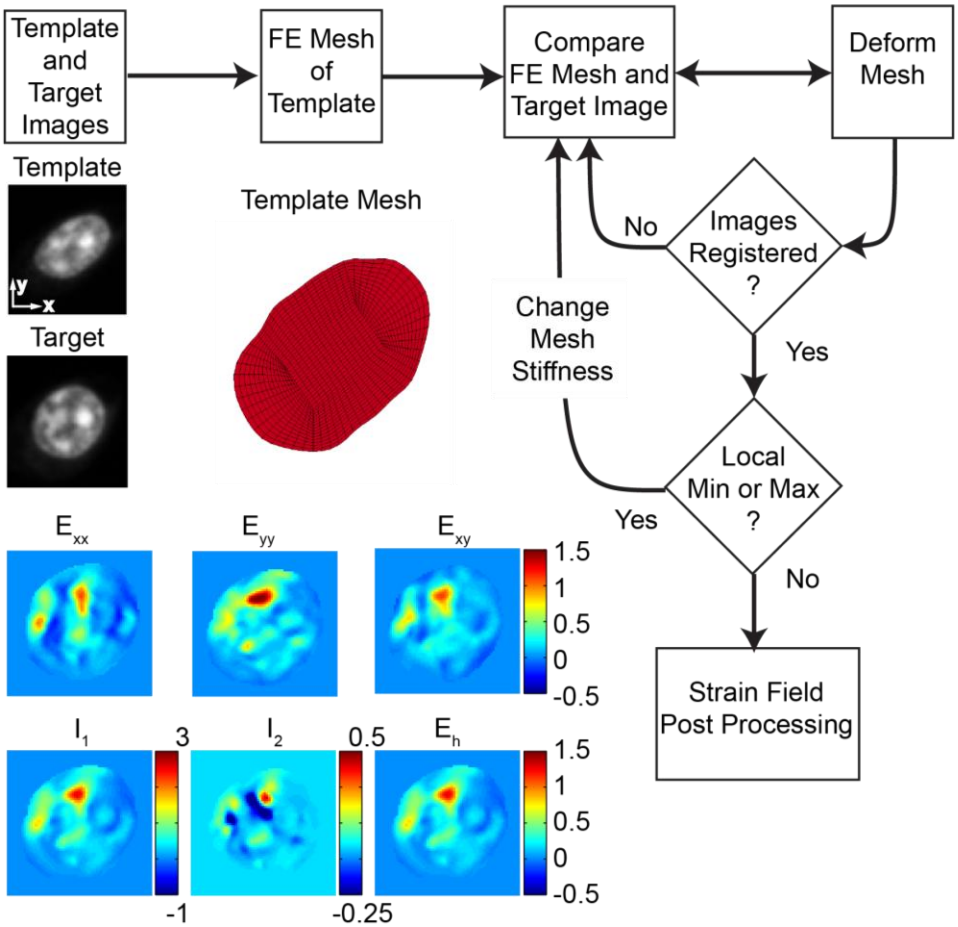

Figure 4.1. Iterative warping using deformable image registration measures the deformation between two nucleus images (Template and Target). An iterative procedure has been developed to optimize image registration through an automated algorithm that increments the mesh stiffness until a reasonable solution is found. The deformation can be visualized in several ways, 1) directional strain fields in Cartesian coordinates (E_{xx}, E_{yy} and E_{xy}) 2), strain invariants (I_1, I_2) or 3) hydrostatic strain (E_h) both being directionally independent and calculated from the directional strain fields.

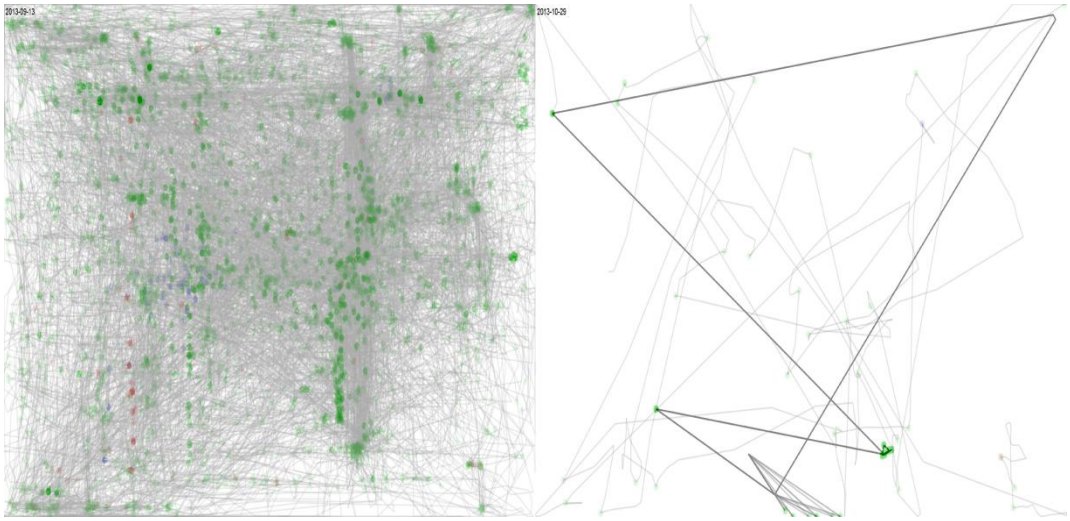

Figure 4.2. Visual comparison of the recorded computer screen mouse movements and clicks during the manual analysis (left) and after the semi automation Matlab algorithm was developed (right).

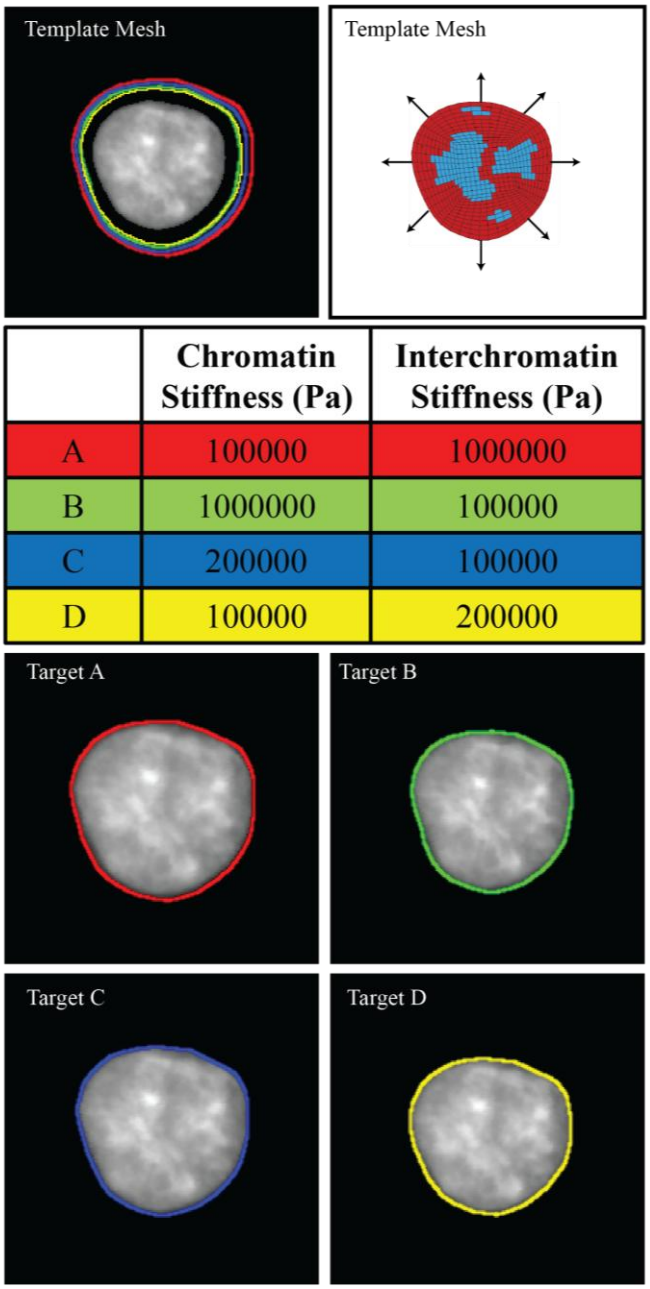

	Chromatin Stiffness (Pa)	Interchromatin Stiffness (Pa)
A	100000	1000000
B	1000000	100000
C	200000	100000
D	100000	200000

Figure 4.3. Four target images (A-D) were made with a forward FE model that applied and equal normal force out ward on the perimeter of the mesh (arrows on mesh) to be used as the known standard in validating warping to measure intranuclear strains. The nucleus was segmented into a chromatin region (Template Mesh-blue area) and an interchromatin region (Template Mesh-red area). The chromatin or interchromatin mesh stiffness was defined to be 2× or 10× stiffer, respectively, as shown in the figure above. The color coded target perimeters are overlaid on the Template Mesh image.

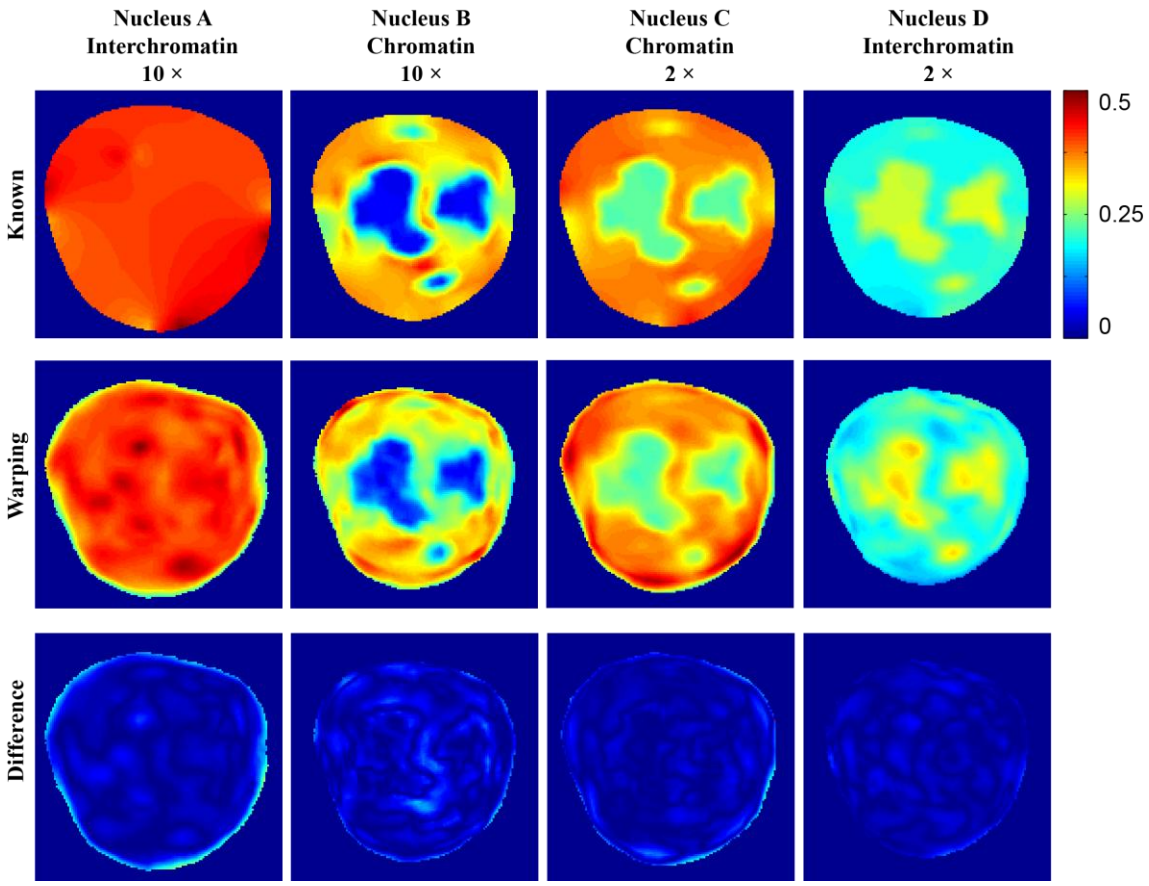

Figure 4.4. Qualitatively seen in the nearly zero difference images, the hydrostatic strain fields measured by iterative warping closely match the known forward analysis for all four of the nuclei. There are slight edge artifacts where the image was not completely registered which are seen as a few brighter pixels near the edge of the nucleus in the difference image.

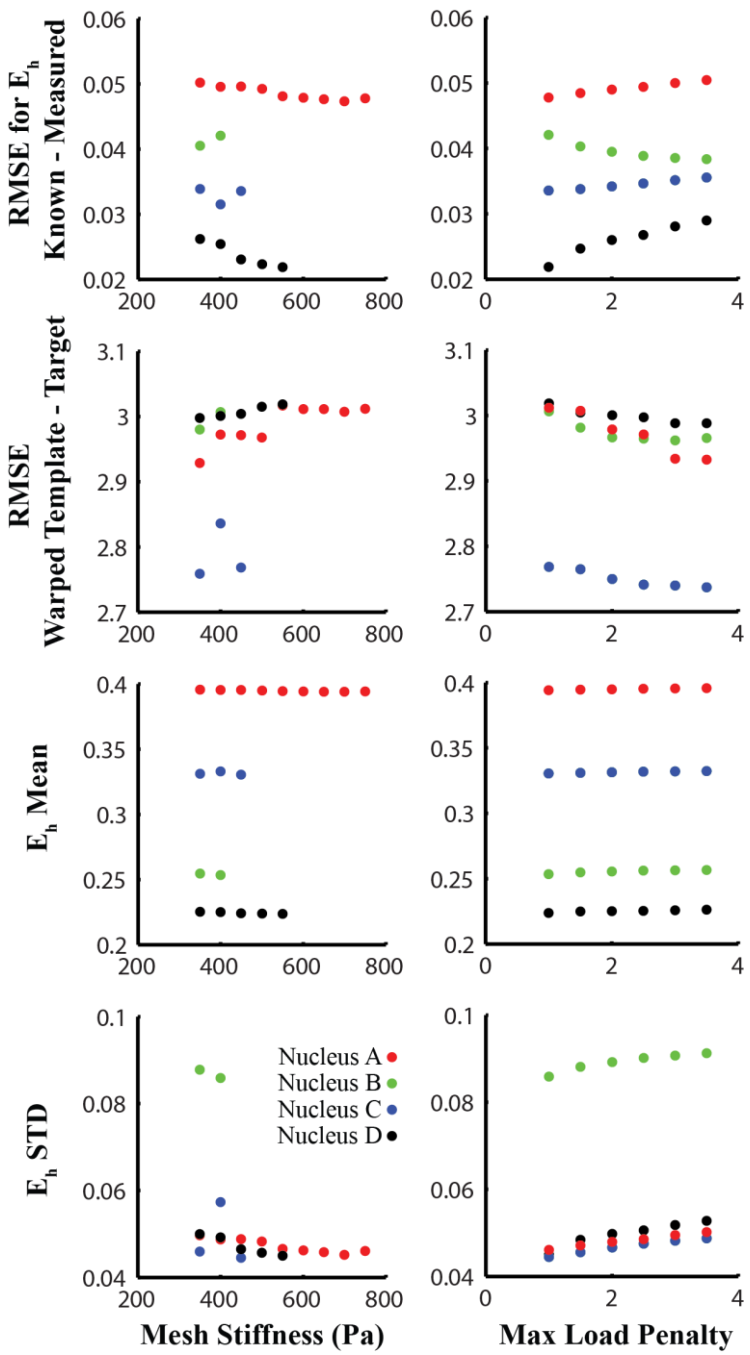

Figure 4.5. Two independent variables, mesh stiffness and max load penalty, were varied to find the combination that minimizes the error in the hydrostatic strain measurements. The RMSE for known-measured hydrostatic strain and the RMSE for the warped target-template images are plotted to find the global minima in the solution space. The mean of the hydrostatic strains are not influenced by the changes in the mesh stiffness and load penalties. Whereas, the standard deviation of the strains changes with mesh stiffness and load penalties.

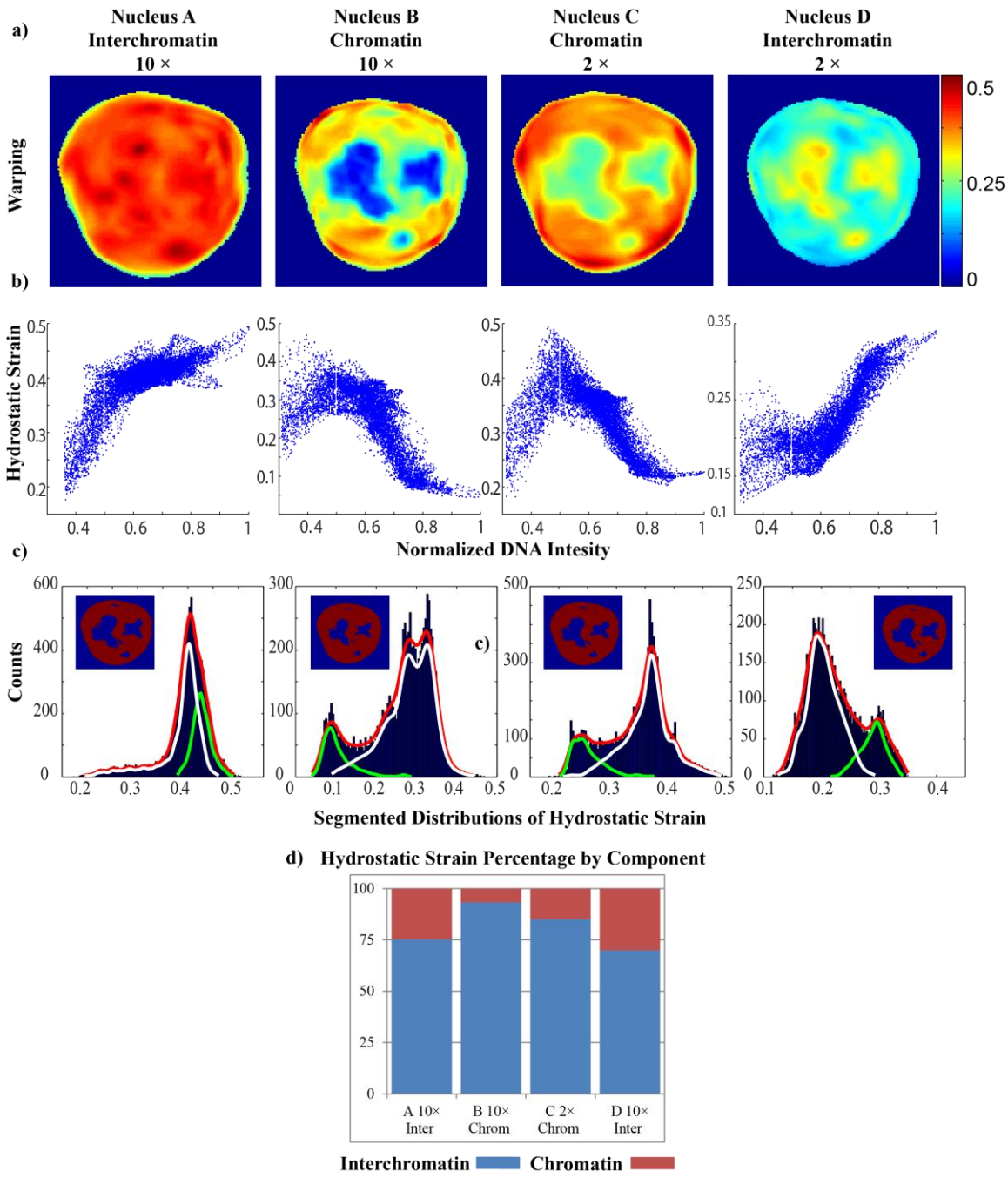

Figure 4.6 Intensity versus hydrostatic strain (b) is plotted and similar trends are seen among the interchromatin stiffer A and D nucleus and the chromatin B and C nucleus. Segmentation of the nucleus images into interchromatin and chromatin regions show how the total strain distribution, blue histogram (red line), is a composite of the two strain distribution chromatin (green line) and interchromatin (white line). To quantify the percentage of the total strain that is distributed between the interchromatin and chromatin components, a stacked bar plot is shown for each of the four nuclei.

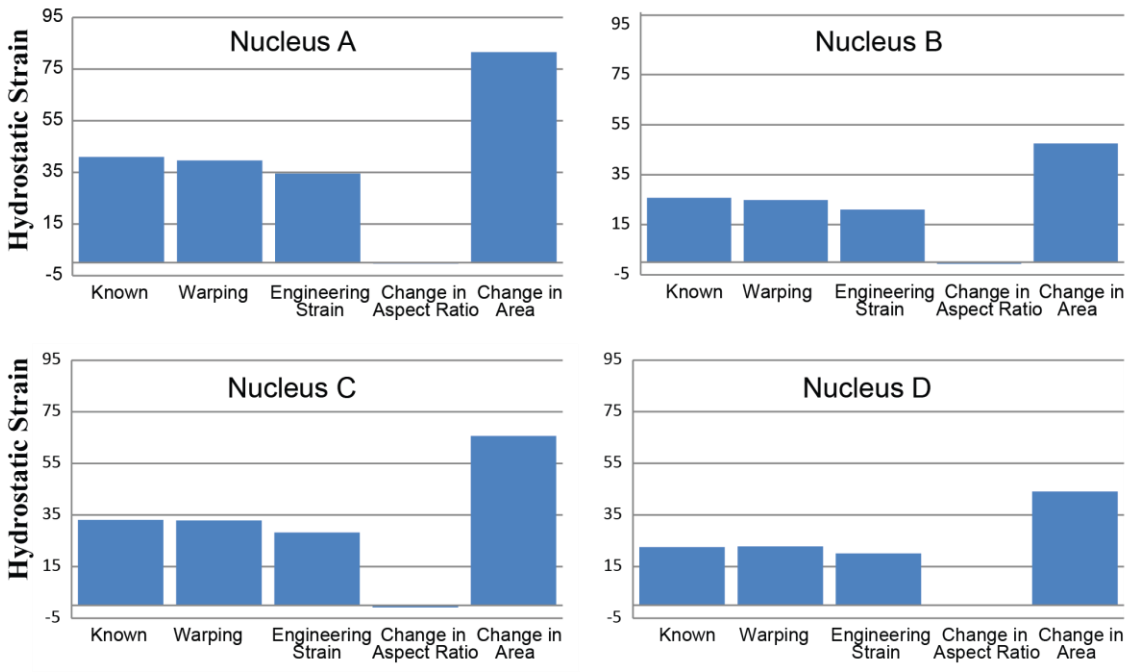

Figure 4.7. With all four nuclei, the mean hydrostatic strain measured by iterative warping is closest to the known mean compared to the other bulk measurement techniques (engineering strain for the major axis, change in aspect ratio and change in area).

CHAPTER 5. DEDIFFERENTIATION OF CHONDROCYTES INFLUENCES INTRANUCLEAR STRAIN TRANSFER MEASURED BY WARPING DEFORMABLE IMAGE REGISTRATION

5.1 Abstract

Mechanical cues are important for cellular processes and in regulating gene expression by influencing chromatin compaction. Cellular shape, size and gene expressions are known to change with cells as they are passaged in 2D cell cultures. Previous cell substrate stretched experiments have measured minimum strain transfer to the nucleus using bulk measurement techniques. It is not known how strain is transferred to the intranuclear structures because previous measurement techniques have low resolution strain maps. Warping image registration provides high resolution intranuclear strain maps that can spatially correlate chromatin strain regions. In this study passage zero (P0) and passage four (P4) chondrocyte cells are subjected to equibiaxial stretch on untreated and collagen I treated substrates. There was an increase in strain transfer ratio as the cell dedifferentiated from P0 to P4 with no significant difference between treated or untreated substrates. Using warping to measure intranuclear strains provides new data to how strain is locally distributed between chromatin and interchromatin regions when under stretch and how it changes due to dedifferentiation.

5.2 Introduction

The nucleus is sometimes represented as a mechanically isolated stiff cellular organelle. Recent studies have started to demonstrate that the nucleus is in fact not mechanically isolated from the cell[76,77]. Several proteins have been found to be nuclear membrane bound proteins that connect the underlining nuclear lamins and chromatin structures to the cytoskeleton and cytoplasmic structures. The chromatin structures can mainly be divided into euchromatin, lightly packed and active in gene transcription, and

heterochromatin, dense and less active in gene transcription. The integrity of the nuclear structures is important for cellular activities and the disruption of them can cause severe diseases such as laminopathies which is a group of genetic disorders caused by the disruption of nuclear lamina[77-79].

Several studies have focused to understand how the cell regulates mechanical cues from the local environment to the nucleus. With cells in deformed cartilage plugs it has been measured that the bulk nuclear deformation is dependent on the location of the cell in the depth varying cartilage structure[28,80,81]. Mechanical properties such as stiffness have been measured for the nucleus with micropipette aspiration and the results were modeled to calculate strain transfer through the cell to the nucleus[82] . There are also other experimental methods with isolated cells on stretchable substrates that measure intracellular and nuclear deformation with texture correlation[50]. Texture correlation is an image pixel passed correlation of deformed images with spatial resolution limits and accuracy based on size of unique texture in the image[83]. Because the intranuclear structures are small and lack unique image texture it is difficult to measure a high resolution strains. An alternative to pixel based correlation is finite element modeling based on deformable image registration (DIR)[64]. With DIR the registration quality is related to mechanical model parameters and how the solution space is searched for the best deformed registration (chapter 4).

The objective of this study is to use iterative warping deformable image registration to measure intranuclear strain transfer of cells on stretchable substrates. Two hypotheses will be tested: 1) is there a difference in strain transfer based on cell differentiation state, and 2) does the substrate coating affect the strain transfer. To test cellular dedifferentiation chondrocytes at passage zero (P0) and passage four (P4) will be used because it is well characterized that chondrocytes dedifferentiated into a fibroblast phenotype over passages[84]. The substrates tested will be an untreated and a collagen I coated substrate.

5.3 Methods

5.3.1 Cell staining and imaging

Primary bovine chondrocytes from the weight bearing region of the medial condyle were harvested from young cows less than 6 months old. To visualize the structural differences between passage zero and passage four cells on the substrates coated with or without collagen I the following staining procedures were used. The cells were sparsely plated and incubated on the substrates for 24 h to allow for complete adhesion to the substrates. The cells were fixed with 2% paraformaldehyde, washed with 1 x PBS, and then permeabilized with 1% trition and washed three times with 1x PBS. The actin cytoskeleton was fluorescently labeled with Alexa488-phollodin (Invitrogen, Life Technologies). The nucleus was labeled with Hoechst stain. Microscopy was performed using a Widefield Nikon inverted microscope with a 60 X 1.20 na with 1.5 magnification with the appropriate filters for Alexa488 and Hoechst dyes. The substrates with the fixed cells where inverted onto a cover slip for viewing, because the short working distance of 60X objective was insufficient to view threw the substrates.

5.3.2 Quantitative Real-Time PCR - qPCR

Total RNA has been extracted from cultured primary chondrocytes using the AurumTM Total RNA Mini Kit (Bio-Rad Laboratories) following the user's manual for cell cultures. Amount of isolated RNA has been determined by spectrometry using the NanoDrop ND-1000 (Thermoscientific Fischer). cDNA has been synthesized via iScriptTM Reverse Transcription Supermix for RT-qPCR (Bio-Rad Laboratories) and the thermocycler CFX96 TouchTM (Bio-Rad Laboratories) using between 400 and 1000 ng RNA per reaction. For every sample, the concentration of cDNA was adjusted to 1 ng/µl. Quantitative Real-Time PCR has been performed using the SsoAdvancedTM Universal SYBR® Green Supermix (Bio-Rad laboratories) with a final concentration of 5 µM for each primer and 3 ng cDNA template per 20 µl reaction. The cycling protocol was as follows: 95°C for 30s, 40 cycles of 95°C for 10s and 56°C for 25s; melting curves were determined by raising to temperature from 65°C to 95°C with 0.5°C increments between read outs. A custom MATLAB code has been written to calculate initial fluorescence

intensities (theoretical fluorescence intensity from initial number of templates) which can be determined from amplifications curves using sigmoidal curve fitting analysis[85].

Primer pairs were designed such that at least one partner was binding to an exon-exon junction and/or be separated by at least one intron, if possible; exclusions: COMP, SUN2 and LMNB2 because no exon information was available for the bovine genome and COL2A1 as no specific primers could be found with such premises. However, melting curves were specific and showed no signs of primer dimerization or genomic DNA contamination. All primers were specific for all known isotypes besides primer for TTN (titin) that were specific for the N2A-isotype. Suitable housekeeping genes have been found using the Genevestigator gene expression databank tool (https://www.genevestigator.com/gv/) by searching for stable genes between chondrocytes and fibroblasts, as with ongoing passages cells seem to recapitulate a fibroblastic phenotype. Potential candidates selected were CSNK1A1, HPRT1 and RPL10A of which HPRT1 showed the most stable expression with >1% change in gene expression between fresh isolated and passage 4 chondrocytes. All primer sequences can be obtained from the list below.

5.3.3 Device calibration

The device to deform the substrate and image the strain transferred to the nucleus is a modified Flexcell stage device. The StageFlexer purchased from Flexcell International Corp was modified in several ways. The first modification was to convert it from a vacuum device to a positive pressure device by placing a cap above the substrate Figure 5.1. The second modification was to drill out the bottom support bracket under the loading post to allow for a 40X Olympus water dipping objective with a 3.5 mm working distance to fit inside the device to view the cells prior and post deformation. The magnitude of the substrate stretch varied linearly with change in pressure which was controlled by a pressure regulator ran with program in Labview. To calculate the substrate deformation, a Matlab code was implemented that tracked the displacements of the nuclei centroids. To validate the Matlab code to accurately calculate the substrate

deformation fluorescent spheres were used as fiducial markers and measured by tracking the centroids and with digital image correlation.

5.3.4 Cell stretching experiments

Cells were plated on substrates 24 h prior to the stretching experiments. DNA was stained with Hoechst prior to loading the membranes onto the StageFlexer. A small amount of silicone lubrication was applied to the loading post followed by the substrate which was covered with 3 ml of L-15 cell culture imaging media. Two photon microscopy (740 nm wavelength and 250 mW power) was used to take three z stack images three minutes apart prior to loading using a 40X water dipping objective. Two images were captured the cell image, by transmitted light, and the nucleus images by the Hoechst stain. The substrate is stretched and the cells are relocated within 5 to 10 minutes of the applied stretch and three more images are taken (Figure 5.1). Equibiaxial strain is calculated from the average engineering strains e_{xx} and e_{yy}, which are measured by tracking the nuclei centroid as fiducial markers.

5.3.5 Nuclear strain measurements

To measure the nuclear strain fields, z projection of the nucleus were used in the warping analysis. Briefly, warping analysis uses deformable image registration to calculate the local deformations of the nucleus. The process to optimize the warping analysis parameters to minimize the error in the strain fields was determined from a blinded known digitally applied deformation study (chapter 4). Nuclear dynamics was established by observing cell movement during the three pre-stretched nuclei images. Any cells that were moving prior to stretching were not included in the analysis. The nuclear deformation due to the membrane stretch was measured between the images just prior to and post substrate stretch (Figure 5.1).

Image segmentation was done by a Matlab code. The DNA nuclear image was threshold at 65% of max intensity for all the images. The bright regions were called chromatin and lighter areas interchromatin. The threshold was arbitrary selected as seen in Figure 5.4. Chromatin nuclear regions are typically characterized in the literature as euchromatin and heterochromatin, with euchromatin being more tightly packed then heterochromatin.

This classification would mechanically imply that euchromatin is stiffer and therefore must have a lower stain than heterochromatin, which may not be the case.

5.4 Results

5.4.1 Morphological Differences

To measure geometric differences P0 and P4 cells were plated on treated and untreated substrates. The cells were fixed and stained for actin and DNA. Cell and nuclei area and aspect ratio were measured and found to be significantly different between P0 and P4 on both substrates (n=100 to 170, $p < 0.05$) (Figure 5.2A-C). The cells shape for P0 were mostly spherical with cellular and nucleus aspect ratios near 1 and had an actin shell distribution around the periphery of the nucleus. This is phenotypical for chondrocytes. P4 cells were non spherical and had phenotypical fibroblast focal adhesion structures. The actin stain showed organized actin stress fibers all throughout the cell.

5.4.2 Shift in Gene expression

To confirm the shift in differentiation from P0 to P4, chondrogenic and fibroblastic gen markers have been analyzed. Indeed, all chondrogenic expression markers (SOX9, ACAN, PRG4, COMP and COL2A1) were significantly reduced and all fibroblastic markers (COL1A2, VIM, S100A4 and Thy1) showed and high increase up to >10,000 fold in P4 cells compared to P0 cells (Figure 5.3). To better understand the observed changes in nuclear area and aspect ratio, gene expression of nucleoskeleton components has been furthers investigated. Generally, a decrease in nucleoskeletal gene expression can be observed. Nuclear envelope proteins that provide nuclear stability like Lamin A/C, obscurin, MAN1 and titin show an high down regulation of their respective genes from 63% (LMNA) to 95% (LEMd3). This would suggest a softening of the nucleus toward P4. Similarly, LINC-complex proteins Sun1 and Nesprins show significant decrease in gene expression from 77-86%, which leads to the expectation of a decrease strain-transfer to the nucleus. In contrast, LINC-complex gen Sun1 as well as the structural protein emerin sowed no significant decrease after passaging. Lamin B proteins are known to be ubiquitously expressed between various cell types and differentiation states and seem to

play a crucial role in cell survival, similar expression levels between P0 and P4 were therefore expected.

5.4.3 Strain Transfer Ratios

Using iterative warping intranuclear strain patterns were measured from undeformed and deformed nucleus images taken immediately prior and post substrate strain. The nucleus image was segmented into chromatin and interchromatin regions by making a mask of the nucleus based off of 65% max nuclear intensity, respectively. The strain field distribution was measured for the total area or for each of the masked regions, chromatin or interchromatin. Two strain fields with total and regional distributions are provided in. The nucleus area, and chromatin patterning differs between these two nuclei. The smaller nucleus is a P0 and the larger nucleus is a P4 cell. P0 compressive regions are spatially correlated to the chromatin regions and the majority of the tensile regions are spatially correlated to the interchromatin. Between the P0 and P4 cells in Figure 5.4, the interchromatin and chromatin distributions switch when looking at the P4 cell. Figure 5.4 is provided to show a visual measure of how the total strain distribution can be spatial correlated to the different, user defined, structures in the nuclear image. The exact distributions vary from cell to cell.

Knowing the substrate strain and intranuclear strain for each nucleus a strain transfer ratio is measured. For each of the experimental factors (cell passage and substrate coating) at least 5 substrates were stretched with 2-9 cells in the same imaging area for each experiment. A total of 111 nuclei were analyzed with P0, n=20 and P4, n=22 on the untreated substrates and P0, n=34 and P4, n=34 on the collagen treated substrates. Strain transfer ratios (STR) were calculated as the average intranuclear hydrostatic strain divided by substrate equibiaxial strain. The STR is calculated for the different areas of the nucleus total area, interchromatin and chromatin regions (Figure 5.5). There is a significant increase in STR for all the measured regions between P0 and P4 cells. With the P0 chromatin area on average is related to a compressed region and interchromatin to tensile regions. In contrast the P4 strain transfer ratio for all the regions is tensile but as

seen in Figure 5.4 this does not mean there are not local compressive regions. Those regions are just a smaller percentage of the strain distribution.

5.5 Discussion and Conclusion

The primary findings of this paper are made possible because of the newly developed iterative warping measurement of intranuclear strain fields. By knowing the applied substrate strain a STR is calculated which increases from P0 to P4 and is not sensitive to the substrate coatings selected in these experiments. In summary of the results as seen in Figure 5.6, there is an increase in cell area, aspect ratio and actin organization that may all aid in transmitting more strain to the nucleus in P0 (chondrocyte) versus P4 (dedifferentiated fibroblasts) by allowing the cell to attach to the substrate more firmly. Another possible factors contributing to a higher STR is the decrease in chromatin condensation, making the cell less dense. Also, the decrease in nuclear envelope gene expressions would mean a less stiff cell. Especially lamin A, which decreases by 63%, is known to be the main contributor to nuclear stiffness. In contrast, the decrease of LINC-complex protein gene expression would theoretically indicate a lower STR. The decrease in nuclear connections to the cytoskeleton might be to protect the "soft" nucleus from rupturing in consequence to strain transfer overload as the cell dedifferentiates and deformed in different mechanical environments. However, the effect of nuclear softening might outweigh or even be the reason of the observed increase STR.

The strength using warping is that high spatial resolution strain fields can provide a higher resolution stain map of the nucleus compare to other bulk measurements. In a similar cell substrate stretching experiment, texture correlation was used to calculate a bulk STR to the nucleus by only measuring a few points in the nucleus[50]. That study reported STR around 0.17 to 0.38 depending on orientation of the cell because the uniaxial substrate stretched. Using warping to measure intranuclear strain we not only have an average nucleus response but can also measure interchromatin and chromatin STR which varied and had a much larger range even giving negative STR ratios (Figure 5.5). The negative STR can possible be attributed to active cellular remodeling of the nucleus and not a passive strain transfer. In the texture correlation paper the measured

average nuclear strains around 2% with max values around 8%. To generally compare our average stains were around 2 and we had similar STR for the total nucleus, but the high pockets of strain measured with warping can reach max values round 10-30% tensile or compressive stain. If the STR values around 1-2 would be measured if these max pockets are used in the analysis. However, a measure of STR is convoluted because there are so many other active mechanics that can cause the nucleus to deform that the deformation measured might not be from the applied substrate strain.

Some example of nuclear shape regulation is seen by regulating cell shape with micropatterns[86]. Other active methods of nuclear deformation are by knocking out nucleoskeletal components such as lamin-A/C[87,88]. In this study the shape and genes expressions changes for chondrocyte dedifferentiation are similar to previously results[32,84]. Cell regulated nuclear shape or changes in gene expression for nuclear structures and dynamics are confounding mechanism as an explanation for why there is an increase STR from P0 to P4. There appear to be no difference with the selected substrate coatings but it is well known that some cell types are very sensitive to substrate stiffness and coatings for attachment[6].

There is large cell to cell variability even with in the same imaging area during substrate stretching. Some of the variability could be because of active remolding mechanics. However, other passive strain transfer variables such as how firmly and directionally the cell was attached to the substrate were not possible to measurable in this experimental setup. Substrate bead force traction microscopy or micro-post force experiments could provide a measure of cellular adhesive force explaining variability in cell populations. Future studies are needed to tease apart these underling mechanisms of intranuclear mechanics that regulate how a cell can sense and transmit local mechanical cues to the nucleus for gene expression and other cellular activity.

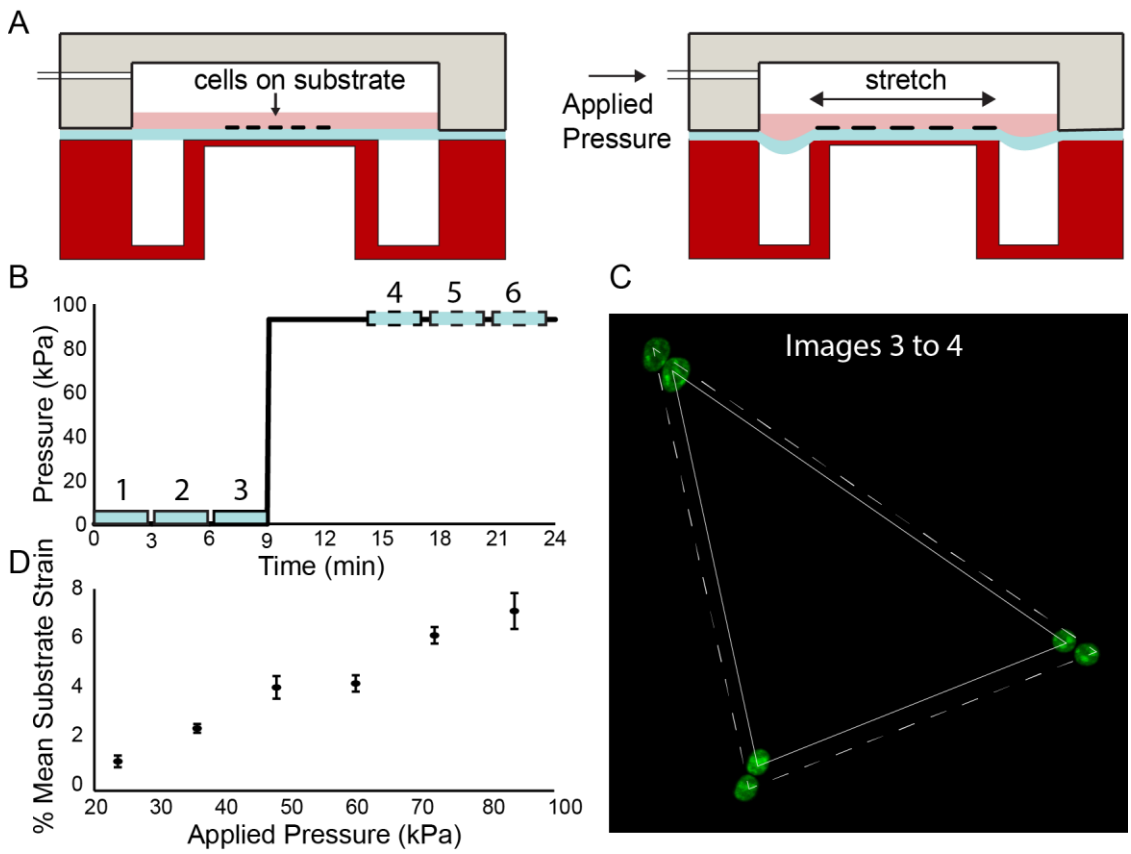

Figure 5.1. A) Microscope mountable device to visualize deformed nuclei of cells attached to a substrate that is stretched over a loading post when a positive pressure is applied. B) To watch for cell dynamics six images are taken (blue boxes), three before and three after the pressure is applied. C) An equibiaxial strain is applied to the substrate translating the cells outwards as visualized by the green stained nuclei. D) A calibrate curve was made to validate the device that with increasing the applied pressure there is an linear increase substrates mean hydrostatic strain ($R^2 = 0.977$).

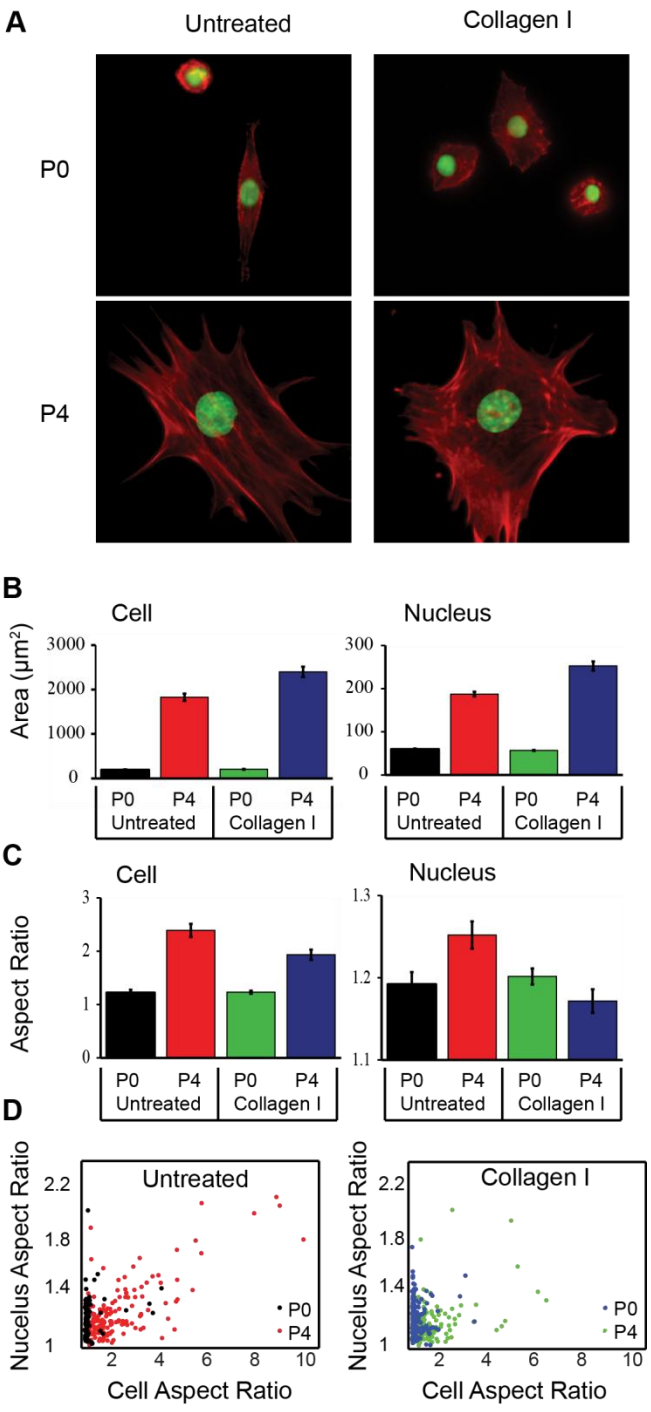

Figure 5.2. A) There is a distinct visual morphological difference between passage zero (P0) and passage four (P0) cells and nuclei (red=actin, green=nucleus, n=100 to 170, $p < 0.05$). However, there is very little difference in cell and nuclei area B) and aspect ratio C) when they are platted on untreated or collagen treated substrates. D) Cell aspect ratio versus nucleus aspect ratio show similar trends between untreated and collagen treated substrates.

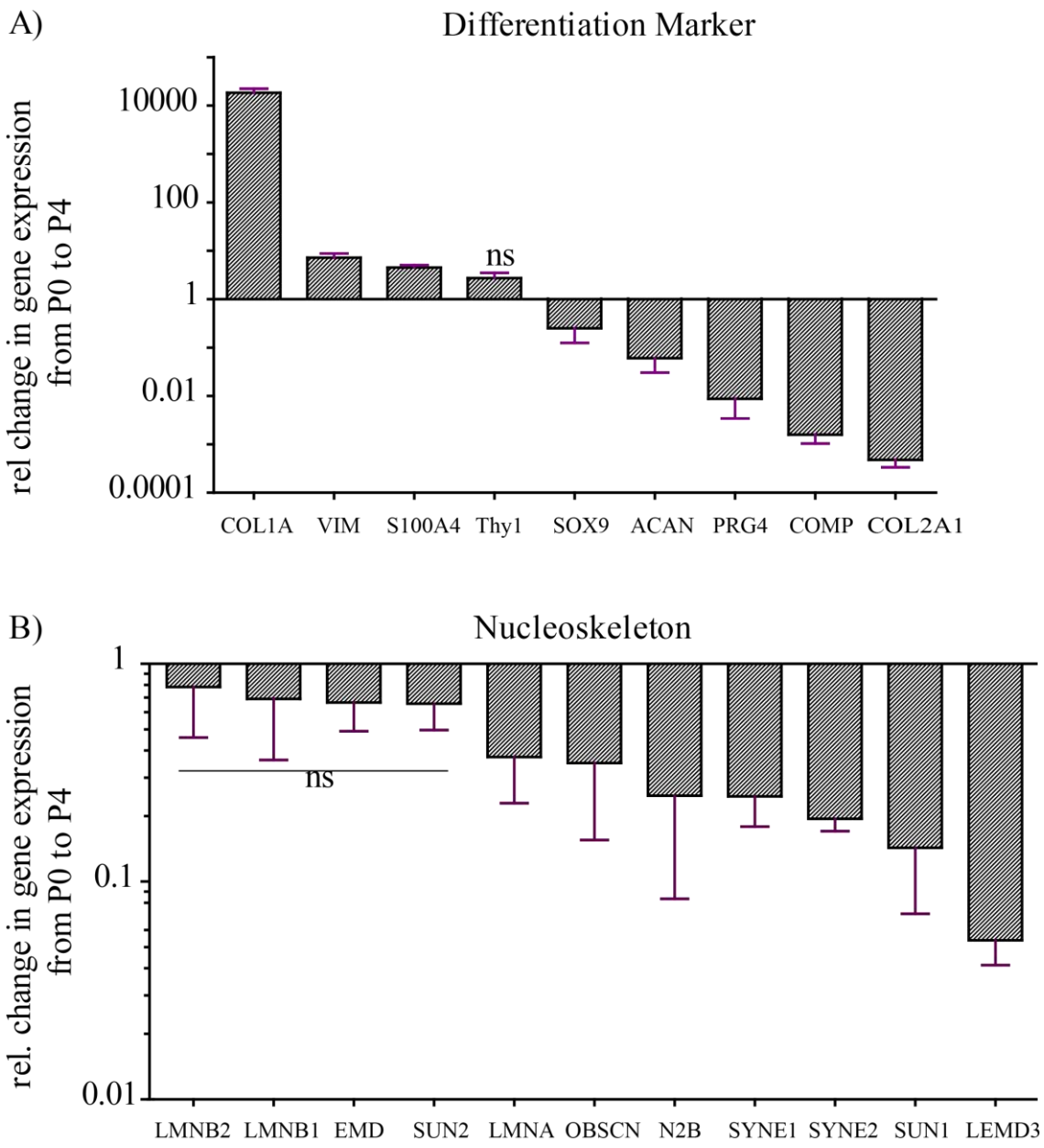

Figure 5.3. Change in gene expression of passage 4 chondrocytes relative to fresh isolated cells for A) markers of differentiation and B) nucleoskeleton components. Error bars represent SEM. Changes are significant from 1.0 ($p<0.05$) if not indicated as (ns non-significant) as verified via post-hoc t-test; n=4.

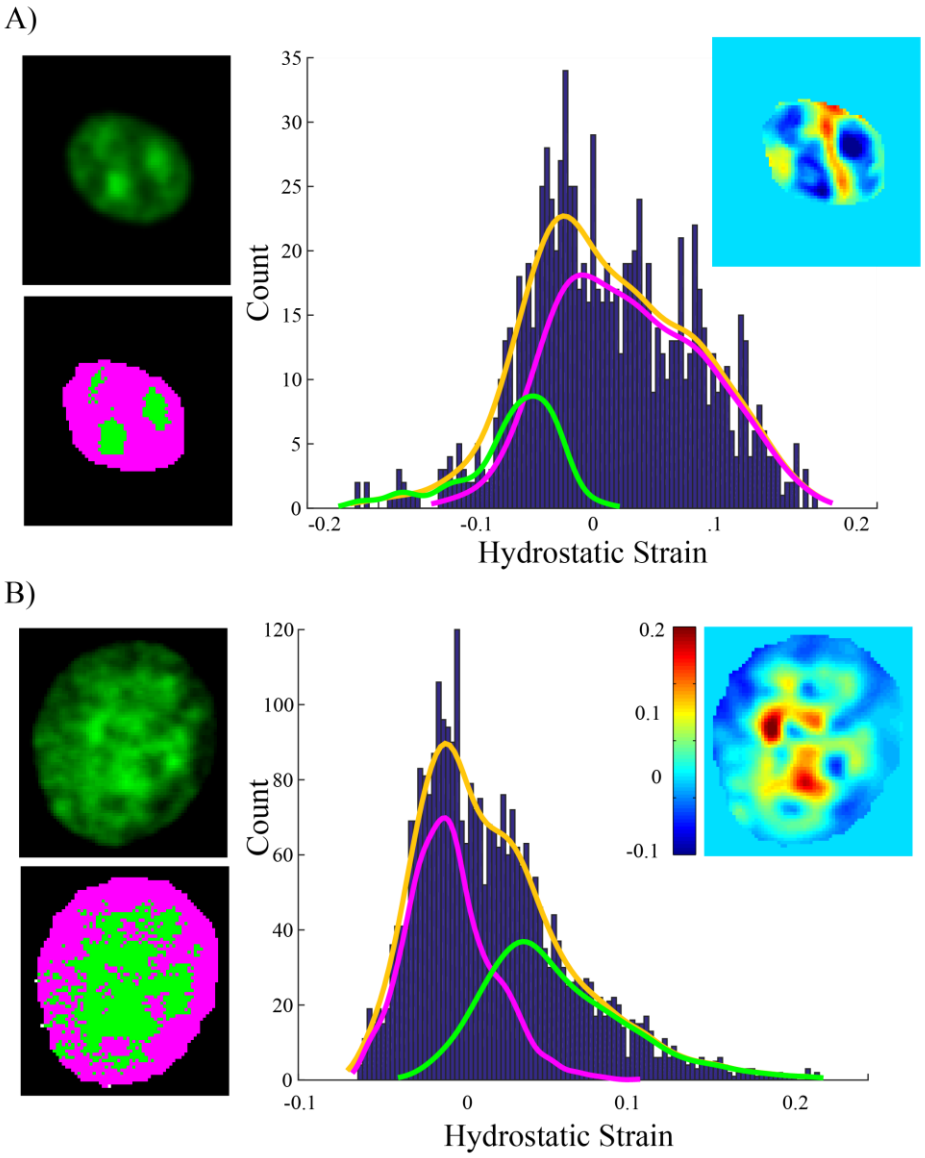

Figure 5.4. Strain distributions for two nuclei (A=P0 and B=P4) with different patterns of chromatin regions that are segmented according to the pink and green mask. The histograms fitted with the yellow line are the total distribution of hydrostatic strains. The pink (chromatin) and green (interchromatin) lines correspond to the strain distribution of the pink and green areas in the masked nucleus (histograms not shown). Note that the chromatin and interchromatin distributions switch sides of the total distribution.

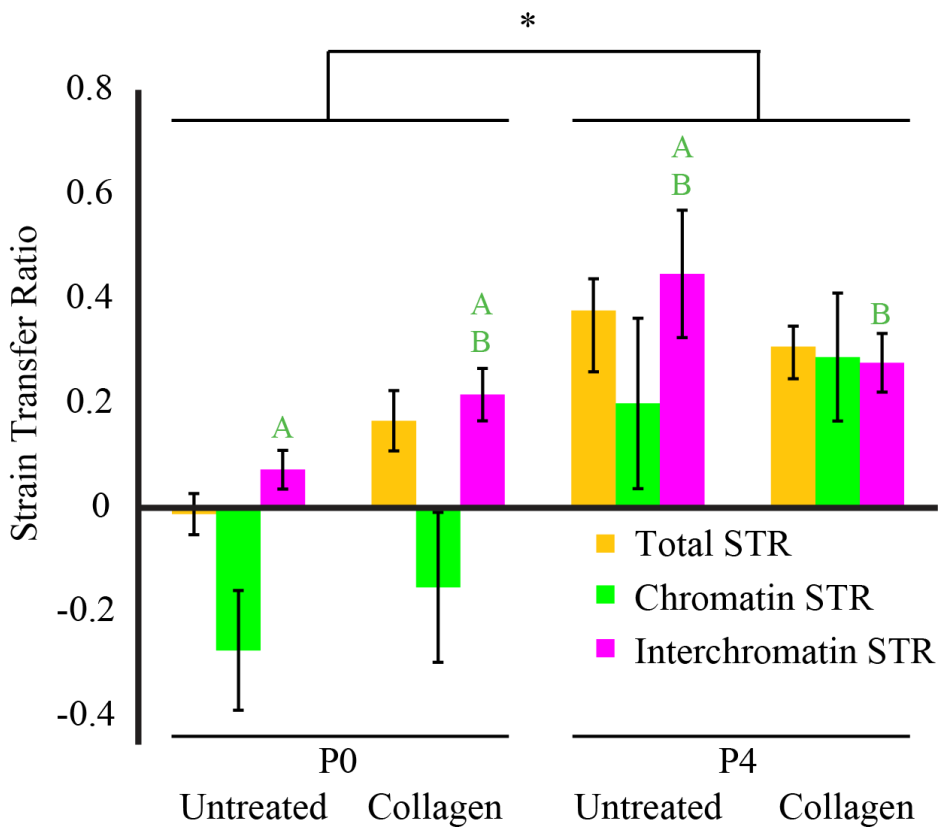

Figure 5.5. Strain Transfer ratio is calculated as the mean hydrostatic strain for the region of interest divided by substrate strain. The STR regions of interest are interchromatin, chromatin, and the total nucleus areas and example of two strain distributions is seen in Figure 4. There is significant difference in the STR between P0 and P4, but not the substrates. The interchromatin STR was on the only measure that had a significant interaction between substrate and passage. (n=20-35, $p > 0.05$)

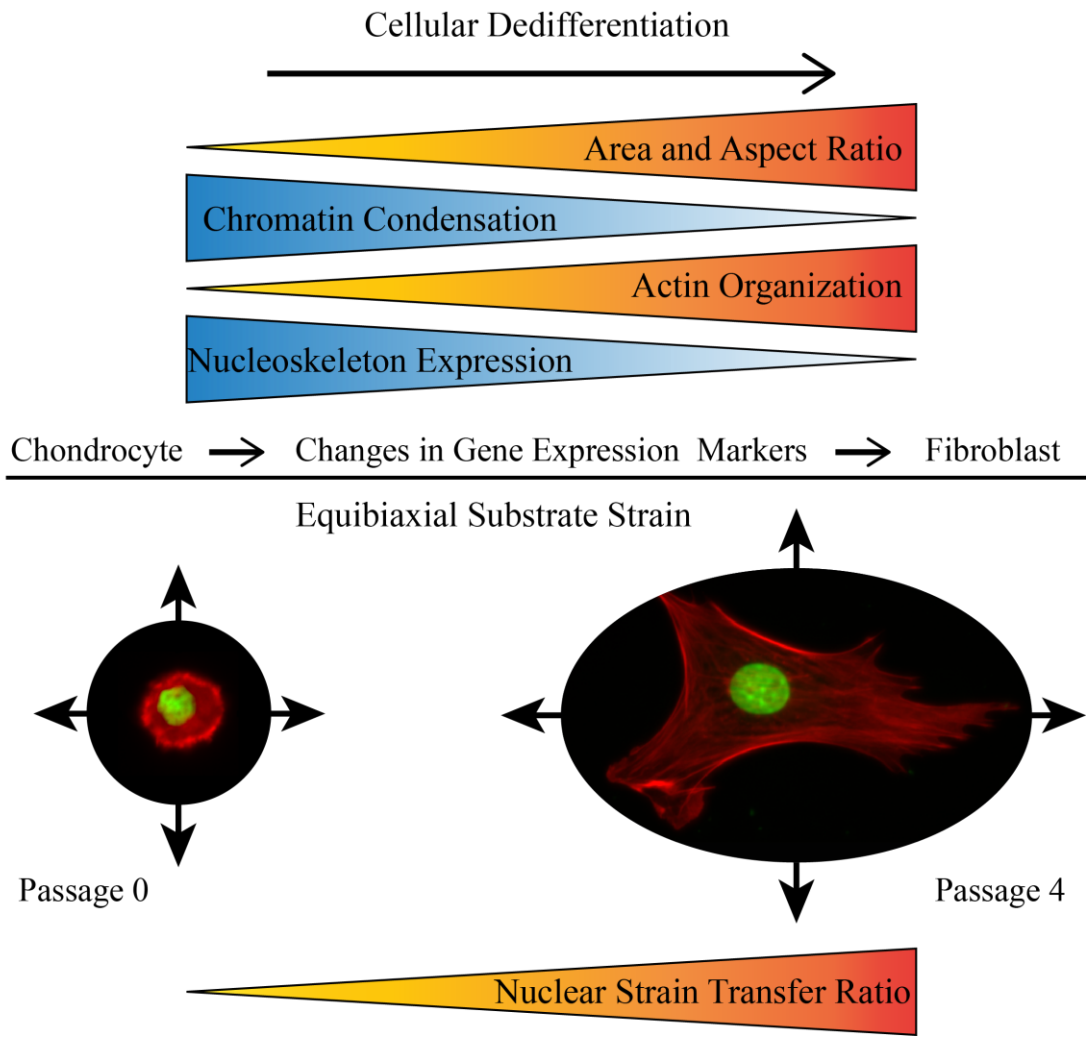

Figure 5.6. Changes in morphological and nucleoskeletal expressions for chondrocyte cells (P0) that dedifferentiates into a fibroblast phenotype (P4) will be helpful to the nuclear strain transfer ratio increase seen between P0 to P4 cell.

CHAPTER 6. CHANGES IN CELL-SUBSTRATE ADHESION AND INTRANUCLEAR STRAINS ARE CORRELATED DURING OSMOTIC LOADING OF CHONDROCYTE CELLS

6.1 Abstract

Cells can sense both chemical and mechanical changes in the local environment. For a mechanical stimulus, the cell and nucleus are deformed by direct mechanical linkages from the extracellular matrix to the nucleus. The cytoskeleton is thought to be the internal cytoplasmic structure of the cell that transmits the mechanical stimulus to the nucleus. In chemical osmotic challenges, the salt concentrations are altered and osmotic pressures drive water in or out of the nucleus and cell causing cytoskeletal independent deformation. Bulk nuclear deformations have been measured during osmotic challenges providing limited information about how non direct chemical stimulus can mechanically deform the nucleus. Iterative warping is a method that has been developed that measures intranuclear mechanics, providing greater detail about the nuclear mechanics during chemical and mechanical stimuli. Force traction microscopy is used to measure what it is mechanically happening during osmotic loading at the cell-substrate interface. In this study, intranuclear strain maps and cell-force adhesion fields will be measured simultaneously. Cell-substrate adhesion is negatively linearly correlated to the compressive intranuclear strain for the first ten minutes after a hyperosmotic challenge of passage four chondrocytes. These data suggest that cell mechanical interactions with the substrate and the ability for the cell to maintain its nuclear shape are related to the internal osmotic pressure of the cell and not just the cytoskeletal components.

6.2 Introduction

The cell interacts with its mechanical and chemical environment in many ways that regulate gene expression. The nucleus is mechanically connected through the

cytoskeleton to the extracellular matrix [89]. Mechanical signals translated to the nucleus that deform the euchromatin and heterochromatin regions are starting to be considered as mechano-regulators in gene expression[17,41]. In contrast to directly pulling on the cell and transducing signals through the cytoskeleton osmotic pressure can change the volume of the cell and nucleus through passive transport of water even when the cytoskeleton is disrupted[90,91]. Additionally osmotic loading of cells has shown to alter gene expression yet the mechanism of how this happens is still unknown[92,93]. It is hypothesized this happens because during hyperosmotic loading chromatin condensation occurs.

Cellular force traction microscopy can be used to understand the cell-substrate interface by measuring the cellular adhesion force. Force maps are calculated from the displacements of beads in a substrate that are imaged before and after the cell is chemically removed. Many chemical treatments have been studied, such as adding chemicals to activate or disrupt the cytoskeleton to see the changes in force traction maps[94]. The objective of this study is to explore the use of iterative warping to measure intranuclear strains while simultaneously measuring cell-substrate adhesion fields during osmotic loading. This study will provide time course information about the mechanical state of both the cell-substrate interface and the intranuclear regions of cells deforming to better understand how gene expression can be influenced by mechanical forces transmitted to the nucleus.

6.3 Methods

6.3.1 Fabrication of substrates

A Sylgard 184 silicone elastomer kit (Dow Corning) was used to prepare PDMS substrates of varying stiffness. The curing agent and silicone elastomer were measured by mass. Small 0.5µm red fluorescent beads were placed into the PDMS mixture. PDMS droplets of 40µL per substrate were allowed to set for 20 minutes to degas. The gels were then cured at 70°C overnight. After the completion of curing, the glass slides were lifted carefully off the petri dish and coated with fibronectin for cell attachment for 1 hour.

6.3.2 Two Photon microscopy imaging.

Primary bovine chondrocytes from the weight bearing region of the medical condyle were harvested from young cows less than 6 months old. Harvested cells were cultured and split around 80% confluence until passage 4. Prior to testing, cells were plated at a sparse density onto fibronectin coated substrates for 2 hours. For population responses to osmotic loading, cells were plated at low density, 5 to 9 cells per 106×106 µm imaging area, to minimize cell to cell interaction. For single cell bead displacement experiments cells were highly diluted for a very sparse plating so only one cell is in the imaging area to eliminate displacement of the substrate by multiple cells. The cells were stained with DNA Hoechst stain and incubated for 15 minutes.

Two photon imaging was performed using an Olympus Confocal Microscope stage adapted with a tunable Mai Tai pulse laser that exited at a wavelength of 740nm. The detectors wavelength ranges were set to 430-500 nm (set as green) and 540-600 nm (set as red) to image the nucleus and fluorescent beads, respectively. Also detected in in the green channel was the shape of the nucleus. This multiplexing of images on a single excitation wavelength was made possible because indigenous NADH is excited by two photon microscopy at wavelengths below 800nm peaking near 720 nm. The gel substrates with stained cells were placed over a 60× water emission objective with a rubber annulus placed on top to ensure liquid stayed on the gel. Two z stack images 1 minute apart were taken before treatment and 10 images, at the same time interval, after osmotic loading. Another image was taken of just the beads after the cells were removed from the substrate with the addition of TypLE™ Express (Life Technologies).

6.3.3 Osmotic Loading experiments

It is well established that hypertonic osmotic challenge causes a reduction in cellular and nucleus cross sectional area[18,95-97]. The substrates were removed from the staining culture media and the majority of the liquid was wicked off except for a thin film that wetted the surface. An area of interest with cells was found quickly before the liquid dehydrated and two z-stack images were taken. Immediately after the second image to change the osmolality from approximately 320 mOsm in the thin film culture medium to a 500

mOsm saline solution 500 μL was added by dropping it in to the well very gently. The control experiment included taking images of the cells with the thin layer of culture medium for 12 minutes, 1 minute apart. The addition of the 500 mOsm saline solution was repeated exactly the same way for the population response experiment and for bead-single cell deformation experiments.

6.3.4 Nuclear and substrate deformation measurements

All image processing was done using ImageJ and custom codes written in Matlab. The average Z projection of the nucleus z stack for each time point was taken to calculate the normalized cross sectional area and engineering strain of the major axis calculated as the percent change in major axis. For the cell population osmotic challenge study the control experiment measured 27 cells from 5 substrates and the osmotic loading results are of 32 cells from 4 substrates. Results are plotted as mean and standard error bars in figure 6.1.

For the single cell substrate and nucleus deformation, the first image and the images taken at 2, 4, 6, 8 and 10 minutes after osmotic loading were used to calculate intranuclear strain fields using iterative warping and substrate deformation. Substrate displacement field images were measured using an iterative PIV (Particle Image Velocimetry) ImageJ plugin. Two substrate displacement fields are measured from two different reference points. The first displacement field is the cell-substrate adhesion field, which is measured by taking the last image as the reference (cell removed) and subtracting each time point. The first time point is then considered the stable cell-substrate adhesion field (Figure 6.2). The displacement field arrows point inward, which represents the current adhesion state of the cell pulling in on the substrate. The first image was used as the other reference point to measure the change in the cell-substrate adhesion field. The displacement field is measured by subtracting the beads at each time point from the first. Three cells, with different morphologies (2, 3, and 4 apexes), were selected to determine how cell-substrate adhesion fields change with morphology and if intranuclear strains correlate. To look at the time dependence of intranuclear mechanics and substrate interactions a 3 apexes cell was selected and result were plotted versus time. To measure the local bead movements at each of the apexes, 3 bead's displacements were

averaged at each apex (I, II and III). Based off of the directions of the arrows in the displacement fields a magnitude displacement balance is achieved by adding the average displacements at I and II to equal that at III (Figure 6.3D).

6.4 Results

6.4.1 Bulk nuclear changes during osmotic loading

A 12 min time series images of nuclei was taken for an osmotic challenge from 320 to 500 mOsm and for control nuclei (no osmotic challenge) (Figure 6.1). In the control experiment a total of 27 nuclei from 5 different replica experiments were measured. The control cells had on average no change in the nucleus area (slope=0.000 R^2=0.3199) and a very slight decrease in the percent engineering strain of the major axis (slope=-0.08 R^2=0.8693). In the osmotic loading experiment a total of 32 nuclei from 4 different replicas were measured. The hyperosmotic loaded cells saw a significant decrease in the area (slope=-0.011 R^2=0.9761) and percent engineering strain (slope=0.46 R^2=0.9716).

6.4.2 Cell-substrate adhesion maps correlate to morphology

To measure the substrate deformation when cells are osmotically challenged, the cells were plated sparsely as to not confound the results. Three morphological shapes were selected to compare the substrate displacement fields. Cells with 2, 3, or 4 apexes were selected and osmotically loaded for 10 minutes. The different cell shapes showed the similar patterns in the stable cell-substrate adhesion field with localized deformation at the apexes of the cell Figure 2 A. The changes in cell-substrate adhesion fields are taken at 10 minutes after osmotic loading. It shows the same patterns of displacement but that the cell is still slightly attached after 10 minutes. If the cell was completely released the displacements in Figure 6.2 A, B would be exactly the same. The change in cell-substrate adhesion field displacements for the 2 and 3 apex cells are 2× that of the 4 apex cell. This trend follows with the nuclear hydrostatic strain fields in that the compressive strains in the nuclei for 2 and 3 are about twice as big as with the 4 apex cell. The nuclear strains fields are mostly compressive with a few really large compressive regions and a few zero or slightly tensile pockets Figure 6.2C.

6.4.3 Changing with time after Osmotic loading

In figure 6.3 time series data is presented that provides more detail about how cell-substrate adhesion and nuclear strain change as a function of time. In the time measurement plots hydrostatic and percent engineering strain of the major axis are plotted for 10 minutes after osmotic loading. The change in nuclear strain for both measurements is linear with respect to time and has similar percent strain rates to that of warping = -0.44 percent strain/min $R^2 = 0.9842$ and Engr. Strain = -0.47 percent strain/min, $R^2 = 0.9945$. The engineering strain underestimates the average hydrostatic strain for all time points. The slope is linear for the average displacement versus time plots for all three apex locations in the change in cell-substrate adhesion field, (slopes and R^2 values are in Table 6.1). Summing the displacements at apexes I and II equals III. This would indicate that the cell is maintaining a force balance during the osmotic challenge as it is releasing the substrate. The average bead displacement rate for all three locations is 62.8 nm/min. The bead displacement versus hydrostatic strain plot shows a linear correlation with a ratio of 128 nm per 1% nuclear strain ($R^2 = 0.9685$).

6.5 Discussion and Conclusion

The average population response to hyperosmotic loading was similar to other studies that look at the normalized cross section area change with time. However, in a previous study the normalized area plateaued with in the first 40 seconds[95]. The differences in that study is that chondrocyte passage zero cells, that have spherical cell morphologies were used compared to passage four chondrocytes with fibroblast phenotype morphologies that were used in this study. The nuclear response measured with warping was linear over the 10 minutes time frame (Figure 6.1). Whereas, passage zero cells, showed a nonlinear response for 140 seconds in a previous paper[95]. It is assumed then that if our studies had lasted longer we could have seen this similar nonlinear response and could have calculated a time constant for the osmotic response. What should be noted is that higher resolution images for our nuclear strain measurements and changes to the nucleus due to the osmotic treatment would be confounded by the longer imaging times.

The three cell-substrate adhesion fields for the different cell morphologies all show similar spatial trends of concentrated displacement at the cell apex. Local stress concentrations at the cell apexes are similar for other cell types and for cells on 2D and in 3D substrates[58,98]. Among all three cell cases, there was one apex that had a larger deformation than the others. The pattern of cell-substrate adhesion was maintained for 10 minutes after osmotic loading but with a decrease in magnitude. The intranuclear strain maps show that there are pockets of high and almost non-compressive strain. The high compressive areas in the nucleus are possible areas that had higher water content before hyperosmotic loading. This is rationalized by understanding that osmosis occurs with water leaving the nucleus and cell when the salt concentration is increased in the extracellular space (Figure 6.4). These areas would be considered as euchromatin regions where higher gene expression is occurring. With previous studies in the literature experiements have shown changes in gene expression profiles due to osmotic loading[91,93,99]. The nucleus compression as mapped by the warping strain fields could be used as a way to identify mechanical mechanism for altering gene expression.

Measuring intranuclear strain and change in cell-substrate adhesion over time allows for the correlation of how the cell can mediate both. As water is leaving the cytoplasm and nucleus, the cell deformation of the substrate decreases as the cell and nucleus area is decreased. The strain in the nucleus and the substrate deformation are both linear and the displacement vs. strain can be plotted. This plot is similar to a stress vs. strain plot in a mechanics of materials tensile test experiment. The slope of the stress vs. strain curve is proportional to the modulus of the material, which in our case would be the nucleus modulus. To convert the displacements to stress would be very difficult with stress being force of the cell divided by the area of the cell. This conversion is difficult because the area where the cell is pulling is not known. Also, if we did get the stress at the cell-substrate what portion of that stress is transferred to nucleus is still limited by not knowing the cell modulus.

This study's objective was focused on measuring intranuclear strain simultaneously with substrate deformation during hyperosmotic loading of cells. Construction of the force

traction fields was attempted but because of discontinuities in the displacement field, a large amount of noise was calculated (results not presented). Different smoothing algorithms and methods can be applied but currently were not incorporated in this work. However, the results presented as displacement maps provide an approximation of the directions, but not magnitude of the force traction maps. It will be beneficial to know the traction force field values for future work where strain transfer from the substrate to the nucleus could be modeled and the force values could be used as a boundary condition in determine nucleus material properties. Understanding the change in cellular forces and intranuclear mechanics will help elucidate how cells sense and regulate gene actives due to mechanical and chemical extracellular cues.

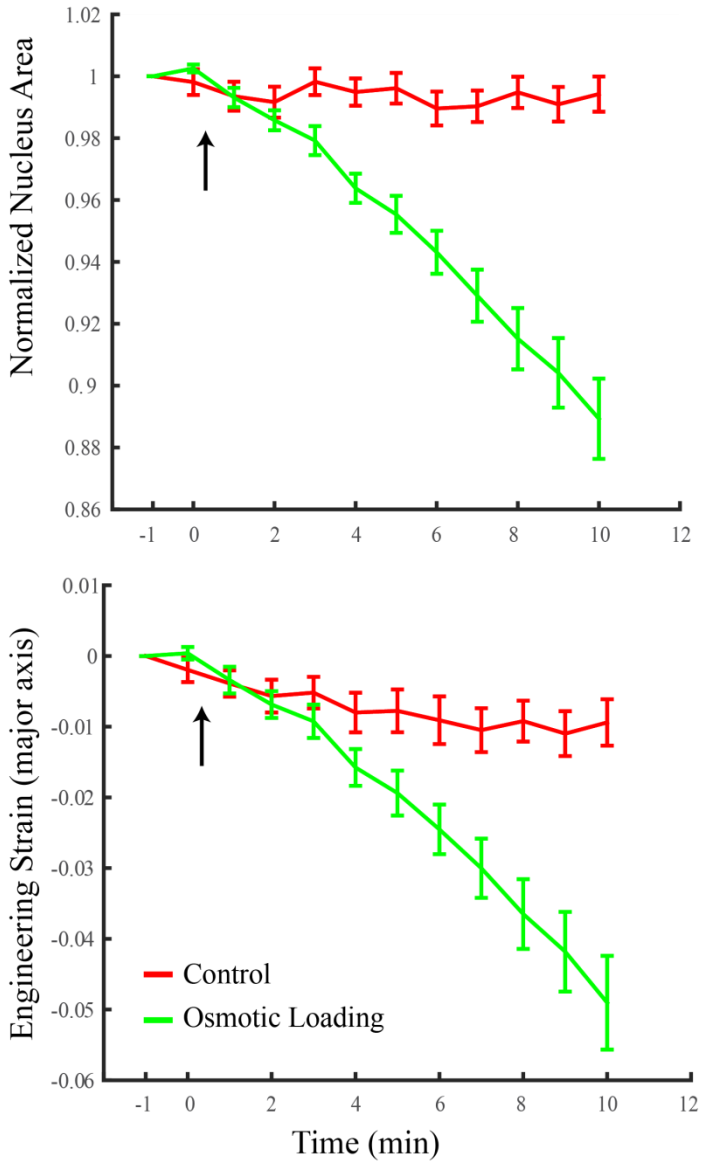

Figure 6.1. No significant change in the bulk measures of normalized area and engineering strain of the major axis for the control study. Area (slope=0.000 R^2=0.3199) and percent engineering strain (slope=-0.08 R^2=0.8693) for 27 cells from 5 substrates. There are liner compressive changes in the 320 to 500 mOsm loading for both normalized nucleus area and engineering strain with respect to time. With significant decrease in the area (slope=-0.011 R^2=0.9761) and percent engineering strain (slope=0.46 R^2=0.9716) for 32 cells from 4 substrates. Mean and standard error bars are plotted.

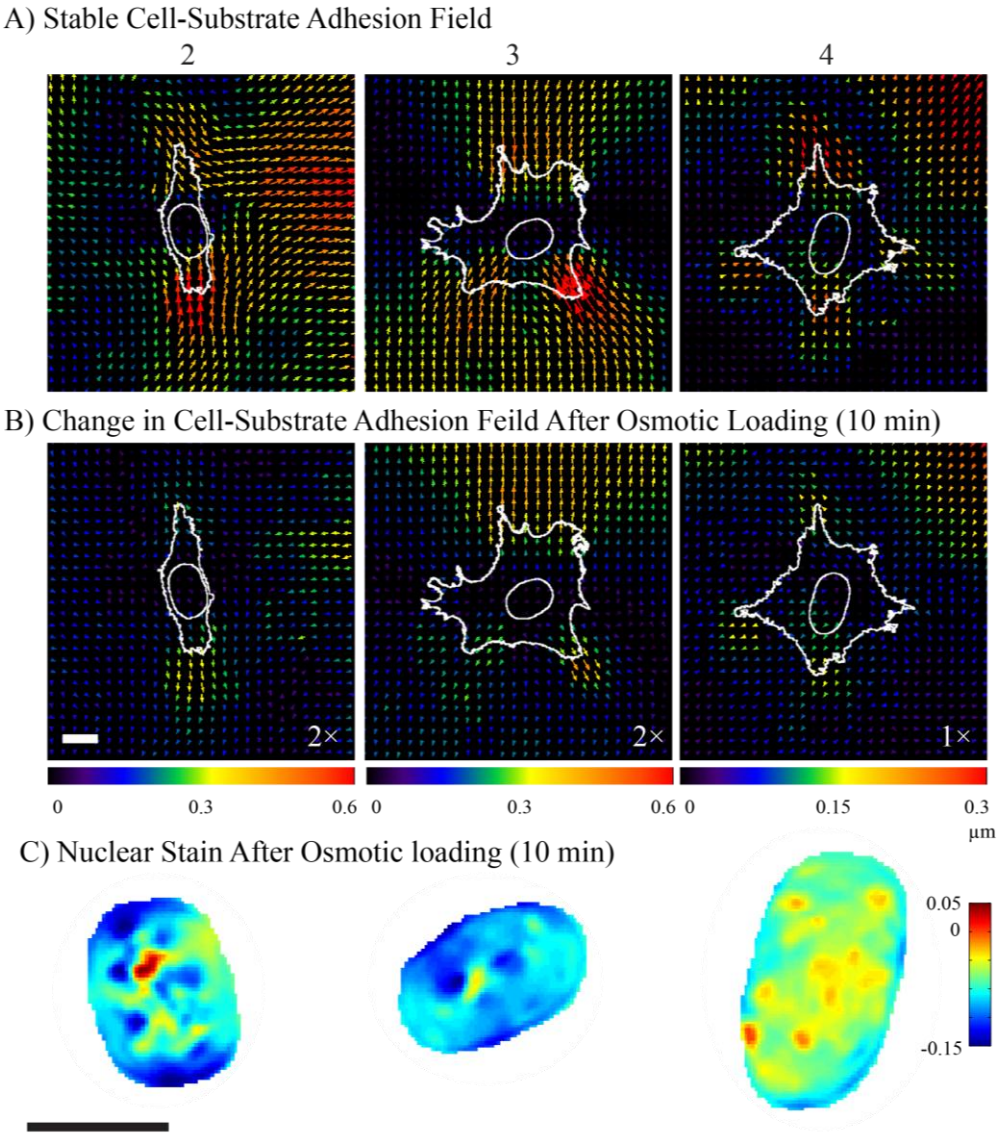

Figure 6.2. The shape of substrate deformation matches that of the shape of the nucleus from cells with 2, 3, and 4 apexes. The nuclear strain compressive magnitudes are similar to the general magnitude of substrate displacement between the three cells. With substrate 2 and 3 being on a scale 2× that of cell 4 and the compressive intranuclear strains are about have as much in 4 than they are in 2 and 3.

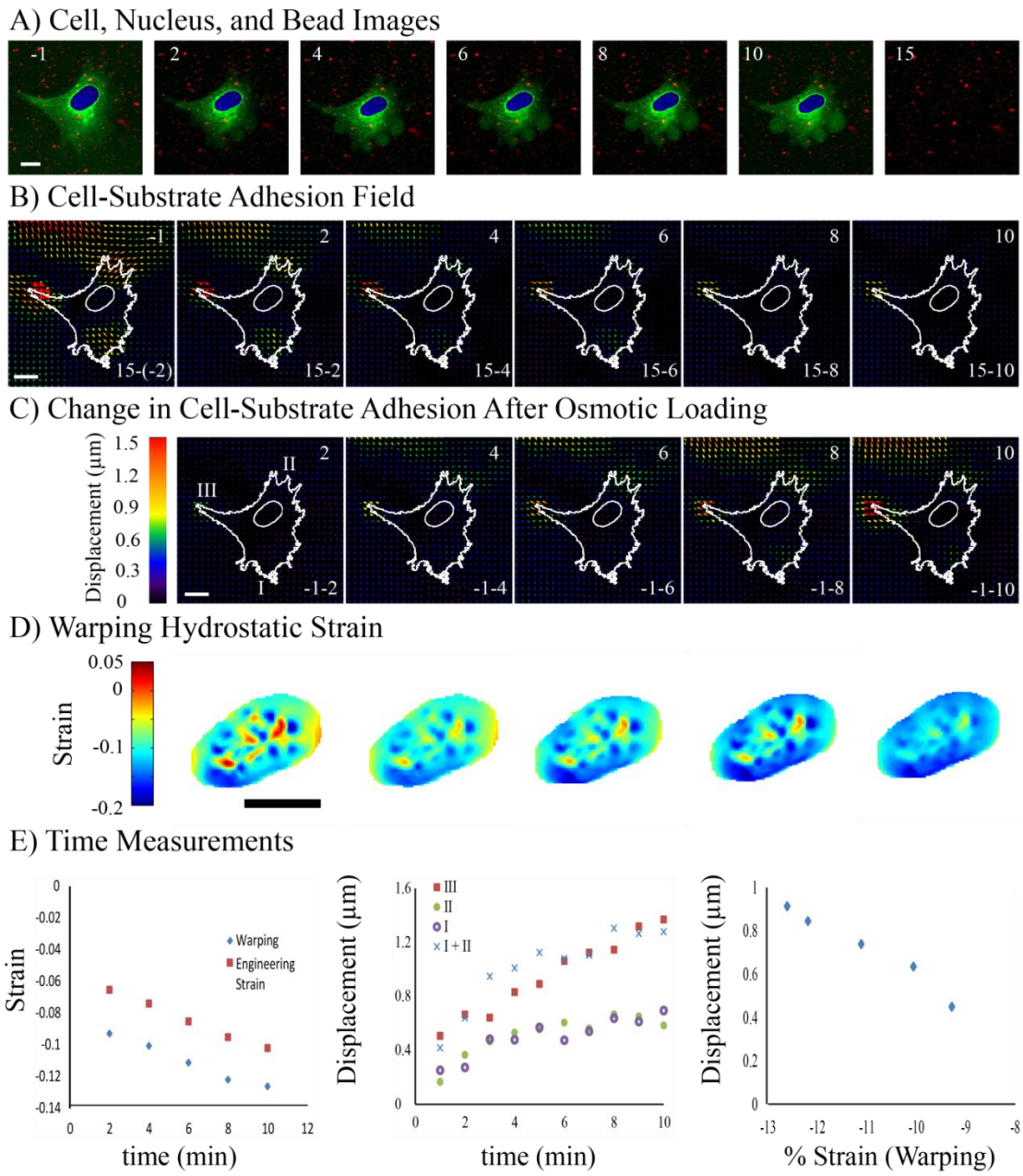

Figure 6.3. By tracking the deformation of the nucleus D) and substrate C) after osmotic loading the effects of water leaving the nucleus and cell can be seen as linear correlation between bead displacement and %strain of the nucleus E). There is a force balance between the three apexes (I, II, II marked in C) of the cell which can be seen in the adhesion maps or seen in plotting the displacement of the locations E).

Table 6.1: Linear regression slope and R^2 values for the strain and displacement plots in figure 3.

	% Strain Rate/min	R^2
Warping	-0.44	0.9842
Eng Strain	-0.47	0.9945

	Bead Displacement rate (nm/ min)	R^2
I	45.3	0.8324
II	43.3	0.7055
III	99.7	0.9796
I+II	88.7	0.8175
*Average(I,II,III)	62.8	0.9564

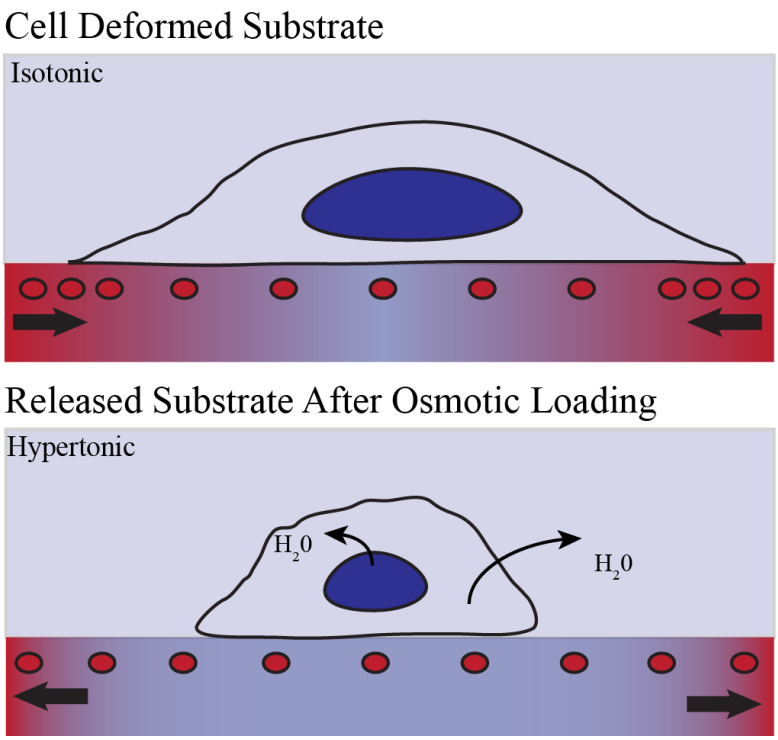

Figure 6.4. An illustration of the substrate release and compression of the cell and nucleus during osmotic loading when the extracellular fluid goes for isotonic to hypertonic. The mechanism of cellular and nuclear deformation is the loss of water through osmosis.

CHAPTER 7. INTRANUCLEAR MECHANICS: SIGNIFICANCE AND POTENTIAL

The three way intersection of mechanics, biochemistry and the nucleus is gaining more attention because of the understanding that the nucleus is a mechano-sensor. However, how it works and by what mechanisms is still unknown. In diseases like laminopathies where patients have cells with mechanically compromised nuclear lamins, the nucleus acting as a mechano-senor is compromised. Using iterative warping to further study nuclear mechanics in disease states will provide local chromatin level mechanics that may causes the altered cellular activity found in many diseases and cancers[11,88,100]. Chapter three of this dissertation was published in 2013 and in 2014 it already has two citations from other labs that work on nuclear lamin mechano-responsive properties[101] and cytoskeleton and nucleus biomechanical responses[102]. The findings that intranuclear mechanics are complex and mechanically dynamic were cited by the other researchers. Basic geometrical measurements simply underestimate the deformations that occur in many experimental settings.

In this dissertation, three completely different cell mechanics experiments were performed each having its own strengths and weaknesses. The cartilage tissue shear experiments' strength was that the cell was able to be in its native 3D matrix allowing for a close representation of what a cell will actually mechanically sense and what gene regulation might be like *in vivo*. The limitation of doing cell mechanics in tissues is that knowing the exact loading condition from one cell to the other can be confounded by its location in the microstructure of the tissue. With the applied distant force is transferred differently throughout the structure. The strength of the cell stretching experiment is that the applied mechanical stimulus is directly applied to the cell and the confounding factors of the matrix are eliminated. However, the weakness is that cell's phenotypes change while in cell culture and the biological relevance is lost when the cell population is not in

its native microenvironment. It was seen that the P4 chondrocytes were more like fibroblast and had different strain transfer ratios compared to P0 chondrocytes. The novelty of the cell-substrate adhesion and intranuclear strains measured during osmotic stress is that mechanical deformation measured did not have to come from a mechanical stimulus. A limitation is that by not controlling the cell shape, every experiment is different, because the cell gripping force changes based on cell shape.

Potential future studies that would provide a mechanistic insight into how strain is transferred to the nucleus would be to control some parameters that are controlled in typical material testing experiments. One parameter would be the cross sectional area to be the same in the loading experiments. This could be accomplished by micro-patterning the substrates in both the substrate stretching experiment and osmotic force traction experiment. It would be the equivalence of always having the same grips and specimen size in a tensile test. A second parameter where error can be reduced would be in sensing the force that the cell is applying during experimental treatments. Stretchable substrates with tracking beads have non-uniform stiffness and surface roughness and the location where the cell is anchored is nonspecific compared to cells on micro post. The full potential of measuring intranuclear mechanics will be realized when real time individual genes and gene expression can be imaged. Then the loop of intranuclear mechanics and gene expression a can be completed and how the nucleus is a mechanosensor will become useful in disease treatment and cell tissue engineering.

REFERENCES

REFERENCES

1 Henderson, J. T. & Neu, C. P. in *Handbook of Imaging in Biological Mechanics* (eds Corey P Neu & Guy M Genin) Ch. 33, 451 (2014).

2 Henderson, J. T., Shannon, G., Veress, A. I. & Neu, C. P. Direct Measurement of Intranuclear Strain Distributions and RNA Synthesis in Single Cells Embedded within Native Tissue. *Biophysical Journal* **105**, 2252-2261, doi:10.1016/j.bpj.2013.09.054 (2013).

3 Guilak, F. VOLUME AND SURFACE-AREA MEASUREMENT OF VIABLE CHONDROCYTES IN-SITU USING GEOMETRIC MODELING OF SERIAL CONFOCAL SECTIONS. *Journal of Microscopy-Oxford* **173**, 245-256 (1994).

4 Guilak, F., Jones, W. R., Ting-Beall, H. P. & Lee, G. M. The deformation behavior and mechanical properties of chondrocytes in articular cartilage. *Osteoarthritis and Cartilage* **7**, 59-70 (1999).

5 Wang, N., Tytell, J. D. & Ingber, D. E. Mechanotransduction at a distance: mechanically coupling the extracellular matrix with the nucleus. *Nature Reviews Molecular Cell Biology* **10**, doi:10.1038/nrm2594 (2009).

6 Engler, A. J., Sen, S., Sweeney, H. L. & Discher, D. E. Matrix elasticity directs stem cell lineage specification. *Cell* **126**, 677-689, doi:10.1016/j.cell.2006.06.044 (2006).

7 Veress, A. I., Weiss, J. A., Gullberg, G. T., Vince, D. G. & Rabbitt, R. D. Strain measurement in coronary arteries using intravascular ultrasound and deformable images. *Journal of Biomechanical Engineering-Transactions of the Asme* **124**, doi:10.1115/1.1519279 (2002).

8 Veress, A. I., Gullberg, G. T. & Weiss, J. A. Measurement of strain in the left ventricle during diastole with cine-MRI and deformable image registration. *Journal of Biomechanical Engineering-Transactions of the Asme* **127**, 1195-1207, doi:10.1115/1.2073677 (2005).

9 Goldman, R. D., Gruenbaum, Y., Moir, R. D., Shumaker, D. K. & Spann, T. P. Nuclear lamins: building blocks of nuclear architecture. *Genes & Development* **16**, 533-547, doi:10.1101/gad.960502 (2002).

10 Gerace, L. & Huber, M. D. Nuclear lamina at the crossroads of the cytoplasm and nucleus. *Journal of Structural Biology* **177**, 24-31, doi:10.1016/j.jsb.2011.11.007 (2012).

11 Li, Q. S. & Lim, C. T. Structure-Mechanical Property Changes in Nucleus arising from Breast Cancer. *Cellular and Biomolecular Mechancis and Mechanobiology* **4**, 465-475, doi:10.1007/8415_2010_19 (2011).

12 Alexopoulos, L. G., Erickson, G. R. & Guilak, F. A method for quantifying cell size from differential interference contrast images: validation and application to osmotically stressed chondrocytes. *Journal of Microscopy-Oxford* **205**, 125-135 (2002).

13 Aigner, T., Kurz, B., Fukui, N. & Sandell, L. Roles of chondrocytes in the pathogenesis of osteoarthritis. *Current Opinion in Rheumatology* **14**, 578-584, doi:10.1097/01.bor.0000022355.07263.81 (2002).

14 Hou, H. W. *et al.* Deformability study of breast cancer cells using microfluidics. *Biomedical Microdevices* **11**, 557-564, doi:10.1007/s10544-008-9262-8 (2009).

15 Chalut, K. J. *et al.* Chromatin decondensation and nuclear softening accompany Nanog downregulation in embryonic stem cells. *Biophysical Journal* **103**, 2060-2070, doi:10.1016/j.bpj.2012.10.015 (2012).

16 Chuang, C. H. & Belmont, A. S. Moving chromatin within the interphase nucleus-controlled transitions? *Seminars in Cell & Developmental Biology* **18**, 698-706, doi:10.1016/j.semcdb.2007.08.012 (2007).

17 Trinkle-Mulcahy, L. & Lamond, A. I. Nuclear functions in space and time: Gene expression in a dynamic, constrained environment. *Febs Letters* **582**, 1960-1970, doi:10.1016/j.febslet.2008.04.029 (2008).

18 Martins, R. P., Finan, J. D., Guilak, F. & Lee, D. A. Mechanical Regulation of Nuclear Structure and Function. *Annual Review of Biomedical Engineering, Vol 14* **14**, 431-455, doi:10.1146/annurev-bioeng-071910-124638 (2012).

19 Teperino, R., Lempradl, A. & Pospisilik, J. A. Bridging epigenomics and complex disease: the basics. *Cellular and Molecular Life Sciences* **70**, 1609-1621, doi:10.1007/s00018-013-1299-z (2013).

20 Neu, C. P., Khalafi, A., Komvopoulos, K., Schmid, T. & Reddi, A. H. Mechanotransduction of articular cartilage superficial zone protein by TGF-b signaling. *Arthritis Rheum* **56**, 3706-3714 (2007).

21 Neu, C. P., Komvopoulos, K., Reddi, A. H., Schmid, T. & Di Cesare, P. A. Friction coefficient and superficial zone protein are increaseed in patients with advanced osteoarthritis. *Arthritis Rheum*, in press (2010).

22 Latchman, D. S. Transcription factors: An overview. *International Journal of Biochemistry & Cell Biology* **29**, 1305-1312, doi:10.1016/s1357-2725(97)00085-x (1997).

23 Gorlich, D. & Kutay, U. Transport between the cell nucleus and the cytoplasm. *Annual Review of Cell and Developmental Biology* **15**, 607-660, doi:10.1146/annurev.cellbio.15.1.607 (1999).

24 Raska, I., Shaw, P. J. & Cmarko, D. New insights into nucleolar architecture and activity. *International Review of Cytology - a Survey of Cell Biology, Vol 255* **255**, 177-+, doi:10.1016/s0074-7696(06)55004-1 (2006).

25 Cremer, T. *et al.* Chromosome territories, interchromatin domain compartment, and nuclear matrix: An integrated view of the functional nuclear architecture. *Critical Reviews in Eukaryotic Gene Expression* **10**, 179-212 (2000).

26 Mammoto, A., Mammoto, T. & Ingber, D. E. Mechanosensitive mechanisms in transcriptional regulation. *Journal of Cell Science* **125**, doi:10.1242/jcs.093005 (2012).

27 Lim, K. Y., Henderson, J. T. & Neu, C. P. Cell and tissue deformation measurements: Texture correlation with third-order approximation of displacement gradients. *Journal of Biomechanics* **46**, 2490-2496, doi:10.1016/j.jbiomech.2013.07.035 (2013).

28 Guilak, F. Compression-induced changes in the shape and volume of the chondrocyte nucleus. *Journal of Biomechanics* **28**, 1529-& (1995).

29 Henderson, J. T., Shannon, G., Veress, A. & Neu, C. P. Direct Measurement of Intranuclear Strain Distributions and RNA Synthesis in Single Cells Embedded within Native Tissue. *Biophysical Journal*, in press (2013).

30 Campbell, J. J., Blain, E. J., Chowdhury, T. T. & Knight, M. M. Loading alters actin dynamics and up-regulates cofilin gene expression in chondrocytes. *Biochemical and Biophysical Research Communications* **361**, 329-334, doi:10.1016/j.bbrc.2007.06.185 (2007).

31 Chan, P. S. *et al.* Gene expression profile of mechanically impacted bovine articular cartilage explants. *Journal of Orthopaedic Research* **23**, 1146-1151, doi:10.1016/j.orthres.2005.01.016 (2005).

32 Dehne, T. *et al.* Gene expression profiling of primary human articular chondrocytes in high-density micromasses reveals patterns of recovery, maintenance, re- and dedifferentiation. *Gene* **462**, 8-17, doi:10.1016/j.gene.2010.04.006 (2010).

33 Mousoulis, C., Xu, X., Reiter, D. A. & Neu, C. P. Single cell spectroscopy: Noninvasive measures of small-scale structure and function. *Methods*, doi:10.1016/j.ymeth.2013.07.025 (2013).

34 Buckley, M. R., Bergou, A. J., Fouchard, J., Bonassar, L. J. & Cohen, I. High-resolution spatial mapping of shear properties in cartilage. *Journal of Biomechanics* **43**, 796-800, doi:10.1016/j.jbiomech.2009.10.012 (2010).

35 Choi, J. B. *et al.* Zonal changes in the three-dimensional morphology of the chondron under compression: The relationship among cellular, pericellular, and extracellular deformation in articular cartilage. *Journal of Biomechanics* **40**, 2596-2603 (2007).

36 Jao, C. Y. & Salic, A. Exploring RNA transcription and turnover in vivo by using click chemistry. *Proceedings of the National Academy of Sciences of the United States of America* **105**, doi:10.1073/pnas.0808480105 (2008).

37 Paredes, E. & Das, S. R. Click Chemistry for Rapid Labeling and Ligation of RNA. *Chembiochem* **12**, doi:10.1002/cbic.201000466 (2011).

38 Politz, J. C., Tuft, R. A., Pederson, T. & Singer, R. H. Movement of nuclear poly(A) RNA throughout the interchromatin space in living cells. *Current Biology* **9**, 285-291, doi:10.1016/s0960-9822(99)80136-5 (1999).

39 Banerjee, B., Bhattacharya, D. & Shivashankar, G. V. Chromatin structure exhibits spatio-temporal heterogeneity within the cell nucleus. *Biophysical Journal* **91**, 2297-2303, doi:10.1529/biophysj.105.079525 (2006).

40 Bhattacharya, D., Talwar, S., Mazumder, A. & Shivashankar, G. V. Spatio-Temporal Plasticity in Chromatin Organization in Mouse Cell Differentiation and during Drosophila Embryogenesis. *Biophysical Journal* **96**, 3832-3839, doi:10.1016/j.bpj.2008.11.075 (2009).

41 Shivashankar, G. V. Spatio-temporal organization of chromatin assembly and transcription control within living cells. *Biophysical Journal*, 14A-14A (2007).

42 Haudenschild, D. R. *et al.* Vimentin Contributes to Changes in Chondrocyte Stiffness in Osteoarthritis. *Journal of Orthopaedic Research* **29**, 20-25, doi:10.1002/jor.21198 (2011).

43 Knight, M. M. *et al.* Cell and nucleus deformation in compressed chondrocyte-alginate constructs: temporal changes and calculation of cell modulus. *Biochim. Biophys. Acta-Gen. Subj.* **1570**, 1-8 (2002).

44 Guilak, F., Ratcliffe, A. & Mow, V. C. CHONDROCYTE DEFORMATION AND LOCAL TISSUE STRAIN IN ARTICULAR-CARTILAGE - A CONFOCAL MICROSCOPY STUDY. *Journal of Orthopaedic Research* **13**, 410-421 (1995).

45 Abusara, Z., Seerattan, R., Leumann, A., Thompson, R. & Herzog, W. A novel method for determining articular cartilage chondrocyte mechanics in vivo. *Journal of Biomechanics* **44**, 930-934, doi:10.1016/j.jbiomech.2010.11.031 (2011).

46 Guilak, F., Alexopoulos, L. G., Haider, M. A., Ting-Beall, H. P. & Setton, L. A. Zonal uniformity in mechanical properties of the chondrocyte pericellular matrix: Micropipette aspiration of canine chondrons isolated by cartilage homogenization. *Annals of Biomedical Engineering* **33**, 1312-1318, doi:10.1007/s10439-005-4479-7 (2005).

47 Bader, D. L., Ohashi, T., Knight, M. M., Lee, D. A. & Sato, M. Deformation properties of articular chondrocytes: A critique of three separate techniques. *Biorheology* **39**, 69-78 (2002).

48 Darling, E. M. Force scanning: a rapid, high-resolution approach for spatial mechanical property mapping. *Nanotechnology* **22** (2011).

49 Wilusz, R. E. et al. THE INHOMOGENEOUS MECHANICAL PROPERTIES OF THE PERICELLULAR MATRIX OF ARTICULAR CARTILAGE MEASURED IN SITU BY ATOMIC FORCE MICROSCOPY. (2009).

50 Gilchrist, C. L., Witvoet-Braam, S. W., Guilak, F. & Setton, L. A. Measurement of intracellular strain on deformable substrates with texture correlation. *Journal of Biomechanics* **40**, 786-794, doi:10.1016/j.jbiomech.2006.03.013 (2007).

51 Misteli, T. Nuclear structure - Protein dynamics: Implications for nuclear architecture and gene expression. *Science* **291**, doi:10.1126/science.291.5505.843 (2001).

52 Cremer, T. *et al.* Chromosome territories--a functional nuclear landscape. *Current Opinion in Cell Biology* **18**, 307-316, doi:10.1016/j.ceb.2006.04.007 (2006).

53 Felsenfeld, G. Chromatin unfolds. *Cell* **86**, 13-19 (1996).

54 Polach, K. J. & Widom, J. A model for the cooperative binding of eukaryotic regulatory proteins to nucleosomal target sites. *J Mol Biol* **258**, 800-812, doi:10.1006/jmbi.1996.0288 (1996).

55 Cairns, B. R. Chromatin remodeling: insights and intrigue from single-molecule studies. *Nat Struct Mol Biol* **14**, 989-996, doi:10.1038/nsmb1333 (2007).

56 Wang, N., Butler, J. P. & Ingber, D. E. Mechanotransduction across the cell surface and through the cytoskeleton. *Science* **260**, doi:10.1126/science.7684161 (1993).

57 Cardoso, M. C., Schneider, K., Martin, R. M. & Leonhardt, H. Structure, function and dynamics of nuclear subcompartments. *Current Opinion in Cell Biology* **24**, doi:10.1016/j.ceb.2011.12.009 (2012).

58 Legant, W. R. *et al.* Measurement of mechanical tractions exerted by cells in three-dimensional matrices. *Nature Methods* **7**, doi:10.1038/nmeth.1531 (2010).

59 Iyer, K. V., Pulford, S., Mogilner, A. & Shivashankar, G. V. Mechanical Activation of Cells Induces Chromatin Remodeling Preceding MKL Nuclear Transport. *Biophysical Journal* **103**, doi:10.1016/j.bpj.2012.08.041 (2012).

60 Ouyang, M., Sun, J., Chien, S. & Wang, Y. Determination of hierarchical relationship of Src and Rac at subcellular locations with FRET biosensors. *Proceedings of the National Academy of Sciences of the United States of America* **105**, doi:10.1073/pnas.0807537105 (2008).

61 Chan, D. D. & Neu, C. P. Transient and Microscale Deformations and Strains Measured under Exogenous Loading by Noninvasive Magnetic Resonance. *Plos One* **7**, doi:10.1371/journal.pone.0033463 (2012).

62 Neu, C. P., Reddi, A. H., Komvopoulos, K., Schmid, T. M. & Di Cesare, P. E. Increased friction coefficient and superficial zone protein expression in patients with advanced osteoarthritis. *Arthritis and Rheumatism* **62**, 2680-2687, doi:10.1002/art.27577 (2010).

63 Phatak, N. S. *et al.* Noninvasive determination of ligament strain with deformable image registration. *Annals of Biomedical Engineering* **35**, doi:10.1007/s10439-007-9287-9 (2007).

64 Veress, A., Phatak, N. & Weiss, J. in Handbook of Biomedical Image Analysis Volume III: Registration Models Vol. III Topics in Biomedical Engineering. International Book Series (eds Jasjit Suri, David Willson, & Swamy Laxminarayan) Ch. 12, 487-533 (Kluwer Acedemic / Plenum Publishers, 2005).

65 Veress, A. I. *et al.* Measuring regional changes in the diastolic deformation of the left ventricle of SHR rats using microPET technology and hyperelastic warping. *Annals of Biomedical Engineering* **36**, doi:10.1007/s10439-008-9497-9 (2008).

66 Gilchrist, C. L., Witvoet-Braam, S. W., Guilak, F. & Setton, L. A. Measurement of intracellular strain on deformable substrates with texture correlation. *Journal of Biomechanics* **40**, 786-794, doi:10.1016/j.jbiomech.2006.03.013 (2007).

67 Kruithof, M. *et al.* Single-molecule force spectroscopy reveals a highly compliant helical folding for the 30-nm chromatin fiber. *Nat Struct Mol Biol* **16**, 534-540, doi:10.1038/nsmb.1590 (2009).

68 Kim, E., Guilak, F. & Haider, M. A. The dynamic mechanical environment of the chondrocyte: a biphasic finite element model of cell-matrix interactions under cyclic compressive loading. *J Biomech Eng* **130**, 061009, doi:10.1115/1.2978991 (2008).

69 Neu, C. P., Hull, M. L. & Walton, J. H. Heterogeneous three-dimensional strain fields during unconfined cyclic compression in bovine articular cartilage explants. *J Orthop Res* **23**, 1390-1398 (2005).

70 Le Beyec, J. *et al.* Cell shape regulates global histone acetylation in human mammary epithelial cells. *Experimental Cell Research* **313**, 3066-3075, doi:10.1016/j.yexcr.2007.04.022 (2007).

71 Booth-Gauthier, E. A., Alcoser, T. A., Yang, G. & Dahl, K. N. Force-Induced Changes in Subnuclear Movement and Rheology. *Biophysical Journal* **103**, 2423-2431, doi:10.1016/j.bpj.2012.10.039 (2012).

72 Gilchrist, C. L., Xia, J. Q., Setton, L. A. & Hsu, E. W. High-resolution determination of soft tissue deformations using MRI and first-order texture correlation. *Ieee Transactions on Medical Imaging* **23**, 546-553, doi:10.1109/tmi.2004.825616 (2004).

73 Lim, K. Y., Henderson, J. T. & Neu, C. P. Cell and tissue deformation measurements: Texture correlation with third-order approximation of displacement gradients. *Journal of Biomechanics* **46**, 2490-2496, doi:10.1016/j.jbiomech.2013.07.035 (2013).

74 Veress, A. I., Weiss, J. A., Klein, G. J. & Gullberg, G. T. in *Computers in Cardiology 2002, Vol 29* Vol. 29 *Computers in Cardiology* (ed A. Murray) 709-712 (2002).

75 Mazumder, A. & Shivashankar, G. V. Gold-nanoparticle-assisted laser perturbation of chromatin assembly reveals unusual aspects of nuclear architecture within living cells. *Biophysical Journal* **93**, 2209-2216, doi:10.1529/biophysj.106.102202 (2007).

76 Dahl, K. N., Kahn, S. M., Wilson, K. L. & Discher, D. E. The nuclear envelope lamina network has elasticity and a compressibility limit suggestive of a molecular shock absorber. *Journal of Cell Science* **117**, 4779-4786 (2004).

77 Lammerding, J., Dahl, K. N., Discher, D. E. & Kamm, R. D. in *Cell Mechanics* Vol. 83 *Methods in Cell Biology* 269-294 (2007).

78 Dahl, K. N., Ribeiro, A. J. S. & Lammerding, J. Nuclear shape, mechanics, and mechanotransduction. *Circulation Research* **102**, 1307-1318, doi:10.1161/circresaha.108.173989 (2008).

79 Rowat, A. C., Lammerding, J., Herrmann, H. & Aebi, U. Towards an integrated understanding of the structure and mechanics of the cell nucleus. *Bioessays* **30**, 226-236, doi:10.1002/bies.20720 (2008).

80 Korhonen, R. K. & Herzog, W. Depth-dependent analysis of the role of collagen fibrils, fixed charges and fluid in the pericellular matrix of articular cartilage on chondrocyte mechanics. *Journal of Biomechanics* **41**, 480-485, doi:10.1016/j.jbiomech.2007.09.002 (2008).

81 Mukherjee, N. & Wayne, J. S. Load sharing between solid and fluid phases in articular cartilage: I - Experimental determination of in situ mechanical conditions in a porcine knee. *Journal of Biomechanical Engineering-Transactions of the Asme* **120**, 614-619 (1998).

82 Ofek, G., Natoli, R. M. & Athanasiou, K. A. In situ mechanical properties of the chondrocyte cytoplasm and nucleus. *Journal of Biomechanics* **42**, 873-877, doi:10.1016/j.jbiomech.2009.01.024 (2009).

83 Tung, S.-H. & Shih, M.-H. Precision verification of a simplified three-dimensional DIC method. *Optics and Lasers in Engineering* **49**, 937-945, doi:10.1016/j.optlaseng.2011.02.006 (2011).

84 Schulze-Tanzil, G. Activation and dedifferentiation of chondrocytes: Implications in cartilage injury and repair. *Annals of Anatomy-Anatomischer Anzeiger* **191**, 325-338, doi:10.1016/j.aanat.2009.05.003 (2009).

85 Rutledge, R. G. & Stewart, D. A kinetic-based sigmoidal model for the polymerase chain reaction and its application to high-capacity absolute quantitative real-time PCR. *Bmc Biotechnology* **8**, 28, doi:10.1186/1472-6750-8-47 (2008).

86 Versaevel, M., Grevesse, T. & Gabriele, S. Spatial coordination between cell and nuclear shape within micropatterned endothelial cells. *Nature Communications* **3**, doi:10.1038/ncomms1668 (2012).

87 Broers, J. L. V. *et al.* Decreased mechanical stiffness in LMNA-/- cells is caused by defective nucleo-cytoskeletal integrity: implications for the development of laminopathies. *Human Molecular Genetics* **13**, 2567-2580, doi:10.1093/hmg/ddh295 (2004).

88 Broers, J. L. V., Hutchison, C. J. & Ramaekers, F. C. S. Laminopathies. *Journal of Pathology* **204**, 478-488, doi:10.1002/path.1655 (2004).

89 Wang, N., Tytell, J. D. & Ingber, D. E. Mechanotransduction at a distance: mechanically coupling the extracellular matrix with the nucleus. *Nature Reviews Molecular Cell Biology* **10**, 75-82, doi:10.1038/nrm2594 (2009).

90 Oswald, E. S. et al. The role of microtubule organization in chondrocyte response to osmotic loading. (2007).

91 Irianto, J. *et al.* Osmotic Challenge Drives Rapid and Reversible Chromatin Condensation in Chondrocytes. *Biophysical Journal* **104**, 759-769, doi:10.1016/j.bpj.2013.01.006 (2013).

92 Tew, S. R. *et al.* Hyperosmolarity regulates SOX9 mRNA posttranscriptionally in human articular chondrocytes. *American Journal of Physiology-Cell Physiology* **297**, C898-C906, doi:10.1152/ajpcell.00571.2008 (2009).

93 Peffers, M. J., Milner, P. I., Tew, S. R. & Clegg, P. D. Regulation of SOX9 in normal and osteoarthritic equine articular chondrocytes by hyperosmotic loading. *Osteoarthritis and Cartilage* **18**, 1502-1508, doi:10.1016/j.joca.2010.08.011 (2010).

94 Kraning-Rush, C. M., Carey, S. P., Califano, J. P., Smith, B. N. & Reinhart-King, C. A. The role of the cytoskeleton in cellular force generation in 2D and 3D environments. *Physical Biology* **8**, doi:10.1088/1478-3975/8/1/015009 (2011).

95 Finan, J. D., Chalut, K. J., Wax, A. & Guilak, F. Nonlinear Osmotic Properties of the Cell Nucleus. *Annals of Biomedical Engineering* **37**, 477-491, doi:10.1007/s10439-008-9618-5 (2009).

96 Finan, J. D. & Guilak, F. The Effects of Osmotic Stress on the Structure and Function of the Cell Nucleus. *Journal of Cellular Biochemistry* **109**, 460-467, doi:10.1002/jcb.22437 (2010).

97 Oswald, E. S. *et al.* Effects of Hypertonic (NaCl) Two-Dimensional and Three-Dimensional Culture Conditions on the Properties of Cartilage Tissue Engineered from an Expanded Mature Bovine Chondrocyte Source. *Tissue Engineering Part C-Methods* **17**, 1041-1049, doi:10.1089/ten.tec.2011.0212 (2011).

98 Legant, W. R. *et al.* Multidimensional traction force microscopy reveals out-of-plane rotational moments about focal adhesions. *Proceedings of the National Academy of Sciences of the United States of America* **110**, 881-886, doi:10.1073/pnas.1207997110 (2013).

99 Chao, P. H. G., West, A. C. & Hung, C. T. Chondrocyte intracellular calcium, cytoskeletal organization, and gene expression responses to dynamic osmotic loading. *American Journal of Physiology-Cell Physiology* **291**, C718-C725, doi:10.1152/ajpcell.00127.2005 (2006).

100 Jaalouk, D. E. & Lammerding, J. Mechanotransduction gone awry. *Nature Reviews Molecular Cell Biology* **10**, 63-73, doi:10.1038/nrm2597 (2009).

101 Swift, J. & Discher, D. E. The nuclear lamina is mechano-responsive to ECM elasticity in mature tissue. *Journal of Cell Science* **127**, 3005-3015, doi:10.1242/jcs.149203 (2014).

102 Reynolds, N. H. *et al.* On the role of the actin cytoskeleton and nucleus in the biomechanical response of spread cells. *Biomaterials* **35**, 4015-4025, doi:10.1016/j.biomaterials.2014.01.056 (2014).

VITA

VITA

Jonathan Tyrus Henderson

Weldon School of Biomedical Engineering, Purdue University

Jonathan Henderson was born and raised in Boise, Idaho, where he attended Owyhee Elementary, South Junior High, and Borah High School. He hated biology because it was just memorizing a ton of hard to pronounce words and loved math and physics because they were easy and conceptual. He then majored in mechanical engineering at Boise State University where he had a change of heart. He found that the intersection of mechanics and biology is complicatedly amazing and there were really hard problems that fascinated his problem solving curiosity. Upon realizing he knew very little about biology and wanted to purse biomedical research as a career he enrolled at Purdue University. Where he is now writing his dissertation towards a Ph.D. in biomedical engineering while juggling being a husband and father of three kids, the youngest only a month old. His future plans are to enter industry in a research and development position for a biomedical company and solve those complex problems that drove him to graduate school to learn about the intersection of mechanics and biology. His future, future, plans are to retire and run a farmers market stand on the side of the road.

PUBLICATIONS

PUBLICATIONS

Publications based on work performed at Purdue University, listed in order of acceptance for publication:

KY Lim, JT Henderson, CP Neu. 2013. Cell and tissue deformation measurements: Texture correlation with third-order approximation of displacement gradients. Journal of biomechanics 46 (14), 2490-2496

JT Henderson, G Shannon, AI Veress, CP Neu, 2013. Direct Measurement of Intranuclear Strain Distributions and RNA Synthesis in Single Cells Embedded within Native Tissue. Biophysical Journal 105 (10), 2252-2261

JT Henderson, CP Neu. 2014. Intranuclear Measurement of Deformation in Single Cells. Handbook of Imaging in Biological Mechanics, CRC Press, 415-422

Journal of Biomechanics 46 (2013) 2490–2496

Contents lists available at ScienceDirect

Journal of Biomechanics

journal homepage: www.elsevier.com/locate/jbiomech
www.JBiomech.com

Cell and tissue deformation measurements: Texture correlation with third-order approximation of displacement gradients

Kai Y. Lim, Jonathan T. Henderson, Corey P. Neu *

Weldon School of Biomedical Engineering, Purdue University, West Lafayette, IN 47907, USA

ARTICLE INFO

Article history:
Accepted 4 July 2013

Keywords:
Texture correlation
Digital image correlation
Digital volume correlation
Cell and tissue mechanics
Subset entropy

ABSTRACT

Cells remarkably are capable of large deformations during motility and when subjected to mechanical force. Measurement of mechanical deformation (i.e. displacements, strain) is critical to understand functional changes in cells and biological tissues following disease, and to elucidate basic relationships between applied force and cellular biosynthesis. Microscopy-based imaging modalities provide the ability to noninvasively visualize small cell or tissue structures and track their motion over time, often using two-dimensional (2D) digital image (texture) correlation algorithms. For the measurement of complex and nonlinear motion in cells and tissues, implementation of texture correlation algorithms with high order approximations of displacement mapping terms are needed to minimize error. Here, we extend a texture correlation algorithm with up to third-order approximation of displacement mapping terms for the measurement of cell and tissue deformation. We additionally investigate relationships between measurement error and image texture, defined by subset entropy. Displacement measurement error is significantly reduced when the order of displacement mapping terms in the texture correlation algorithm matches or exceeds the order of the deformation observed. Displacement measurement error is also inversely proportional to subset entropy, with well-defined cell and tissue structures leading to high entropy and low error. For cell and tissue studies where complex or nonlinear displacements are expected, texture correlation algorithms with high order terms are required to best characterize the observed deformation.

1. Introduction

Cells and tissues in the body are capable of large deformation both *in vitro* and *in vivo*. In controlled studies by micropipette aspiration (Pravincumar et al., 2012) and optical tweezers (Henon et al., 1999), applied mechanical forces or pressure cause cells to undergo complex and viscoelastic changes in shape that relate to dynamics of the cytoskeleton. Flow and signal transduction pathways greatly influence cell polarization and motility with large changes to cellular shape (Maree et al., 2012). Red blood cells (Mills et al., 2004) and granulocytes (Evans and Kukan, 1984) undergo extreme deformations during flow. At the tissue level, excessive strain and strain rates have been linked to concussion in traumatic brain injury (Viano et al., 2005).

Because mechanical forces act upon our bodies, eliciting a diverse set of cellular responses, it is important to understand how our cells perceive and respond to force in the surrounding environment. One approach to address this question is to observe the cellular response to the mechanical forces and determine mechanistic relationships to the elicited chemical activity (Bershadsky et al., 2006; Janmey and McCulloch, 2007; Vogel and Sheetz, 2006; Zhu et al., 2000). To understand the influence of mechanical force on cells and tissues, unique methods are required to determine, in part, distributions of deformation (e.g. displacements and strain) throughout cellular subcomponents, including cytoskeleton, mitochondria, and the nucleus, as well as the surrounding tissue microenvironment (Gilchrist et al., 2004; Knight et al., 2006).

Texture correlation, a modified digital image correlation (DIC) procedure, utilizes the natural texture of biological tissues to measure displacement fields between two consecutive digital images (Bay, 1995). The texture correlation algorithm tracks the motion of a pixel within an image that is characterized by a unique intensity pattern defined by a subset of surrounding pixels. The displacement of the unique subset can be tracked by comparing images representing an object in a reference (i.e. initial) and deformed (i.e. current) configuration. Texture correlation has been applied to quantify bone, soft tissue, and intracellular deformations (Bay, 1995; Gilchrist et al., 2004,2007; Knight et al., 2006; Thompson et al., 2007; Wang et al., 2002; Zhang and Arola, 2004; Zhao and Simmons, 2012).

There are several unresolved concerns in the application of texture correlation algorithms to cell and tissue mechanics studies.

* Corresponding author. Tel.: +1 765 496 1426; fax: +1 765 494 0902.
E-mail address: cpneu@purdue.edu (C.P. Neu).

0021-9290/$ - see front matter © 2013 Elsevier Ltd. All rights reserved.
http://dx.doi.org/10.1016/j.jbiomech.2013.07.035

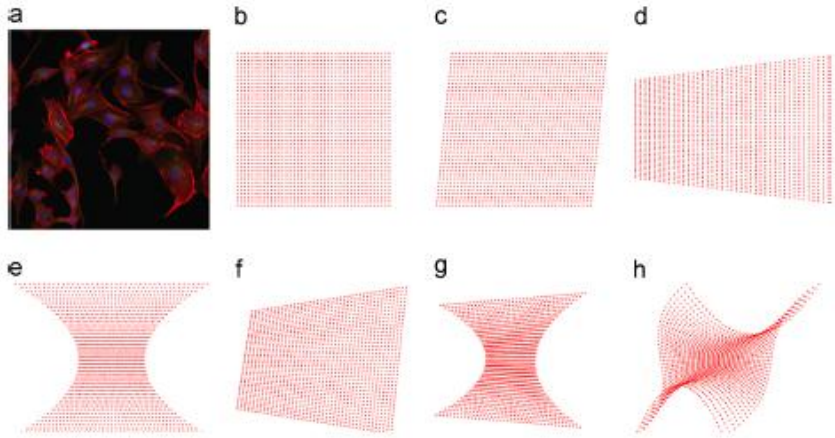

Fig. 1. Measurement error for a texture correlation algorithm with up to 3rd-order displacement mapping terms was determined using microscopy images and applied deformations. (a) Microscopy images of bovine pulmonary arterial endothelial (BPAE) cells revealed actin (Texas Red), microtubules (GFP), and nuclei (DAPI), which were merged for subsequent analysis in the study. Known deformation, defined by displacement mapping terms, was applied to subset points: (b) reference; (c) 1st-order deformation ($10\%\,\partial u/\partial y$); (d) 2nd-order deformation ($1\%\,\partial^2 v/\partial x\partial y$); (e) 3rd-order deformation ($1\%\,\partial^3 u/\partial x\partial^2 y$); (f) combination of 1st- and 2nd-order deformation ($10\%\,\partial u/\partial y + 1\%\,\partial^2 v/\partial x\partial y$); (g) combination of 1st-, 2nd-, and 3rd-order deformation ($10\%\,\partial u/\partial y + 0.5\%\,\partial^2 v/\partial x\partial y + 1\%\,\partial^3 u/\partial x\partial^2 y$), and (h) combination of 2nd- and 3rd-order deformation ($1\%\,\partial^2 v/\partial x\partial y + 1\%\,\partial^3 u/\partial^3 y + 1\%\,\partial^3 v/\partial^2 x\partial y$).

First, to reduce displacement measurement error for objects in complex motion, higher order (1st- and 2nd-order) displacement mapping terms were introduced to the algorithm (Chu et al., 1985; Lu and Cary, 2000; Vendroux and Knauss, 1998). However, for most studies of cell and tissue deformation, only 1st-order algorithms have been used to date (Gilchrist et al., 2004; Knight et al., 2006; Wang et al., 2002). High order approximations for displacement mapping terms may be required to best describe complex cell and tissue motion, especially when long image acquisition times limit the ability to visualize temporal changes, often occurring on millisecond time scales (e.g. (Pravincumar et al., 2012; Viano et al., 2005)). A related concern is that the distinct intensity patterns needed for texture correlation might not be found in small subset regions, especially in the extracellular matrix or the cytoplasm. A relatively large subset region (on the order of tens by tens of square pixels) may be necessary to provide a unique pattern that is tracked using the algorithm. In this case, however, linear deformation mapping may not be appropriate in the large subset region to characterize internal motion.

Second, relationships between the subset texture and measurement error of the algorithm have been largely unexplored. Two methods have typically been used to define subset texture: subset entropy and subset roughness (Gilchrist et al., 2004; Haralick et al., 1973; Sun and Pang, 2007). Subset entropy is a statistical measure of randomness of pixel values within a subset, in comparison to the entire image. Subset roughness depends on the standard deviation of the pixel values within a subset. Previous studies demonstrated an increase in subset entropy or roughness with the measurement accuracy. However, previous results were typically obtained using a single-loop simulation, i.e. only a pair of pre- and post-deformation images was used. Since texture correlation algorithms are sensitive to the image noise, it is not clear how the magnitude of error varies over multiple simulations representing arbitrary images acquired with superimposed random noise, a case more closely representing practical application of the algorithm.

In this study, we propose a texture correlation algorithm enabling higher order (up to 3rd-order Taylor series) approximation of the displacement gradients. We compare the utility of texture correlation with 0th-, 1st-, 2nd-, and 3rd-order displacement gradients for cell and tissue mechanics studies. Furthermore, we applied Monte-Carlo simulations to determine the relationship between subset texture, defined by entropy, and the error of displacement measurements.

2. Methods

2.1. Texture correlation algorithm

In this study, a texture correlation algorithm with up to 3rd-order displacement mapping terms was implemented. Texture correlation algorithms, that included 0th-, 1st-, and 2nd-order terms, were previously presented by Bay (Bay, 1995), Vendroux and Knauss (Vendroux and Knauss, 1998), and Lu and Cary (Lu and Cary, 2000), respectively. The 3rd-order algorithm is an expansion of the 2nd-order algorithm, considering deformation in two dimensions, with pixels of interest identified in image pairs that depict an object in reference (original) and deformed (current) configurations. For each point (e.g. pixel) of interest in the reference image, local texture centered about the point was defined using image intensity values in a square subset of pixels. The coordinates of each subset point in the reference image, (x, y), were mapped to their counterpart in the deformed image, $(\bar{x}, \bar{y})$, using

$$\begin{aligned} \bar{x} &= x_0 + U(x, y) \\ \bar{y} &= y_0 + V(x, y) \end{aligned} \tag{1}$$

where U and V are the displacement components of each subset point. U and V can be approximated utilizing up to 3rd-order Taylor series expansion about a pixel of interest (x_0, y_0), as detailed in the Appendix. Briefly, the Taylor series expansion includes up to twenty displacement parameters, and allowed for the representation of complex deformations (Fig. 1). Bicubic spline interpolation was introduced to describe motion, in addition to a scaling parameter, w, to account for differences in reference and deformed image intensities. To find the mapping parameters, U and V, a least-squares correlation coefficient and Newton–Raphson optimization method was implemented. Importantly, a simple demonstration code for the algorithm, 'TextureCorrDemo.m', is available for download as a supplement online.

2.2. Cellular-scale images and simulated deformation

To compare the utility of a texture correlation algorithm with 0th-, 1st-, 2nd-, and 3rd-order displacement mapping terms, reference and deformed images of single cells were acquired and simulated, respectively. An image of bovine pulmonary artery endothelial (BPAE) cells (Invitrogen Inc., Carlsbad, CA), a model cell type with representative cytoskeletal and nuclear structures expected in a broad range of eukaryotic cells, was acquired by widefield fluorescent microscopy

(EclipseTi, Nikon Inc., Melville, NY). Actin (Texas Red), microtubules (GFP), and nuclei (DAPI) were visualized and merged into a single reference image for subsequent analysis (Fig. 1a). Deformed images were generated using the reference image and known deformations of increasing (0th-, 1st-, 2nd, and 3rd-order) complexity using closed-form solutions and MATLAB (R2010b, Mathworks, Natick, MA) software. For the 0th-order deformation, a translation of 5, 10, or 15 pixels in a horizontal ($+y$) direction was applied to the reference image. For the 1st-order deformations, 0, 10, 20, 30 or 40% shear ($\partial u/\partial y$) was applied in addition to the aforementioned 5 pixels translation. For the 2nd-order deformations, 0, 0.5, 1, or 1.5% $\partial^2 v/\partial x \partial y$ was applied in combination with the 5 pixels translation and 10% shear ($\partial u/\partial y$). For the 3rd-order deformation, 0.5, 1.0, or 1.5% $\partial^3 u/\partial x \partial^2 y$ was applied in addition to the 5 pixels translation, 10% shear ($\partial u/\partial y$), and 0.5% $\partial^2 v/\partial x \partial y$. The intensity value of each pixel in the (simulated and) deformed image was then determined by cubic spline interpolation.

2.3. Measurement error with 0th-, 1st-, 2nd-, or 3rd-order approximations of displacement gradients

Measurement error was estimated for a texture correlation algorithm with multi-order displacement mapping terms implemented in MATLAB software. To characterize deformation throughout the population of cells (Fig. 1a), a set of points of interest ($n = 20$) was randomly selected within the cells in the reference image. The same set of points, each with a subset size of 31×31 pixels determined using a gray level co-occurrence matrix (Lane et al., 2008), was chosen for every pair of test (reference and deformed) images. Displacements of each point were determined using the texture correlation algorithm with 0th-, 1st-, 2nd-, or 3rd-order terms. The 0th-order algorithm calculated displacement refined to the nearest 1/16th pixel using bicubic spline interpolation. For higher-order algorithms, in order to apply Newton–Raphson optimization method, an initial guess of displacement was needed, which was provided by the 0th-order algorithm. The measurement errors for each algorithm were then compared by calculating the radial distance error (RDE), defined as the square root of the sum of perpendicular axial errors.

2.4. Tissue-scale images and relationships between error and entropy

To extend the algorithm for tissue-scale studies, and to establish relationships between measurement error and entropy, addition studies were conducted using explanted articular cartilage explants. Fresh-frozen juvenile bovine cartilage explants (full thickness, diameter = 5 mm) were imaged by confocal microscopy. Explants were cut along the depth direction to reveal an internal flat (cut) surface of the explant hemisphere for imaging. Collagen (predominantly type II) of the cartilage extracellular matrix (ECM) was imaged using confocal reflection microscopy with an Olympus Fluoview FV1000 microscope system (488 nm) (Olympus Corp., Tokyo, Japan). Additionally, compared to images of BPAE cells, imaging of the ECM provided larger range of entropy, computed as a statistical measure of randomness and used to characterize the image texture at each pixel of interest (MATLAB).

Monte Carlo simulations were used to estimate a relationship between the measurement error of displacement and entropy for microscopy-based images. Simulations were used because error, expected to be a function of object displacement and noise from the imaging system, was not known *a priori*. For simulations, the image of the ECM was used as the reference image. A simple 10 pixels horizontal translation, chosen to be representative of common small motion observed in cell and tissue studies (Chan and Neu, 2012), was applied to generate a deformed image. For each of the 100 simulation iterations, and to mimic the signal-to-noise observed in our microscopy images, random (Gaussian) noise with zero mean and a standard deviation of 0.30 was applied separately to the reference and deformed image. A set of sampling points ($n = 120$) was randomly selected on the ECM image, with the condition that at least 15 data points should be chosen for each equally spaced entropy interval observed (ranging from 1 to 7). The texture correlation algorithm with 3rd-order displacement mapping terms was used, with a subset size of 19×19 pixels (Lane et al., 2008) for each sampling point. RDE and radial angular error (RAE) were calculated for each point in all the simulation iterations. Radial angle was defined as the inverse tangent of the ratio of y-location to x-location. RAE is the difference between the expected radial angle and the measured radial angle. The number of successful convergence for each sampling point was also counted. Graphs of average RDE and average RAE versus entropy were plotted, and a power curve with 95% confidence level was fitted to the average RDE versus entropy graph. Importantly, greater than 100 iterations did not change the results presented herein significantly (Neu et al., 2005; Neu and Walton, 2008).

2.5. Statistical analysis

To compare error for algorithm of varying orders, a one-way analysis of variance was performed using standard statistical software (Minitab 16.1, Minitab Inc., State College, PA). Multiple comparisons among algorithms for each applied deformation was evaluated using a post-hoc Tukey's honestly significant difference test.

3. Results

3.1. Measurement error with 0th-, 1st-, 2nd-, or 3rd-order approximations of displacement gradients

Measurement error for texture correlation algorithms depends on the inclusion of high order approximations of displacement gradients and on the order of the deformation observed. For 0th-order deformations, the algorithm with 0th-order displacement gradients produced an average RDE of 0.079 ± 0.021 pixels over the range of applied displacements. Inclusion of higher (i.e. 1st-, 2nd-, and 3rd-) order approximations produced displacements that matched the expected values for the imaged cells (i.e. RDE = 0 pixels).

For applied 1st-order deformations (Fig. 2a), the texture correlation algorithm with included 1st-, 2nd-, and 3rd-order approximations of the displacement gradient provided comparable measurement errors. Regardless of the magnitude of 1st-order deformation, the measurement error of the algorithm with a 0th-order approximation was significantly larger compared to the algorithm with included higher order approximations ($p < 0.001$). The average RDE increased with increased percent shear for all algorithms, although the average RDE produced by the 0th-algorithm showed the most dramatic changes, increasing from 373% of that produced by 1st-, 2nd-, and 3rd-order algorithm in 10% shear to 652% in 30% shear.

With an increase in the magnitude of 2nd-order deformation (Fig. 2b), the average RDE produced by the algorithm with 0th- and 1st-order terms were similar, while error from the algorithm when 2nd- and 3rd-order terms were included remained lower by an order of magnitude. The average RDE produced by the algorithm with 0th- and 1st-order terms was significantly larger than that produced by the algorithm when 2nd- and 3rd-order terms were included ($p < 0.001$) when the magnitude of 2nd-order deformation exceeded 0.5% $\partial^2 v/\partial x \partial y$.

For applied 3rd-order deformations, the average RDEs for each implementation of the algorithm was not significantly different when the magnitude of deformation was 0.5% $\partial^3 u/\partial x \partial^2 y$. However, when the magnitude of deformation exceeded 0.5%, the average RDE produced by the algorithm with 3rd-order terms was significantly lower than the other algorithms with lower order terms ($p < 0.003$) (Fig. 2c).

3.2. Tissue-scale Images and relationships between error and entropy

The Monte Carlo simulation revealed that the measurement error of displacement was inversely proportional to the subset entropy (Fig. 3). A power relationship was determined for the RDE data, with $RDE = 5.1 \times entropy^{-4.516}$, and $R^2 = 0.87$. With entropy larger than 3, the RDE dropped to within 0.01 pixels. The similar relationship was shown between the RAE and the entropy. The RAE was small even with low entropy (RAE = ± 0.00015 rad or $\pm 0.0086°$) and it decreased drastically with the increase in entropy. In addition, the number of successful convergence reached by the 3rd-order algorithm in the 100-loop simulations was directly proportional ($R^2 = 0.88$) to the entropy.

4. Discussion

The purpose of our work was to extend a texture correlation algorithm to include 3rd-order approximations for displacement gradients to minimize potential errors in characterizing large deformation in cells and biological tissues. The main findings of our work are: (1) to minimize error, the order of approximations for displacement gradients in the texture correlation algorithm

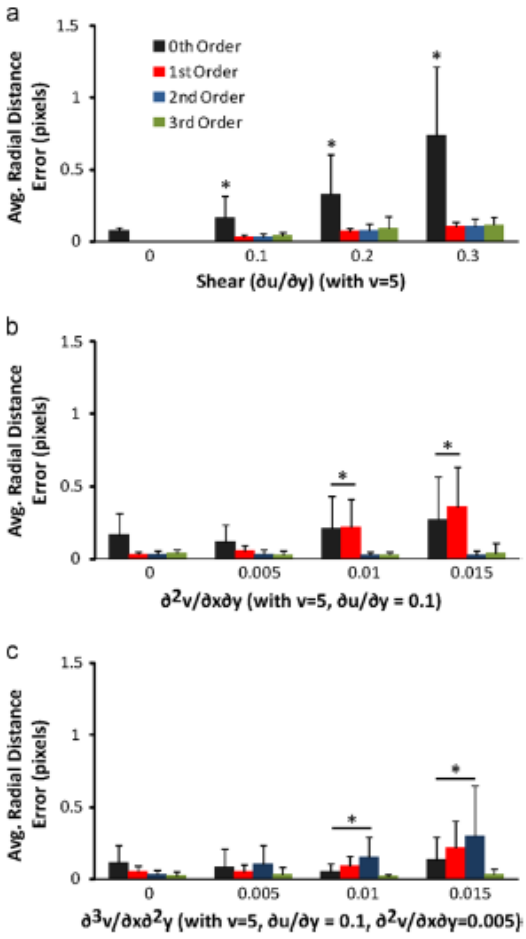

Fig. 2. Measurement error is minimized when the order of displacement mapping terms in the texture correlation algorithm matches or exceeds the order of the deformation images of cells. (a) The 1st-order deformations applied were 0, 10, 20 and 30% $\partial u/\partial y$, together with 5 pixels translation in v. The 1st-, 2nd-, and 3rd-order algorithms provided comparable error while the average RDE produced by the 0th-order was consistently larger than other algorithms ($p < 0.001$). (b) The 2nd-order deformations with 0, 0.5, 1, and 1.5% $\partial^2 v/\partial x\partial y$, in addition to 5 pixels translation in v and 10% $\partial u/\partial y$. When the $\partial^2 v/\partial x\partial y$ magnitude was larger than 0.5%, the 0th- and 1st-order algorithms produced average RDE larger than the 2nd- and 3rd-order algorithms ($p < 0.001$). (c) For the 3rd-order deformations with 0, 0.5, 1, and 1.5% $\partial^3 u/\partial x\partial^2 y$, in addition to 5 pixels translation in v, 10% $\partial u/\partial y$, and 1.5% $\partial^2 v/\partial x\partial y$. The average RDE produced by the 3rd-order algorithm was significantly lower than those by the lower order algorithm when deformation magnitude exceeded 0.5% $\partial^3 u/\partial x\partial^2 y$ ($p < 0.003$) * = significant difference from unmarked bars in the group, with aforementioned p-values.

must match or exceed the order of the expected deformation in the imaged object (i.e. cell or tissue); (2) the use of higher order displacement mapping terms decreases the measurement error; (3) the measurement error of displacement is inversely proportional to the subset entropy; (4) the occurrence of successful convergence is directly proportional to the subset entropy.

Error in measured displacement can be minimized when the order of displacement mapping terms of the texture correlation algorithm matches or exceeds the order of the deformation in images of cells or tissues. The higher order displacement mapping terms act as modifiers to the measured displacements to help to decrease the measurement error. Even in the 0th-order cell deformations, where error produced by 0th-order algorithm was small (0.080 ± 0.021 pixels), the 1st- and 2nd-order algorithms eliminated the measurement errors (mean and SD = 0 pixels). This finding may be particularly important in cell mechanics studies. For instance, in the study of chondrocyte mechanotransduction, it is speculated that the intracellular structure and organization in single chondrocytes is inherently different from one another with a diversity of response to mechanical stimuli that is observed within a heterogeneous cell population (Knight et al., 2006; Lee et al., 2000). Thus, to account for variable deformation types that may be encountered within a cell population, a higher order algorithm may be necessary to overcome errors expected with the use of lower order algorithms alone. Furthermore, high order displacement mapping terms may be needed even when relatively simple motion is acquired with a low temporal resolution, where motion (e.g. migration) may accumulate.

The use of higher order displacement mapping terms decreased the measurement error. For 1st-order deformation, due to the linear deformation within the subset, the assumption made by the 0th-order algorithm that a subset remains square after deformation was not valid, and thus the measurement error increased. The measurement error was not different for the algorithm with 1st-, 2nd-, and 3rd-order approximations. By adding in 2nd-order deformation, non-linear deformation occurred within each subset. Even with a slight 2nd-order deformation ($\partial^2 v/\partial x\partial y = 0.005$), the average RDE produced by the 0th- and 1st-order algorithms increased. The error increased further with the increase in deformation magnitude. The same was observed in the 3rd-order deformation. The average RDE produced by the 0th-, 1st-, and 2nd-order algorithms increased with the increase in the magnitude of the 3rd-order deformation while the 3rd-order algorithm provided identical measurement error.

The high computational cost required for the 1st-, 2nd-, and 3rd-order algorithms is offset by the fast convergence rate characteristic of the Newton-Raphson optimization process (Lu and Cary, 2000). With a subset size of 31×31 pixels, the computational time of each pixel of interest required for the 0th-order algorithm with displacement refined to the nearest 1/16th pixel was 8.2 s while that for the 1st-, 2nd-, and 3rd-order algorithms added only 4.4, 5.2 and 6.1 s, respectively.

Since the texture correlation algorithm utilizes the natural texture of biological tissue and cells, the measurement error depends strongly on the unique subset texture within an image. Consequently, quantification of subset texture is important to estimate the error expected for a given point of interest. The inversely proportional relationship between the subset entropy and the RDE obtained in our study agreed with the results shown in previous studies (Gilchrist et al., 2004; Sun and Pang, 2007). Although two different methods were used to quantify subset texture, namely the subset roughness and entropy, there was a linear relationship between the two ($R^2 = 0.710$). The two quantification methods were considered interchangeable, and in this study, only subset entropy was applied. Moreover, the application of Monte Carlo simulation helps to mimic the real and practical effects of imaging, i.e. the random noise added through the use of microscopy systems during the acquisition of any given pair of images. In previous studies, only a fixed pair of digital images was used to determine the relationship between the measurement accuracy and the subset texture. The aforementioned error of the algorithm is sensitive to the subset texture, which in turn is sensitive to the noise superimposed by the imaging device. As a result, the effect of random noise, included through Monte Carlo simulations, is

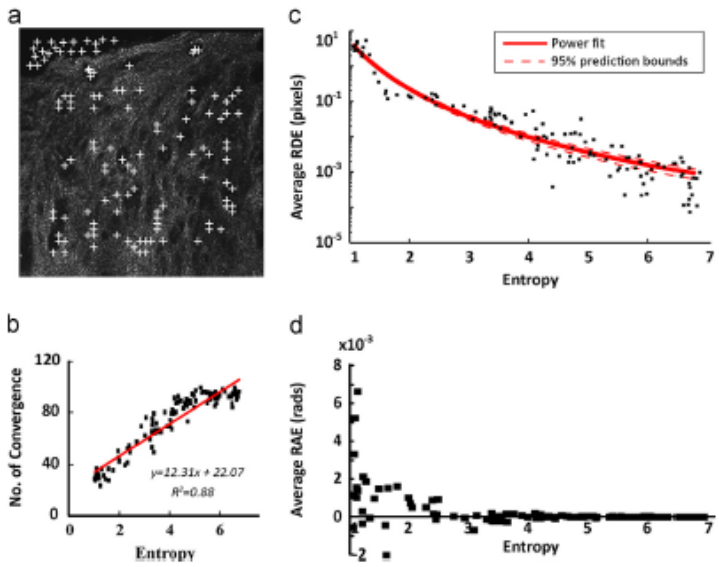

Fig. 3. Measurement error is inversely proportional to subset entropy, while the occurrence of convergence is directly proportional to subset entropy. (a) Monte Carlo simulations of deformation were performed to estimate radial displacement error (RDE) and radial angular error (RAE) at 120 randomly generated data points (marked as "+") in the image of the tissue extracellular matrix. (b) The occurrence of convergence of the texture correlation algorithm increased with subset entropy, and reached a value of 75% when the entropy was larger than 3.5. (c) The RDE decreased with the increase in subset entropy. (d) The average RAE dropped drastically with the increase in subset entropy, compared to the RDE case in (c).

required to best estimate relationships between image parameters and error.

Based on the mathematical relationship between subset entropy and RDE obtained through the Monte Carlo simulations, it is possible to estimate the range of measurement error that might be encountered when applying the texture correlation algorithm to arbitrary images. For example, using $RDE = 5.1 \times entropy^{-4.516}$, we can estimate the range of RDE in the cell and tissue images (Fig. 4), identifying regions of expected high and low measurement errors. It is important to note that when a different type of (e.g. magnetic resonance) imaging device is used, due to the different technical specifications, a separate Monte Carlo simulation may be needed in order to obtain an appropriate mathematical relationship. For the BPAE cells (Fig. 4b), large RDE was observed (as expected) in the extracellular region where the entropy values are low compared to the intracellular structure.

In the Monte Carlo simulation using the 3rd-order algorithm, we observed that the occurrence of successful convergence increased with the subset entropy. However, since the deformation type applied was a 0th-order deformation, i.e. horizontal translation, successful convergence may decrease if higher order motion is encountered. Also, the region of low entropy (in the range of 1 to 2.5) corresponded to noisy background regions without any visualized cell components. With a subset entropy larger than 3.5, the successful convergence rate reached at least 75%. Therefore, if high order motion is suspected, a high order algorithm is advised, and must be applied with caution since convergence for all 21 parameters is not always achieved, especially in regions with low entropy. If needed, convergence criteria may be adjusted to enable a best estimate of the result for higher order motion, for example through averaging of the parameter values in the last few loops of the optimization process.

While the 3rd-order algorithm in this study considered deformation in two dimensions, the algorithm can be naturally extended for studies in three dimensions. For a 3D implementation, additional displacement mapping parameters (see Appendix) would be required to account for (out of plane) motion, with an associated higher computational cost and slower convergence rate. Also, it is not clear whether errors computed in 2D (Fig. 2) would be comparable to those measured in 3D. One important consideration is the need to acquire multiple image slices (i.e. as a z-stack of confocal microscopy images) to visualize cells or tissues, which are often separated at a distance that is perhaps an order of magnitude larger than the (in-plane) image spatial resolution. Therefore, close packing of image slices is likely required, and necessary 3D spline interpolation to account for motion would further increase the computational time.

In conclusion, in order to contain all deformation types that may be encountered in cell and tissue mechanics studies, a higher order algorithm is needed. However, since convergence for all 21 parameters in the algorithm is not always achieved, an algorithm with high order approximation of displacement terms must be applied with caution. Additionally, high entropy in a subset of pixels is needed to minimize displacement errors, and can be achieved through increases in the signal-to-noise ratio and spatial resolution of microscopy images, often at the cost of spatial resolution, thereby requiring a texture correlation algorithm with increased (up to 3rd-order) approximations of displacement gradients. Application of the algorithm to other imaging modalities, e.g. magnetic resonance imaging (Neu et al., 2005; Neu and Walton, 2008), may also be possible, provided high entropy of pixel subsets is achieved to minimize error.

Conflict of interest statement

There are no conflicts of interest to report.

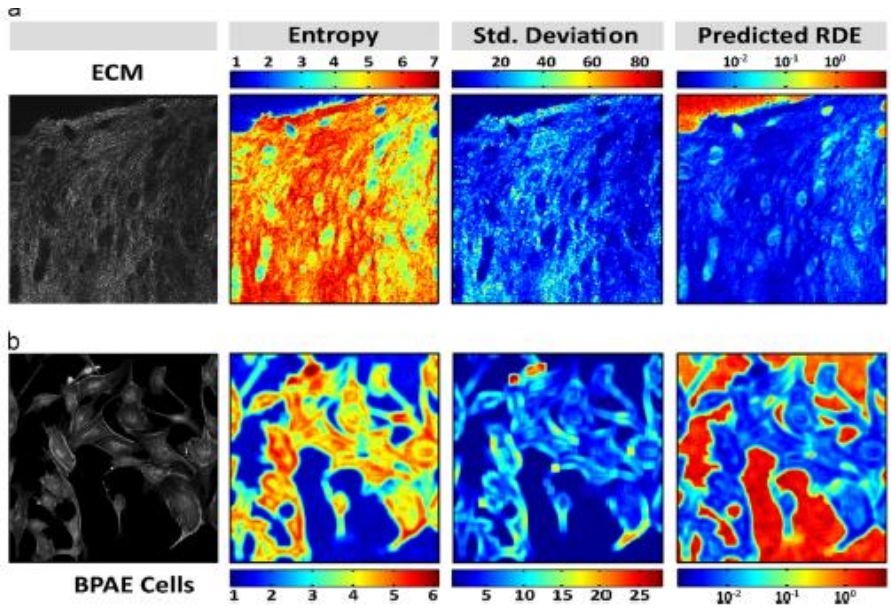

Fig. 4. The texture of an image, defined by entropy, allows for the predicted RDE at each potential point of interest for the determination of displacement fields by texture correlation. The relationship between RDE and subset entropy obtained through Monte Carlo simulations (Fig. 3c) provides estimates of RDE in images acquired by microscopy systems. The original image, the entropy, and the predicted RDE plot are shown for (a) image of the tissue extracellular matrix (ECM) and (b) image of BPAE cells. Another measure of texture, the standard deviation of image intensities, corresponds to entropy images, and may alternatively be used to predict the RDE at a point of interest.

Acknowledgments

This work was supported in part by the Summer Undergraduate Research Fellowship (SURF) at Purdue University (to KYL) and the Andrews Fellowship (to JTH).

Appendix

The implementation of a third order texture correlation algorithm, available as a simple demonstration code and supplement online, extends the work of Bay (Bay, 1995), Vendroux and Knauss (Vendroux and Knauss, 1998), and Lu and Cary (Lu and Cary, 2000). Here, coordinates of subset points in the reference image, (x, y), are mapped to their deformed coordinates, $(\tilde{x}, \tilde{y})$, using

$$\tilde{x} = x_0 + U(x, y)$$
$$\tilde{y} = y_0 + V(x, y) \tag{2}$$

with U and V as displacement components of each subset point. U and V can be approximated with a third-order Taylor series expansion about the pixel of interest (x_0, y_0), leading to:

$$\tilde{x} = x + U_0 + U_x\Delta x + U_y\Delta y + \frac{1}{2}U_{xx}\Delta x^2 + \frac{1}{2}U_{yy}\Delta y^2 + U_{xy}\Delta x\Delta y + \frac{1}{6}U_{xxx}\Delta x^3 + \frac{1}{6}U_{yyy}\Delta y^3 + \frac{1}{2}U_{xyy}\Delta x\Delta y^2 + \frac{1}{2}U_{xxy}\Delta x^2\Delta y$$

$$\tilde{y} = y + V_0 + V_x\Delta x + V_y\Delta y + \frac{1}{2}V_{xx}\Delta x^2 + \frac{1}{2}V_{yy}\Delta y^2 + V_{xy}\Delta x\Delta y + \frac{1}{6}V_{xxx}\Delta x^3 + \frac{1}{6}V_{yyy}\Delta y^3 + \frac{1}{2}V_{xyy}\Delta x\Delta y^2 + \frac{1}{2}V_{xxy}\Delta x^2\Delta y \tag{3}$$

A Taylor series expansion introduces up to twenty displacement parameters for a third-order description of motion, with $\Delta x = x - x_0$ and $\Delta y = y - y_0$. U_0 and V_0 are the zeroth-order displacement parameters at (x_0, y_0). U_x, U_y, V_x, and V_y are first-order displacement gradients; U_{xx}, U_{yy}, U_{xy}, V_{xx}, V_{yy}, and V_{xy} are second-order displacement gradients; and U_{xxx}, U_{yyy}, U_{xyy}, U_{xxy}, V_{xxx}, V_{yyy}, V_{xyy}, and V_{xxy} are third-order displacement gradients. Complex deformation of a subset of pixels can be represented using the 1st-, 2nd-, and 3rd-order displacement gradients (Fig. 1).

Bicubic spline interpolation was implemented to obtain determine grayscale pixel intensities and ensure continuous gradients at any location within the reference and deformed images. Differences in image intensities (e.g. brightness) between reference and deformed images was accounted for using a scaling parameter, w, as follows:

$$h(\tilde{x}, \tilde{y}) = \sum_{m=0}^{3}\sum_{n=0}^{3} \beta_{mn}\tilde{x}^m\tilde{y}^n + w \tag{4}$$

where h is the intensity value at pixel $(\tilde{x}, \tilde{y})$ in the deformed image, and β_{mn} is the bicubic spline coefficient.

A least-squares correlation coefficient, C, is used to determine optimal displacement parameters, defined as:

$$C = \frac{\sum_{S_p \in S}\{g(S_p) - h(S_p, \mathbf{P})\}^2}{\sum_{S_p \in S} g^2(S_p)} \tag{5}$$

For the optimization, g and h are the intensity values in the reference and deformed images, respectively, and S is the subset of pixels centered about the pixel of interest, with S_p as each subset pixel within S. P represents the twenty-one mapping parameters, i.e. U_0, V_0, U_x, U_y, V_x, V_y, U_{xx}, U_{yy}, U_{xy}, V_{xx}, V_{yy}, V_{xy}, U_{xxx}, U_{yyy}, U_{xyy}, U_{xxy}, V_{xxx}, V_{yyy}, V_{xyy}, V_{xxy}, and w. The correlation coefficient, C, was

minimized when P represents the displacement parameters that best represent the deformation. A simplified Newton-Raphson optimization method was implemented to find the minimum value of C, as:

$$\nabla\nabla C(P_0)(P-P_0) = -\nabla C(P_0) \tag{6}$$

with P_0 representing the initial guess of the solution and P representing the next iterative approximate solution. $\nabla\nabla C$, a second order gradient, or Hessian Matrix, of C can be approximated following Vendroux and Knauss (Vendroux and Knauss, 1998):

$$\nabla\nabla C(P) = \left[\frac{\partial^2 C}{\partial P_i \partial P_j}\right]_{i,j=[1,21]} \approx \left[\frac{2}{\sum_{S_p \in S} g^2(S_p)} \sum_{S_p \in S} \frac{\partial h(S_p, P)}{\partial P_i} \frac{\partial h(S_p, P)}{\partial P_j}\right]_{i,j=[1,21]} \tag{7}$$

where P_i represents the ith element of the displacement parameter vector P. Here, the equations for the first-derivatives of h with respect to the displacement mapping parameters are:

$\frac{\partial h}{\partial U} = \frac{\partial h}{\partial x}$	$\frac{\partial h}{\partial V} = \frac{\partial h}{\partial y}$
$\frac{\partial h}{\partial U_x} = \frac{\partial h}{\partial x}\Delta x$	$\frac{\partial h}{\partial V_x} = \frac{\partial h}{\partial y}\Delta x$
$\frac{\partial h}{\partial U_y} = \frac{\partial h}{\partial x}\Delta y$	$\frac{\partial h}{\partial V_y} = \frac{\partial h}{\partial y}\Delta y$
$\frac{\partial h}{\partial U_{xx}} = \frac{1}{2}\frac{\partial h}{\partial x}\Delta x^2$	$\frac{\partial h}{\partial V_{xx}} = \frac{1}{2}\frac{\partial h}{\partial y}\Delta x^2$
$\frac{\partial h}{\partial U_{yy}} = \frac{1}{2}\frac{\partial h}{\partial x}\Delta y^2$	$\frac{\partial h}{\partial V_{yy}} = \frac{1}{2}\frac{\partial h}{\partial y}\Delta y^2$
$\frac{\partial h}{\partial U_{xy}} = \frac{\partial h}{\partial x}\Delta x\Delta y$	$\frac{\partial h}{\partial V_{xy}} = \frac{\partial h}{\partial y}\Delta x\Delta y$
$\frac{\partial h}{\partial U_{xxx}} = \frac{1}{6}\frac{\partial h}{\partial x}\Delta x^3$	$\frac{\partial h}{\partial V_{xxx}} = \frac{1}{6}\frac{\partial h}{\partial y}\Delta x^3$
$\frac{\partial h}{\partial U_{yyy}} = \frac{1}{6}\frac{\partial h}{\partial x}\Delta y^3$	$\frac{\partial h}{\partial V_{yyy}} = \frac{1}{6}\frac{\partial h}{\partial y}\Delta y^3$
$\frac{\partial h}{\partial U_{xyy}} = \frac{1}{2}\frac{\partial h}{\partial x}\Delta x\Delta y^2$	$\frac{\partial h}{\partial V_{xyy}} = \frac{1}{2}\frac{\partial h}{\partial y}\Delta x\Delta y^2$
$\frac{\partial h}{\partial U_{xxy}} = \frac{1}{2}\frac{\partial h}{\partial x}\Delta x^2\Delta y$	$\frac{\partial h}{\partial V_{xxy}} = \frac{1}{2}\frac{\partial h}{\partial y}\Delta x^2\Delta y$
$\frac{\partial h}{\partial w} = 1$	[8]

with $\partial h/\partial\tilde{x}$ and $\partial h/\partial\tilde{y}$ as the partial derivatives of the bicubic spline interpolation polynomial of the deformed image. The partial derivatives can be obtained by the following equations:

$$\begin{aligned}\frac{\partial h}{\partial \tilde{x}} &= \beta_{10} + \beta_{11}\tilde{y} + \beta_{12}\tilde{y}^2 + \beta_{13}\tilde{y}^3 + 2\beta_{20}\tilde{x} + 2\beta_{21}\tilde{x}\tilde{y} \\ &\quad + 2\beta_{22}\tilde{x}\tilde{y}^2 + 2\beta_{23}\tilde{x}\tilde{y}^3 + 3\beta_{30}\tilde{x}^2 + 3\beta_{31}\tilde{x}^2\tilde{y} + 3\beta_{32}\tilde{x}^2\tilde{y}^2 + 3\beta_{33}\tilde{x}^2\tilde{y}^3\end{aligned}$$

$$\begin{aligned}\frac{\partial h}{\partial \tilde{y}} &= \beta_{01} + 2\beta_{02}\tilde{y} + 3\beta_{03}\tilde{y}^2 + \beta_{11}\tilde{x} + 2\beta_{12}\tilde{x}\tilde{y} + 3\beta_{13}\tilde{x}\tilde{y}^2 + \beta_{21}\tilde{x}^2 \\ &\quad + 2\beta_{22}\tilde{x}^2\tilde{y} + 3\beta_{23}\tilde{x}^2\tilde{y}^2 + \beta_{31}\tilde{x}^3 + 2\beta_{32}\tilde{x}^3\tilde{y} + 3\beta_{33}\tilde{x}^3\tilde{y}^2\end{aligned} \tag{9}$$

Appendix A. Supporting information

Supplementary data associated with this article can be found in the online version at http://dx.doi.org/10.1016/j.jbiomech.2013.07.035.

References

Bay, B.K., 1995. Texture correlation: a method for the measurement of detailed strain distributions within trabecular bone. Journal of Orthopaedic Research 13, 258–267.

Bershadsky, A., Kozlov, M., Geiger, B., 2006. Adhesion-mediated mechanosensitivity: a time to experiment, and a time to theorize. Current Opinion in Cell Biology 18, 472–481.

Chan, D.D., Neu, C.P., 2012. Transient and microscale deformations and strains measured under exogenous loading by noninvasive magnetic resonance. PLoS One 7, e33463.

Chu, T.C., Ranson, W.S., Sutton, M.A., Peters, W., 1985. Applications of digital image correlation techniques to experimental mechanics. Experimental Mechanics 25, 232–244.

Evans, E., Kukan, B., 1984. Passive material behavior of granulocytes based on large deformation and recovery after deformation tests. Blood 64, 1028–1035.

Gilchrist, C.L., Xia, J.Q., Setton, L.A., Hsu, E.W., 2004. High-resolution determination of soft tissue deformations using MRI and first-order texture correlation. IEEE Transactions on Medical Imaging 23, 546–553.

Gilchrist, C.L., Witvoet-Braam, S.W., Guilak, F., Setton, L.A., 2007. Measurement of intracellular strain on deformable substrates with texture correlation. Journal of Biomechanics 40, 786–794.

Haralick, R.M., Shanmugam, K., Dinstein, I., 1973. Textural features for image classification. IEEE Transactions on Systems, Man, and Cybernetics SMC-3, 610–621.

Henon, S., Lenormand, G., Richert, A., Gallet, F., 1999. A new determination of the shear modulus of the human erythrocyte membrane using optical tweezers. Biophys Journal 76, 1145–1151.

Janmey, P.A., McCulloch, C.A., 2007. Cell mechanics: integrating cell responses to mechanical stimuli. Annual Review of Biomedical Engineering 9, 1–34.

Knight, M.M., Bomzon, Z., Kimmel, E., Sharma, A.M., Lee, D.A., Bader, D.L., 2006. Chondrocyte deformation induces mitochondrial distortion and heterogeneous intracellular strain fields. Biomechanics and Modeling in Mechanobiology 5, 180–191.

Lane, C., Burguet, R.L., Shterenlikht, A., 2008. Year An objective criterion for the selection of an optimum DIC pattern and subset size. In: Proceedings of the SEM Annual Conference. Orlando, FL.

Lee, D.A., Knight, M.M., Bolton, J.F., Idowu, B.D., Kayser, M.V., Bader, D.L., 2000. Chondrocyte deformation within compressed agarose constructs at the cellular and sub-cellular levels. Journal of Biomechanics 33, 81–95.

Lu, H., Cary, P.D., 2000. Deformation measurements by digital image correlation: implementation of a second-order displacement gradient. Experimental Mechanics 40, 393–400.

Maree, A.F., Grieneisen, V.A., Edelstein-Keshet, L., 2012. How cells integrate complex stimuli: the effect of feedback from phosphoinositides and cell shape on cell polarization and motility. PLOS Computational Biology 8, e1002402.

Mills, J.P., Qie, L., Dao, M., Lim, C.T., Suresh, S., 2004. Nonlinear elastic and viscoelastic deformation of the human red blood cell with optical tweezers. Mechanics and chemistry of biosystems 1, 169–180.

Neu, C.P., Walton, J.H., 2008. Displacement encoding for the measurement of cartilage deformation. Magnetic Resonance in Medicine 59, 149–155.

Neu, C.P., Hull, M.L., Walton, J.H., 2005. Error optimization of a three-dimensional magnetic resonance imaging tagging-based cartilage deformation technique. Magnetic Resonance in Medicine 54, 1290–1294.

Pravincumar, P., Bader, D.L., Knight, M.M., 2012. Viscoelastic cell mechanics and actin remodelling are dependent on the rate of applied pressure. PLoS One 7, e43938.

Sun, Y., Pang, J., 2007. Study of optimal subset size in digital image correlation of speckle pattern images. Optics and Lasers in Engineering 45, 967–974.

Thompson, M.S., Schell, H., Lienau, J., Duda, G.N., 2007. Digital image correlation: a technique for determining local mechanical conditions within early bone callus. Medical Engineering and Physics 29, 820–823.

Vendroux, G., Knauss, W.G., 1998. Submicron deformation field measurements: Part 2. Improved digital image correlation. Experimental Mechanics 38, 86–92.

Viano, D.C., Casson, I.R., Pellman, E.J., Zhang, L., King, A.I., Yang, K.H., 2005. Concussion in professional football: brain responses by finite element analysis: part 9. Neurosurgery 57, 891–916. (discussion 891-916).

Vogel, V., Sheetz, M., 2006. Local force and geometry sensing regulate cell functions. Nature Reviews Molecular Cell Biology 7, 265–275.

Wang, C.C., Deng, J.M., Ateshian, G.A., Hung, C.T., 2002. An automated approach for direct measurement of two-dimensional strain distributions within articular cartilage under unconfined compression. Journal of Biomechanical Engineering 124, 557–567.

Zhang, D., Arola, D.D., 2004. Applications of digital image correlation to biological tissues. Journal for Biomedical Optics 9, 691–699.

Zhao, R., Simmons, C.A., 2012. An improved texture correlation algorithm to measure substrate-cytoskeletal network strain transfer under large compressive strain. Journal of Biomechanics 45, 76–82.

Zhu, C., Bao, G., Wang, N., 2000. Cell mechanics: mechanical response, cell adhesion, and molecular deformation. Annual Review of Biomedical Engineering 2, 189–226.

Direct Measurement of Intranuclear Strain Distributions and RNA Synthesis in Single Cells Embedded within Native Tissue

Jonathan T. Henderson,[†] Garrett Shannon,[†] Alexander I. Veress,[‡] and Corey P. Neu[†*]
[†]Weldon School of Biomedical Engineering, Purdue University, West Lafayette, Indiana; and [‡]Department of Mechanical Engineering, University of Washington, Seattle, Washington

ABSTRACT Nuclear structure and mechanics play a critical role in diverse cellular functions, such as organizing direct access of chromatin to transcriptional regulators. Here, we use a new, to our knowledge, hybrid method, based on microscopy and hyperelastic warping, to determine three-dimensional strain distributions inside the nuclei of single living cells embedded within their native extracellular matrix. During physiologically relevant mechanical loading to tissue samples, strain was transferred to individual nuclei, resulting in submicron distributions of displacements, with compressive and tensile strain patterns approaching a fivefold magnitude increase in some locations compared to tissue-scale stimuli. Moreover, nascent RNA synthesis was observed in the interchromatin regions of the cells studied and spatially corresponded to strain patterns. Our ability to measure large strains in the interchromatin space, which reveals that movement of chromatin in the nucleus may not be due to random or biochemical mechanisms alone, but may result from the transfer of mechanical force applied at a distant tissue surface.

INTRODUCTION

The nucleus is a membrane-bound organelle and regulation center for gene expression in the cell (1). The position of a gene in the interior of the nucleus changes when it becomes highly expressed, and is often found to extend out of its chromosome territory into the interchromatin space (2). The accessibility of DNA regions by transcription factors may be driven by a variety of mechanisms, including diffusive or thermal conformational changes (3,4), or through biochemical processes (5), which affects the chromatin structure and the complex local binding affinities of the chromatin and RNA molecules surrounding a gene. Less clear is the role of mechanical force transfer as a directed movement mechanism for DNA accessibility, due perhaps to the technical challenges in measuring small-scale mechanics inside the nuclei of cells embedded in their native extracellular environment.

Mechanical forces transfer to the nucleus directly and indirectly through specific cellular pathways and cytoskeletal structures (6,7). There is increasing evidence that mechanical forces are transferred to the nucleus to orchestrate transcriptional activity (8). Protein dynamics inside the nucleus are additionally important for maintaining the nuclear structure and in facilitating gene expression at the transcription level (9). Probing spatiotemporal relationships between distributed mechanical forces and localized gene expression (i.e., biophysical and biochemical interactions) in the nuclei of individual cells is necessary because the individual cells experience different mechanical stimuli resulting from variations in local cell and extracellular matrix interactions. Studies that provide average measures over cells in a given tissue would oversimplify the heterogeneity intrinsic to the population. To understand the inherent variability of large cell populations, innovative methods are therefore required for combined measurements of single nuclei biophysical and biochemical interactions in cells maintained in their three-dimensional (3D) extracellular matrix microenvironment.

Current methods used to simultaneously probe biophysical or biochemical interactions in small subcellular structures like the nucleus are lacking. Methods to characterize nuclear mechanics typically study isolated cells or cells embedded in 3D gel matrices, and often report aspect ratio and volume change measures (10–12) that do not easily reveal the inherent complexity of internal strain patterns. Additionally, such methods lack the spatial resolution necessary for the correlation of intranuclear biomechanics and simultaneous internal biochemical activity. Recent approaches to link nuclear mechanics to biochemical responses have explored unique microscopy-based experimental designs, including the use of photobleaching and fluorescence resonance energy transfer pairs (13,14).

We simulated physiologically -relevant shear loading to tissues while simultaneously measuring nuclear mechanics and nascent RNA synthesis. Applied dynamic or static tissue shear loading mimics routine activities of cartilage-to-cartilage contact in the body that may be seen during walking or standing activities. Here, we describe detailed patterns of intranuclear strains and newly synthesized RNA in the nuclei of single cells in situ during tissue-scale loading. The use of a new, to our knowledge, hybrid imaging technique enabled us to measure biomechanical and biochemical activity in the nuclei of single cells, and contributes to our understanding of whether mechanical force applied directly to tissue surface transfers to the nuclei of embedded cells to possibly influence gene expression.

Submitted March 27, 2013, and accepted for publication September 26, 2013.

*Correspondence: cpneu@purdue.edu

Editor: Andrew McCulloch.

0006-3495/13/11/2252/10 $2.00

http://dx.doi.org/10.1016/j.bpj.2013.09.054

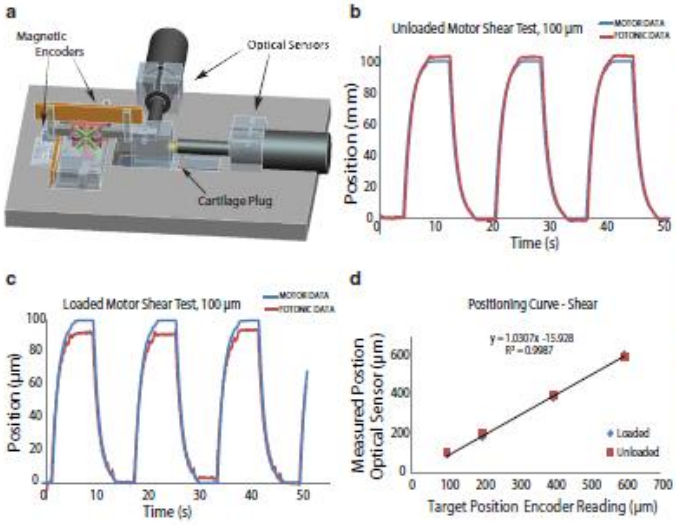

FIGURE 2 The tissue deformation system was validated using a fiber optic displacement measurement system. Motion was provided by two magnetic linear encoders (Nanos Instruments) mounted on Piezo LEGS LL1011A motors (Micromo; Clearwater, FL), and verified using a MTI-2000 Fotonic Sensor (MTI Instruments; Albany, NY). (*a*) CAD representation of the loading device with encoders as well as optical sensor in their respective positions. (*b*) Plot of a representative square-wave (100 μm) displacement profile in control experiments (i.e., actuator motion without a sample present). There was a small, micronscale offset between the encoder positioning and the Fotonic Sensor readout. (*c*) Plot of a square-wave (100 μm) displacement profile with a sample present. (*d*) Three square wave cycles at each position were averaged to produce the linear calibration curve loading a sample (*diamonds*) and without a sample (*squares*). To see this figure in color, go online.

element mesh was created from the confocal images depicting DNA, and a hyperelastic warping algorithm (nike3d) was used to calculate displacement and strain patterns throughout the nuclear volume (Figs. 1 and 4) (17,18). The algorithm deformed a 3D mesh of the *z*-stack image of the nucleus in the reference configuration until it matched the target image of the nucleus in a deformed configuration based upon the minimization of the differences in image intensities between the reference image and the deformed image (19,20). Nodal displacements were used to compute finite Lagrangian 3D strain fields, and principal strains and directions.

Validation: measurement of error in displacement fields using simulations

To validate our hybrid method, in particular the use of hyperelastic warping to quantify strain fields in the interior of small nuclear structures, and to determine the error associated with the hybrid technique overall, we used extensive forward finite element simulations. A 3D mesh was created from the *z*-stack images of a nucleus that was deformed in a finite element simulation with known displacement and strain magnitudes representative of those observed in the nuclei of living cells. A deformed image data set was created based upon the displacements of the forward finite element model. These images were analyzed using hyperelastic warping, and additionally, data were also directly compared to well-known (conventional) texture correlation techniques. Forward finite element stimulations were used to create a known displacement field and determine error (quantified in terms of root mean-square error (RMSE), bias, and precision) of the hyperelastic warping and texture correlation techniques. The forward simulation generated a known 3D displacement field and images of the deformed nucleus that was representative of experimental data. Gaussian noise was added to the image sets to vary the signal-to-noise (SNR) and contrast-to-noise (CNR) ratios to span the range of experimentally observed values. In-plane (*x* and *y* displacement) comparisons between the techniques were made in image slices through the center and at the edge of the image volume. Differences between calculated and known displacements were used to estimate the average RMSE, bias, and precision, over the range of simulated SNR and CNR ratios.

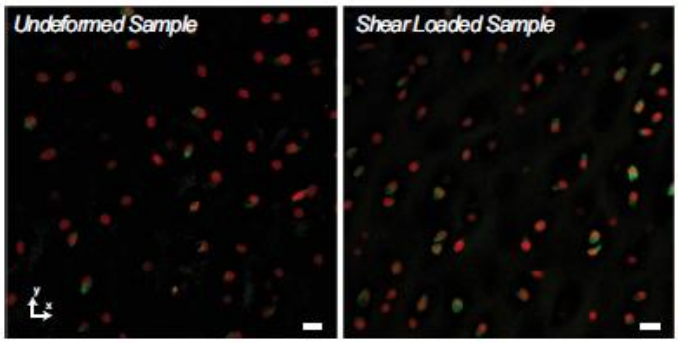

FIGURE 3 Control (*nondeformed*) tissue explants exhibited a reduce number of cells with nascent RNA expression compared to explants exposed to mechanical shear. The images shown are *z* projections of 20 *z*-slices, and the nascent RNA (*green channel*) was filtered to eliminate uneven background intensities so that a threshold could be applied to facilitate cell counting. The image postprocessing was performed with ImageJ (NIH, Bethesda, MD). The control sample showed 14 out of 54 cells (26%) with nascent RNA expression, whereas mechanical shear of the deformed (*treated*) sample resulted in 44 out of 75 (59%) cells with nascent RNA expression. Nuclei in Figs. 4 and 7–9 were analyzed from this deformed image field of view (Scale bar = 10 μm). To see this figure in color, go online.

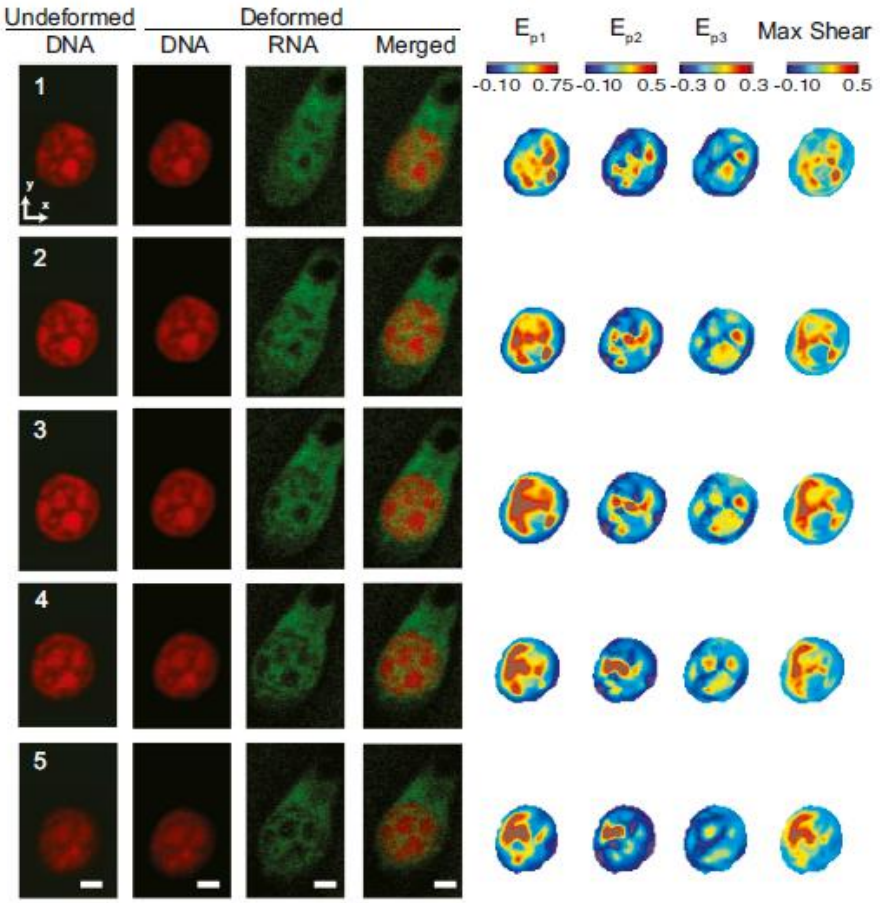

FIGURE 4 Intranuclear strain patterns in a single cell are spatially complex in three dimensions and heterogeneous even during simple shear at the tissue surface. (*a*) Five *z*-slices from an undeformed and deformed nucleus showing nascent RNA and the merged DNA-RNA image. Spatial patterns of strain, and DNA and nascent RNA images, vary by slice location. (*b*) However, overlaid graphs (Fig. 8) show that the relationship between strains and RNA or DNA intensity had very little variation between slices. (Scale bars = 2 μm) To see this figure in color, go online.

Nascent RNA synthesis in situ

A Click-iT RNA Alexa Fluor 488 Imaging Kit (Invitrogen) was used to tag and image newly synthesized RNA over a 60 min period of deformation (Fig. 1 *b*). Nascent RNA detection was performed by a click chemistry reaction between an RNA incorporated 5-ethynyl uridine tag and an azide-containing dye after cell fixation and permeabilization (21,22). Briefly, after incubation during loading, the samples were fixed with 2% formaldehyde in PBS, permeabilized with 0.1% Triton X-100 in PBS, and exposed to freshly prepared Click-iT reaction cocktail, while still in the loading apparatus.

To image nascent RNA synthesis in situ, two preliminary studies were additionally performed to successfully translate the RNA detection technology from its developed use in monolayer cells (21,22) into a 3D tissue environment. First, we minimized the background autofluorescence of collagen and the nonspecific binding of the fluorescent tag. We selected an appropriate emissions range on the confocal detector to minimize signal from collagen, and in addition we applied an image enhancing blocking reagent (Image-iT FX Signal Enhancer, Invitrogen) to help minimize nonspecific binding (Fig. 3). To remove nonspecific background staining in our studies, a 60 min incubation of the blocking reagent was used before the final image acquisition. Second, we determined the duration of 5-ethynyl uridine incubation to enhance RNA signal detection following mechanical shear loading. It should be noted that excessive incubation times resulted in an observed RNA signal from the combined effects of shear deformation and routine (e.g., housekeeping) cellular RNA synthesis (21). Using time duration studies, we determined that routine RNA synthesis was detected above background fluorescence levels in the cells of tissues that were unloaded and incubated for 60 min, indicating a time duration that could be used to best detect RNA signal enhancement due to mechanical loading. To further control for sample variation in routine RNA synthesis, one half of the tissue explant (i.e., one half of the hemicylinder) was loaded, whereas the second half was used as the unloaded control (Fig. 3).

Relationship between intranuclear strains and newly synthesized RNA

To explore links between the internal nuclear mechanics and newly synthesized RNA, the intranuclear strain fields were spatially compared qualitatively and using quantitative correlation analyses with custom MATLAB code (The MathWorks, Natick, MA). Correlation measures were made at three levels, i.e., within a given image slice through a single nucleus, within an image volume representing a whole single nucleus, or among nuclei from single cells identified in the field of view of the confocal images. The raw data consisted of strain values that were correlated to the image (DNA or RNA) intensity values at each voxel location of the nucleus. To facilitate correlations between strain and RNA or DNA image intensities, the data were binned according to the image intensity (bin size = 0.02). The data were binned for each image slice, and the binned results were additionally averaged for a single slice and averaged z-stacks. Correlation statistics (e.g., r^2 values) were calculated from the binned data sets.

RESULTS

Hybrid microscopy reveals complex intranuclear displacements and strains

Intranuclear deformation, defined by displacements and strains, were found to be heterogeneous and complex in living cells embedded within their native extracellular matrix. Intranuclear strains were both amplified and attenuated compared to tissue-scale stimuli. During a 15% simple shear strain, intranuclear displacements overall were consistently submicron in magnitude, with differences approaching only 10 s of nanometers depending on the size and location of the regions used for comparison (Fig. 5). Strong displacement gradients resulted in large intranuclear strains, typically <75% in magnitude, depending on location in the nucleus (Fig. 4). In contrast, nuclei in nonloaded control cartilage showed minimal intranuclear strain compared to those from loaded cartilage (Fig. S2).

The hybrid of microscopy and hyperelastic warping quantified heterogeneous and complex intranuclear strain with minimal error. Of importance, the x and y displacement fields for the middle slice of the nucleus showed that hyperelastic warping matched more closely to the known (simulated) displacements compared to conventional (1st order) texture correlation algorithms (Fig. 5). The known displacements were related to the displacements measured by hyperelastic warping (slope = 1.11, $r^2 = 0.958$) and texture correlation (slope = 0.97, $r^2 = 0.477$). Hyperelastic warping and texture correlation were also compared using experimental data of a nucleus in undeformed and deformed states (Fig. 5 *b*). A comparison of warping and texture correlation displacement predictions with those of the forward model indicated similar qualitative displacement distributions. However, the texture correlation results were lower in magnitude than the hyperelastic warping results. We further noted that texture correlation displacement fields were biased by the bright areas in the image and around the nucleus perimeter, which was qualitatively observed in the known and experimental displacement fields (Fig. 5).

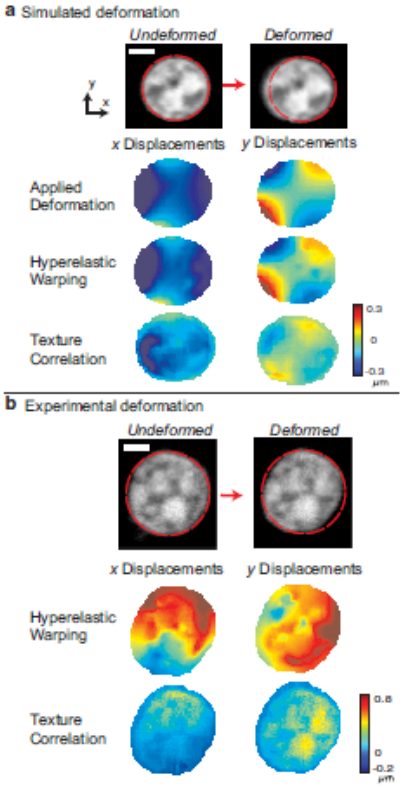

FIGURE 5 Displacement fields from hyperelastic warping, but not texture correlation, match known simulations, thus enabling the measurement of small-scale motion in individual nuclei. (*a*) A simulated deformation was applied to a 3D nucleus, with the middle z-slice images shown. The x and y displacement fields are shown for the known applied deformations, followed by the measured results from hyperelastic warping and texture correlation. (*b*) The x and y displacement fields from experimental data of a representative nucleus are shown for hyperelastic warping and texture correlation methods. Hyperelastic warping describes deformation with lower bias and increased precision compared to texture correlation (Fig. 6). (Scale bars = 2 μm) To see this figure in color, go online.

Hyperelastic warping consistently resulted in displacement data with lower error (avg. RMSE = 0.017) compared to texture correlation (avg. RMSE = 0.091), and without sensitive dependences on SNR and CNR ratios (Fig. 6).

Interchromatin regions and nascent RNA synthesis

Nascent RNA synthesis was observed in the interchromatin regions within nuclei of single cells embedded in their native extracellular matrix during shear loading at the tissue scale. For the nucleus depicted in Figs. 7 and 8, changes in

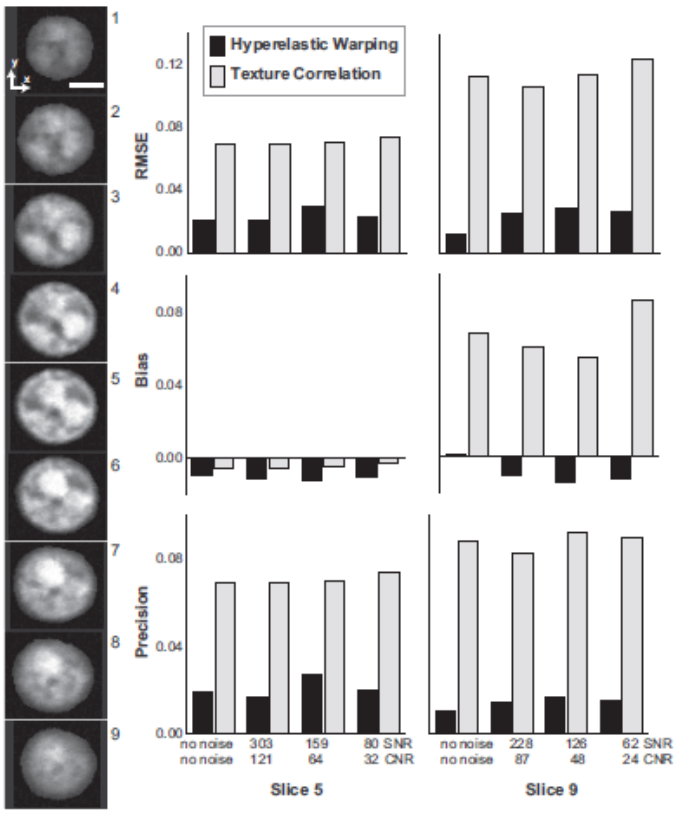

FIGURE 6 Hyperelastic warping consistently provided data with low RMSE and bias, and high precision, compared to texture correlation. SNR and CNR were calculated for each image set after the addition of Gaussian (*random*) image noise. Three error measurements (RMSE, bias, and precision) were used for comparison between the two techniques. The most noticeable difference between the techniques was the increase in bias seen with texture correlation between slice 5 and 9. The other measurements of error show similar performance of the techniques on each image slice. (Scale bar = 2 μm) To see this figure in color, go online.

chromatin position, defined in terms of strain, were also found to correspond to regions of nascent RNA synthesis. Magnitudes of principal strains and maximum shear strains approached a fivefold tensile increase over the 15% simple shear strain magnitude applied at the tissue surface in some regions of the nucleus. Different regions within the nucleus exhibited compressive or tensile strains, indicating that the magnitude of the applied shear at the tissue surface was amplified and attenuated depending on the internal region of the nucleus under investigation (Fig. 7). Principal directions for E_{p2} and E_{p3} were predominately in the imaging plane (i.e., in the *xy* plane), whereas E_{p1} directions were largely through-plane. Qualitative comparisons of the strain patterns revealed a correspondence between high tensile strain regions with increased intensities of the RNA and DNA patterns for max shear (RNA) and E_{p3} (DNA), respectively. Strain patterns tended to correspond visually to observed DNA and RNA patterns, suggesting that specific stimuli, e.g., localized maximum strain, may cause changes in the chromatin structure to influence newly synthesized RNA in nuclear regions with low DNA content.

Relationships between DNA, RNA, and strain were quantified at multiple levels, i.e., within a given image slice through a single nucleus (e.g., Fig. 7), within an image volume representing a whole single nucleus (e.g., Fig. 8), or among nuclei from many single cells (e.g., Fig. 9). For the single image slice in Fig. 7, significant correlations ($p < 0.007$) were found between DNA intensities and E_{p1} ($r^2 = 0.238$), E_{p2} ($r^2 = 0.506$), and E_{p3} ($r^2 = 0.833$), but not max shear ($r^2 = 0.000$; $p = 0.984$). Significant correlations ($p < 0.001$) were also found between RNA intensities and E_{p1} ($r^2 = 0.617$), E_{p3} ($r^2 = 0.754$), and max shear ($r^2 = 0.827$), but not E_{p2} ($r^2 = 0.214$; $p = 0.096$). Similar correlations were observed for a whole single nucleus (Fig. 8), after pooling r^2 values from each slice of the image volume, with DNA and RNA related to E_{p1} ($r^2 = 0.543$, $r^2 = 0.668$), E_{p2} ($r^2 = 0.677$, $r^2 = 0.471$), E_{p3} ($r^2 = 0.889$, $r^2 = 0.473$), and max shear ($r^2 = 0.192$, $r^2 = 0.694$), respectively.

Relationships between strains and DNA and RNA intensities varied among the cell nuclei studied (Fig. 9). Nascent RNA synthesis was consistently observed in the interchromatin regions, although specific intranuclear statistical

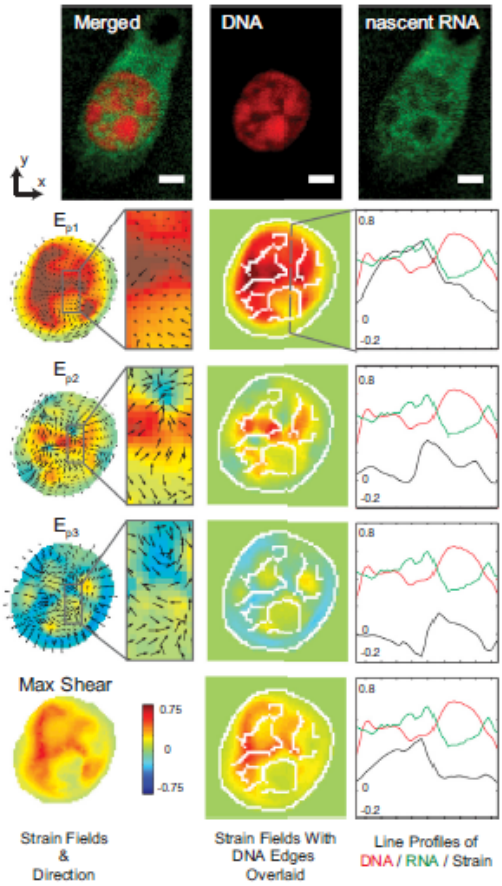

FIGURE 7 Principal strain magnitudes and directions correspond to the intensity of DNA and nascent RNA. A magnification box highlights a nuclear region with heterogeneous (amplified and attenuated) strains. The strain direction for E_{p1} was predominantly through the imaging plane, whereas the $E_{p2,3}$ directions were largely in the imaging plane. Although only one representative image slice from the middle of the nucleus is shown, the results were consistent in other z-slices (Figs. 4 and 8). A single line scan at the right of the strain maps depicts the cross-sectional profiles for DNA (*red*), RNA (*green*), and strain magnitudes (*black*). White lines of the strain map are edges of the DNA image intensity calculated by an edge detection function in MATLAB to help spatially visualize the high and low DNA regions. (Scale bars = 2 μm) To see this figure in color, go online.

correlations covered a broader range when compared cell to cell. Significant statistical correlations ($p < 0.015$) were found in all cells studied between DNA intensities and E_{p1} ($r^2 = 0.575$) and E_{p2} ($r^2 = 0.735$), and between RNA intensities and E_{p3} ($r^2 = 0.641$), with aforementioned coefficients of determination pooled over all nuclei shown in Fig. 9. Statistical correlations varied among cells between DNA intensities and E_{p3} ($r^2 = 0.550$, $p < 0.443$) and max shear ($r^2 = 0.575$, $p < 0.306$), and between RNA intensities and E_{p1} ($r^2 = 0.357$, $p < 0.379$), E_{p2} ($r^2 = 0.492$, $p < 0.295$), and max shear ($r^2 = 0.374$, $p < 0.954$), with 6 of 20 total possible correlations (i.e., five relationships for the four cells shown in Fig. 9) not significant ($p > 0.040$).

DISCUSSION

Diffusive or biochemical processes are thought to drive the movement of genes to different regions of the nucleus, perhaps due to changes in binding affinities in addition to conformational alterations in the chromatin structure. Additional studies, involving the use of relatively insensitive methods based on texture correlation, indicate that the deformation in the nucleus is minimal compared to cell and extracellular matrix strains (23). These studies imply that the relative stiffness of the nucleus is high compared to surrounding cellular structures, resulting in minimal internal deformation for a given applied load. The concept of a relatively stiff nucleus would indirectly support the idea that specific (e.g., diffusive) mechanisms alone may drive gene expression, because the nucleus interior would be more isolated from physical deformation occurring in the extranuclear regions, and would require alternative mechanisms for transcription and other regulators to access DNA.

Here, we find that movement of the nuclear structures, quantified by strain, is highly heterogeneous and is both amplified and attenuated during even simple mechanical loading at the tissue scale. Given a reasonable compliance of chromatin, the heterogeneous strains would be expected to shift and reposition the relative internal position of genes, thereby altering the dynamics of regulation. Interestingly, the compliance of individual chromatin fibers has also been noted as a possible physical basis for DNA accessibility (24). However, we do not yet know the extent that either chromatin remodeling, or passive chromatin deformation in response to the applied load, explains the intranuclear strain patterns described. In light of this current limitation, and in contrast to single molecule studies conducted in controlled in vitro experiments, we overcame technical challenges in obtaining measurements within the nuclei of cells embedded in extracellular matrix in situ. The experimental setup and hybrid microscopy technique allowed us to propagate realistic and physiologically relevant mechanical forces through native structures to better quantify the extent that strain transfer may directly influence nuclear mechanics. The hybrid method, based on microscopy and hyperelastic warping, allowed the measurement of internal deformation (displacements and strains) in small nuclear structures at high spatial resolutions, limited most by the time constraints of image acquisition. Interestingly, the simultaneous detection of newly synthesized RNAs reveal localized expression corresponding to mechanical loading

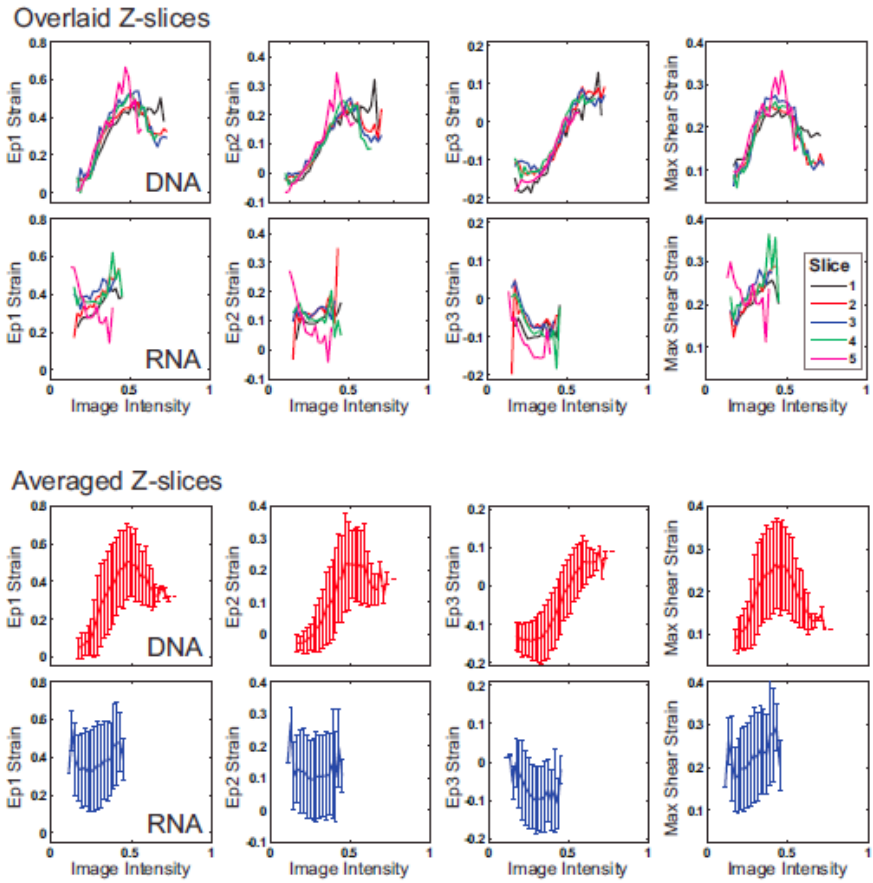

FIGURE 8 Complete 3D, DNA, and RNA image intensity to strain relationship analysis for a single nucleus from Fig. 4. The top graphs show the image intensity versus strain results for each z-slice and the bottom graphs are the averaged results. To see this figure in color, go online.

and patterns of principal and shear strains. The measurement of large (e.g., shear) strains in the interchromatin space that spatially correspond to the localization of nascent RNA expression supports the hypothesis that localized movement of chromatin in the nucleus may not be due to random or biochemical mechanisms alone, but instead can occur simply as a result of mechanical force transfer applied at a distant tissue surface. However, significant transport of RNA over the incubation time (e.g., Fig. 1) indicates that the nascent RNAs observed may not be a true response of the nucleus to deformation. Additionally, RNA expression was observed in nucleus regions that were expected to be more naturally transcriptionally active. Nevertheless, these regions corresponded with unexpectedly high levels of strain, suggesting that the nucleus structure may be routinely regulated through a variety of casual physical activities that involve tissue loading, which in turn allow for transcriptional and other regulators of biological activity and gene expression.

Our experimental analysis demonstrated the hierarchical transfer of strain over large distances and log scales from the tissue surface to the interior of individual nuclei in situ. In our study, simple shear strain applied at a distant tissue surface transfer to individual nuclei, amplifying strain up to fivefold in localized nuclear regions. Interestingly, we note reports of novel quantitative approaches to measure detailed internal biomechanics in individual cells, but these techniques largely ignore the intranuclear strain and gene expression (12). Quantification of intranuclear strains is important, because they possibly extend the concept of

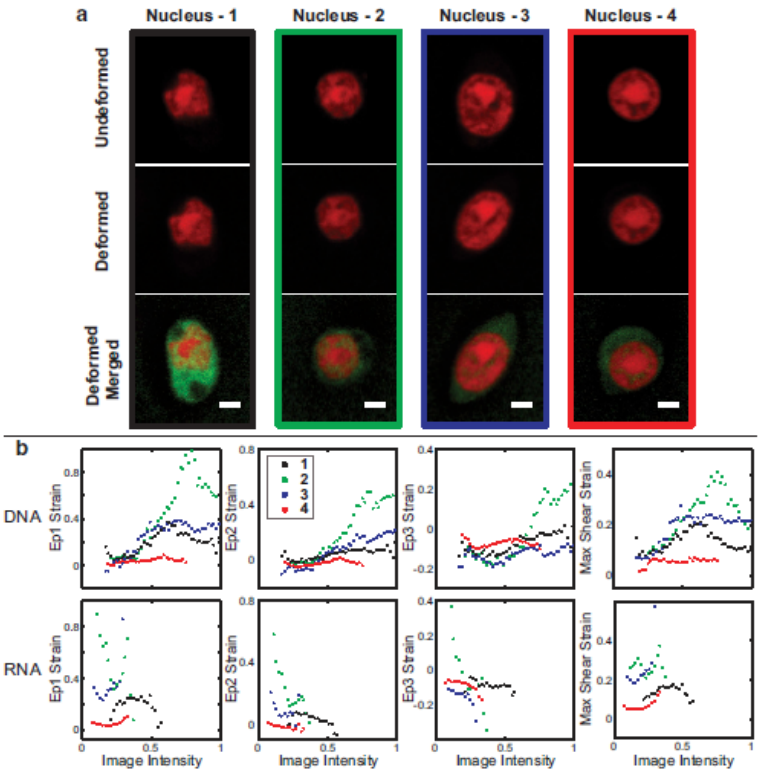

FIGURE 9 Strain magnitudes and nascent RNA expressions in nuclei vary among single cells within in a tissue volume subjected to uniform shear. (*a*) The undeformed DNA image, deformed DNA, and merged DNA-RNA images are shown for four cells from the same imaging field of view seen in Fig. 3. The nuclei were from the same region in the tissue, although there were several physical characteristics, such as shape, size, and long-axis orientation that may influence how the strain was transferred from the tissue to the nucleus. (*b*) The average image intensity versus strain for the four nuclei were graphed in matching colors as boxed in (*a*). Three of the four nuclei (excluding nucleus two) exhibited similar trends in DNA and RNA intensity patterns. The RNA graphs also show that there were different RNA image intensities between nuclei, which were qualitatively observed in panel (*a*). (Scale bars = 2 μm) To see this figure in color, go online.

nuclear mechanics arising due to physical links to the cytoskeleton or extracellular matrix (6,7), to also include remote links through pericellular and extracellular molecules, e.g., type VI and type II collagens, respectively, in the hierarchical organization of complex tissues like cartilage. Using the hybrid method, we did not yet in the current configuration tease apart the relative influence of load transfer through solid or fluid phases (25), or specify candidate matrix or cytoskeletal molecules that result in strain transfer. However, candidate molecules may be identified and visualized by fluorescent tagging in subsequent studies. In this work, it is important to emphasize the nondestructive nature of the hybrid technique, coupled with the ability to reveal internal spatiotemporal dynamics in living cell nuclei in situ for the first time, which enables the study of diverse cell-laden materials, including hydrogel or polymer constructs, and diseased tissues, that contain unique or rare cell populations.

The nucleus-to-nucleus variation of intranuclear strain field patterns (Figs. 4, 8, and 9) suggested that the applied tissue load was not uniformly transferred to every nucleus, possibly due to the spatially heterogeneous mechanics of cartilage explants that arise from cell location and spatial density in the tissue (26). This observation indicates the possibility of subtle and variable underlying cell-matrix connections or other structural parameters that dictate how load is shared over hierarchical scales. Interestingly, newly synthesized RNA was also observed outside of the nuclear region of the cell, illustrating transport during the short incubation time, which has also been reported in other cell types following treatments with soluble factors (21,22). Furthermore, we observe that the time-dependent response of the individual nuclei varies among nuclei to the applied shear (Fig. S3), suggesting more complicated (e.g., viscoelastic) mechanisms may play a role in the biomechanics and RNA expression in some cells. For example, the arrangement of structural elements in the microenvironment, and the local composition of extracellular and pericellular molecules (e.g., proteoglycans), influence the rate of force transmission to the cell, and were not measured in this study. Variations in cell shape and orientation were observed, suggesting that variations in other physical structures were present as well. Moreover, the cartilage may not yet have achieved a mechanical equilibrium, with time-dependent changes in interstitial fluid pressure and flow, in combination with constituents in the local microenvironment, possibly influencing strain patterns observed. Strain maps measured from DNA images taken at 10 min and 60 min postdeformation indicated an increase, decrease, or no change in the intranuclear strain patterns and magnitudes between the two time points. In contrast, very small

differences in aspect ratios of nuclei between 10 and 60 min indicate little to no bulk deformation of the nucleus between the two time points (Fig. S3).

CONCLUSION

These data suggest that cells in situ can sense an applied load that is transferred over relatively large distances and log scales to alter intranuclear deformation and to possibly directly influence new RNA synthesis, and may regulate other actions as well, including the transport of mRNA or other molecules through nuclear pores. The direct correspondence of strain and DNA or RNA patterns may suggest specific mechanical stimuli, e.g., shear strain, that influence spatially localized gene expression in individual cells, although it remains to be determined the extent that mechanics directly regulate nuclear mechanobiology in larger cell populations. We expect that this hybrid method, based on microscopy and hyperelastic warping, will enable a wide variety of future investigations into mechanotransduction mechanisms, including transcription of specific RNAs, and translation and control of downstream protein synthesis.

SUPPORTING MATERIAL

Three figures are available at http://www.biophysj.org/biophysj/supplemental/S0006-3495(13)01133-8.

The manuscript benefitted from helpful comments from Tyler Novak, Deva Chan, Sarah Calve, Russell Main, and Eric Nauman.

The authors gratefully acknowledge funding from the Andrews Fellowship (J.T.H.).

REFERENCES

1. Misteli, T. 2001. Protein dynamics: implications for nuclear architecture and gene expression. *Science*. 291:843–847.
2. Cremer, T., M. Cremer, …, S. Fakan. 2006. Chromosome territories—a functional nuclear landscape. *Curr. Opin. Cell Biol.* 18:307–316.
3. Felsenfeld, G. 1996. Chromatin unfolds. *Cell*. 86:13–19.
4. Polach, K. J., and J. Widom. 1996. A model for the cooperative binding of eukaryotic regulatory proteins to nucleosomal target sites. *J. Mol. Biol.* 258:800–812.
5. Cairns, B. R. 2007. Chromatin remodeling: insights and intrigue from single-molecule studies. *Nat. Struct. Mol. Biol.* 14:989–996.
6. Wang, N., J. P. Butler, and D. E. Ingber. 1993. Mechanotransduction across the cell surface and through the cytoskeleton. *Science*. 260:1124–1127.
7. Wang, N., J. D. Tytell, and D. E. Ingber. 2009. Mechanotransduction at
9. Cardoso, M. C., K. Schneider, …, H. Leonhardt. 2012. Structure, function and dynamics of nuclear subcompartments. *Curr. Opin. Cell Biol.* 24:79–85.
10. Guilak, F. 1995. Compression-induced changes in the shape and volume of the chondrocyte nucleus. *J. Biomech.* 28:1529–1541.
11. Knight, M. M., J. van de Breevaart Bravenboer, …, D. L. Bader. 2002. Cell and nucleus deformation in compressed chondrocyte-alginate constructs: temporal changes and calculation of cell modulus. *Biochim. Biophys. Acta*. 1570:1–8.
12. Legant, W. R., J. S. Miller, …, C. S. Chen. 2010. Measurement of mechanical tractions exerted by cells in three-dimensional matrices. *Nat. Methods*. 7:969–971.
13. Iyer, K. V., S. Pulford, …, G. V. Shivashankar. 2012. Mechanical activation of cells induces chromatin remodeling preceding MKL nuclear transport. *Biophys. J.* 103:1416–1428.
14. Ouyang, M., J. Sun, …, Y. Wang. 2008. Determination of hierarchical relationship of Src and Rac at subcellular locations with FRET biosensors. *Proceedings of the National Academy of Sciences of the United States of America*. 105:14353–14358.
15. Chan, D. D., and C. P. Neu. 2012. Transient and microscale deformations and strains measured under exogenous loading by noninvasive magnetic resonance. *PLoS ONE*. 7:e33463.
16. Neu, C. P., A. H. Reddi, …, P. E. Di Cesare. 2010. Increased friction coefficient and superficial zone protein expression in patients with advanced osteoarthritis. *Arthritis Rheum.* 62:2680–2687.
17. Phatak, N. S., Q. Sun, …, J. A. Weiss. 2007. Noninvasive determination of ligament strain with deformable image registration. *Ann. Biomed. Eng.* 35:1175–1187.
18. Veress, A., N. Phatak, and J. Weiss. 2005. Deformable image registration with hyperelastic warping. *In* Handbook of Biomedical Image Analysis Volume III: Registration Models. J. Suri, D. Willson, and S. Laxminarayan, editors. Kluwer Academic/Plenum Publishers, New York, Boston, Dordrecht, London, Moscow, pp. 487–533.
19. Veress, A. I., J. A. Weiss, …, R. D. Rabbitt. 2002. Strain measurement in coronary arteries using intravascular ultrasound and deformable images. *J. Biomech. Eng.* 124:734–741.
20. Veress, A. I., J. A. Weiss, …, G. T. Gullberg. 2008. Measuring regional changes in the diastolic deformation of the left ventricle of SHR rats using microPET technology and hyperelastic warping. *Ann. Biomed. Eng.* 36:1104–1117.
21. Jao, C. Y., and A. Salic. 2008. Exploring RNA transcription and turnover in vivo by using click chemistry. *Proceedings of the National Academy of Sciences of the United States of America*. 105:15779–15784.
22. Paredes, E., and S. R. Das. 2011. Click chemistry for rapid labeling and ligation of RNA. *ChemBioChem.* 12:125–131.
23. Gilchrist, C. L., S. W. Witvoet-Braam, …, L. A. Setton. 2007. Measurement of intracellular strain on deformable substrates with texture correlation. *J. Biomech.* 40:786–794.
24. Kruithof, M., F. T. Chien, …, J. van Noort. 2009. Single-molecule force spectroscopy reveals a highly compliant helical folding for the 30-nm chromatin fiber. *Nat. Struct. Mol. Biol.* 16:534–540.
25. Kim, E., F. Guilak, and M. A. Haider. 2008. The dynamic mechanical environment of the chondrocyte: a biphasic finite element model of cell-matrix interactions under cyclic compressive loading. *J. Biomech.*

33

Intranuclear Measurement of Deformation in Single Cells

Jonathan T. Henderson and Corey P. Neu

CONTENTS

Nuclear mechanics play a pivotal role in cell survival and gene expression. Mechanical stimulation of cells and nuclei regulates specific mechanotransduction pathways that aid in cell homeostasis. This chapter describes current and emerging methodologies that are used to study nuclear mechanics at the single cell level. We highlight a hybrid method based on optical microscopy and hyperelastic warping that was developed to measure intranuclear strain within individual nuclei maintained in cultured tissue explants. The combined use of imaging and postprocessing methods allows for the study of nuclear mechanics and mechanobiology in single cells, permits simultaneous study of newly synthesized RNAs, and overcomes limitations in competing factors like spatial and temporal resolution of acquisition systems. We discuss the implementation of methods to measure nuclear mechanics, as well as their potential to increase understanding of diseases involved in compromised nuclear structures.

33.1 Introduction

Diseases such as osteoarthritis, laminopathies, and specific cancers are shown to have compromised tissue, cellular, and nuclear mechanics, potentially interrupting normal mechanobiological processes and providing an origin point for disease progression.[1–3] Osteoarthritis of cartilage and articulating joints has a multifactorial etiology resulting in part from a homeostatic imbalance in the tissue. Cartilage degradation causes an altered micromechanical environment, increasing the expression of degrading enzymes that exacerbate the disease state.[4] Laminopathies specifically compromise the rigidity of the nuclear envelope and are linked to premature aging and muscular dystrophy. Cancer cells actively alter their nuclear stiffness, facilitating cell mobility and metastasis,[3,5] and pluripotent cells alter their nuclear structure and stiffness prior to cell lineage commitment.[6] To better understand healthy and diseased or damaged tissues, and how mechanical forces applied to tissues and cells influence individual cell nuclei, it is important to measure the mechanics (e.g., strain) in the nucleus and quantify how nuclear mechanics regulate gene expression.

The nucleus is largely occupied by chromatin, dynamic structures that are influenced by diverse chemical and mechanical signals.[7,8] Chromatin itself is a hierarchical structure composed of DNA molecules wrapped around histones to form nucleosomes, which are then further packed together to form chromatin structures. Within the nucleus, chromatin is often classified as

TABLE 33.1
Common Techniques for Measurement of Nuclear Mechanics

Measurement Technique	Description	Spatial Resolution	Bulk or Local Measurement	Isolated or Embedded (2D/3D) Cells	References
Fluorescence anisotropy	Local compaction	High	Local	Isolated/2D	11–13
Aspect ratio	Morphological change	Low	Bulk	Isolated/2D/3D	14,15
Volume change	Morphological change	Low	Bulk	Isolated/2D/3D	16,17
Micropipette aspiration	Material properties	Medium	Bulk	Isolated	18,19
Nanoindentation	Material properties	High	Local (surface)	Isolated	20,21
Texture correlation	Nuclear strain	High	Local	Isolated/2D/3D	22,23
Hyperelastic warping	Intranuclear strain	High	Local	Isolated/2D/3D	24

heterochromatin, i.e., tightly packed structures that are thought to be areas of relatively silenced gene expression, or euchromatin, i.e., lower density structures that exhibit higher levels of gene expression. Gene expression is affected by nuclear receptors, secondary messengers, and other chemical signaling cascades triggered from chemical binding to cellular receptors. Recently, direct regulation of gene expression by mechanical force has been hypothesized to work in parallel with chemical signaling, with transcriptional activity and accessibility regulated through physical changes in DNA regions.[9,10]

Several methodologies have been developed to measure nuclear mechanics and help identify the role of the nuclear structure in the mechanoregulation of gene expression. Methods to measure nuclear mechanics are numerous and include fluorescence anisotropy, micropipette aspiration or nanoindentation, changes in nuclear aspect ratios and/or volume, and texture correlation or deformable image registration (Table 33.1). Understanding the strengths and limitations of each method better define their best applications for intended experimental needs and objectives. This chapter will cover different methodologies that are used to investigate nuclear mechanics, with special attention paid to the new implementation of deformable image registration using hyperelastic warping and concurrent quantification of nascent RNA expression in single cells.

33.2 Deformed Nucleus

33.2.1 Connecting the Nucleus to the Cell and Extracellular Matrix

The nucleus is a distinct structure inside the cell that is linked through cytoskeletal components to the extracellular matrix (ECM). Among different tissue and cell types, the structures connecting the nucleus to the extracellular environment can be very unique. In this chapter, we will largely focus on the primary cell type (chondrocyte) found in cartilage, a load-bearing tissue with significant relevance to human disease (e.g., osteoarthritis).[25,26] In the chondrocyte, there are multiple structural elements that connect the nucleus to the ECM (Figure 33.1). The cell is anchored to the ECM by cell membrane proteins (e.g., integrins and CD44), which bind to collagen and proteoglycans. These anchoring transmembrane proteins are associated with intracellular cytoskeletal components such as actin, intermediate filaments, and microtubules. The microtubules interact with the endoplasmic reticulum (ER), which is continuous with the outer nuclear membrane. The microtubules, along with other cytoskeleton components, are also connected to the nucleus through a group of nuclear transmembrane proteins called the linker of nucleoskeleton and cytoskeleton complex (LINC). These structural connections from the ECM to the nucleus provide a mechanism for stress and strain to directly transfer to the nucleus when applied at relatively distant tissue surfaces.

33.2.2 Nuclear Structures: Form and Function

Within the nucleus, there are many specific structural elements that help to regulate gene expression. DNA nucleotides that code for genes make up the majority of material in the nucleus. Nuclear function is regulated by transcription factors,[27] nuclear pores,[28] and the nucleolus,[29] about which the referenced reviews provide more in-depth detail. Within the nucleus, distinct euchromatin and heterochromatin regions are observed, in addition to the interchromatin space, where nuclear components are located, such as the nucleolus, which synthesizes rRNA.[29,30] Like a shell, the nuclear membrane is made up of a network of lamins that provide structural rigidity to the nucleus. Distributed in the nuclear membrane, nuclear pores regulate the transport of molecules in and

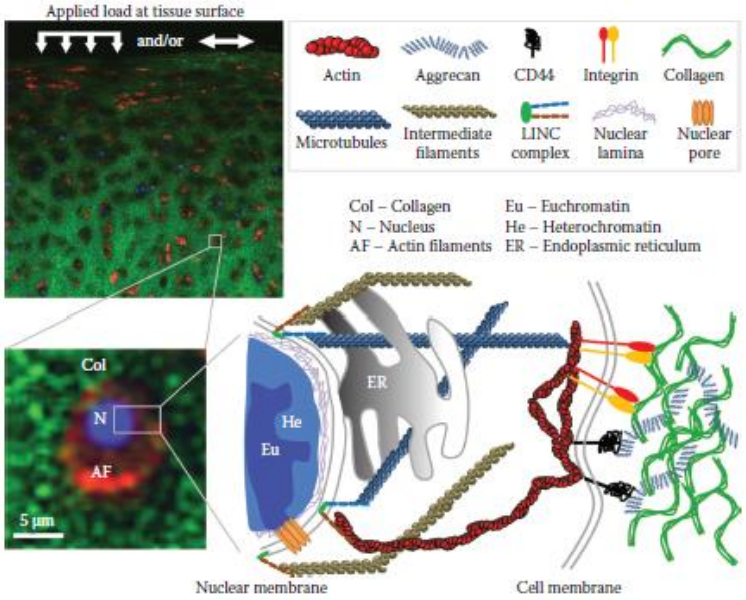

FIGURE 33.1
Structural components transfer strain from the tissue and ECM to the cell nucleus. Strain is transferred from an applied load (e.g., compression or shear) at the tissue surface to the cells and nuclei maintained alive within the interior. Articular cartilage is shown here as a model hierarchical system that normally undergoes many thousands of loading cycles during daily activities like walking. Multiple structural components, including surface receptors, cytoskeletal proteins, and the nuclear lamina, connect the ECM to the nucleus.

out of the nucleus (e.g., RNA; Figure 33.1). The integration of the nuclear components and global structures provides the biophysical conditions for the nucleus to maintain the integrity of the DNA and regulate cellular biosynthesis by modulating the shape, size, and internal patterns of deformation (e.g., displacements and strain).

Local mechanical deformations within the nucleus are thought to alter early transcriptional activities for gene expression. One proposed mechanism is that intranuclear mechanical deformation alters the structure of the chromatin domains thereby modulating the gene expression in the cell.[31]

33.3 Measuring Nuclear Mechanics and Mechanobiology

33.3.1 Nuclear Imaging, Deformation, and Measurement Techniques

Imaging of intranuclear mechanics in single cells is challenging. Several contemporary methods attempt to meet this need through the use of high-resolution imaging (e.g., superresolution microscopy, scanning electron microscopy), although visualization of cell and subcellular structural morphology does not necessarily provide information describing how these structures may deform under applied loading or during active cytoskeletal or chromatin remodeling. Typically, imaging involves visualization of chemically fixed cells, preventing an analysis of deformation and associated mechanotransduction activity. Widefield and confocal microscopy have visualized nuclei in living cells before and after applied deformations,[22] and methods have been used to mechanically deform the nuclei of isolated or tissue/matrix-embedded cells[32] (Table 33.1 and Figure 33.2). A commonality among the deformation and measurement techniques is that the nuclei are fluorescently imaged in predeformation and postdeformation states, so that motion in a current configuration can be measured from a reference configuration.

Considering the variety of methods available to measure nuclear mechanics (Table 33.1), we focus on three common ways to measure predeformation and postdeformation changes of the nucleus (Figures 33.2 and

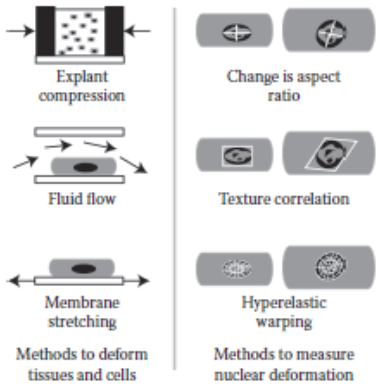

FIGURE 33.2
Common methods to measure mechanical deformation in the nucleus. Flow and stretch methods deform tissues and isolated cells in 2D (monolayer) or 3D (embedded) native or engineered microenvironments. Simple measures of nuclear shape and morphology changes are documented by changes in the aspect ratio. Texture correlation and hyperelastic warping methods provide details of internal strains with different levels of error as described in Figure 33.3.

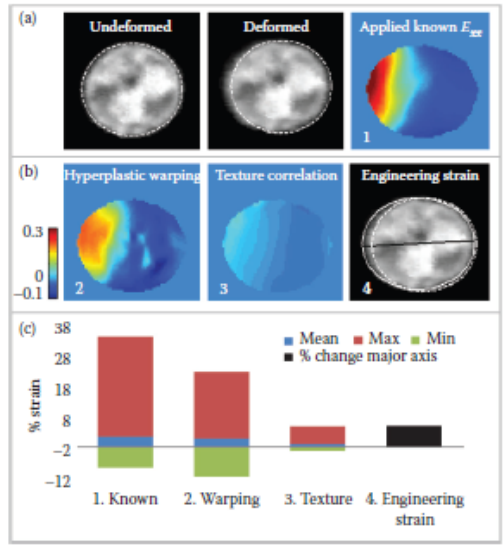

FIGURE 33.3
Simple comparison of three techniques to quantify nuclear deformation. A finite-element model was used to apply a known deformation (strain) to a nucleus and create the deformed nucleus from the undeformed z-stack images (a). Knowing the applied intranuclear strain (a.1), three measurement techniques, hyperelastic warping (b.2), texture correlation (b.3), and engineering strain in the direction of the major axis (b.4), were used to measure the strain fields for comparison between the techniques. Results from the hyperelastic warping method best described the known deformation, with decreased sensitivity observed from texture correlation and engineering strain measurements (c).

33.3), each with distinct strengths and weaknesses. First, changes in bulk morphology of the nucleus (e.g., aspect ratios, nuclear volume, or major/minor axes) enable an average mechanical response of nuclei after mechanical perturbation, often using automated or semiautomated algorithms. While bulk measurements can be acquired from large numbers of cells, important spatial information from within individual nuclei is not captured or described. Second, texture correlation measures intranuclear strain fields by tracking intrinsic high contrast regions, revealed by spatial distributions of fluorescent markers, in the images depicting undeformed and deformed nuclei.[22] Unfortunately, the small volume of the nucleus, coupled with large subset sizes required to help minimize error,[22] limits the ability to reliably quantify intranuclear strain. Third, deformable image registration (e.g. hyperelastic warping) permits intranuclear strain measurements by iteratively deforming a three-dimensional (3D) finite-element mesh representing the undeformed nucleus until it matches the deformed nucleus.[24] A 3D intranuclear strain field is calculated from the displaced nodes of the registered nuclear mesh.

Bulk morphology of the nucleus, texture correlation, and hyperelastic warping increasingly predict known nuclear deformations applied in simulations (Figure 33.3).

Compared to the known deformation applied, texture correlation underestimates the magnitude of the strain field, and the (bulk) engineering strain measured by changes in width fails to capture the strain distribution or magnitudes. In contrast, hyperelastic warping best approximated the known magnitude and spatial distribution of the applied known strain field, with decreased error (i.e., higher precision and minimal bias).[24]

33.3.2 Design Criteria to Combine Nuclear Mechanics and Mechanobiology

Limitations in the spatial and temporal resolution of image data, and the impact of these limitations on image quality (e.g., signal-to-noise ratio [SNR]), must be considered when designing techniques to study nuclear mechanics and mechanobiology in single cells. Tradeoffs in spatial and temporal resolutions may be accepted for specific applications, noting that the error of intranuclear deformation depends largely on the ability to track the motion of structures on the organelle interior with a sufficient SNR. Methods that analyze long-term responses ranging from minutes to days may provide insufficient temporal resolution to capture direct

relationships between nuclear structure and gene expression.[33–36] For example, to capture nuclear mechanics and mechanobiology in a single cell, the measurement technique needs to be fast enough to capture a possible rapid gene expression response to the applied load. The technique also needs to have a high enough spatial resolution to image the nuclear shape changes due to the applied load. Spatial resolution is often sacrificed to improve temporal resolution, and vice versa, when designing techniques for the study of single cells.[36]

33.4 Hybrid Technique—Microscopy and Hyperelastic Warping

A hybrid confocal and hyperelastic warping methodology has recently been demonstrated to measure and calculate intranuclear mechanics and biophysical activities.[24] Combining the high spatial resolution of optical (e.g., confocal or multiphoton) microscopy with hyperelastic warping to measure intranuclear strain maps has provided detailed intranuclear strains compared to bulk measurement of nuclear deformation (Table 33.1). Optical microscopy also enables imaging deep within tissues to calculate nuclear mechanics of cells maintained in native tissue cultures. Z-stack images capture the full volume of the nucleus in the undeformed and deformed state. The volume of the nucleus is converted into a finite-element mesh that is used in an iterative hyperelastic warping-based method, where the undeformed nuclear mesh is optimally warped until it matches the deformed nucleus, to measure 3D intranuclear deformations (Figure 33.4). The intranuclear strain map can be spatially and temporally compared to any fluorescent indicator of gene expression that can be imaged concurrently with the nuclei stain in a second imaging channel, such as nascent RNA synthesis (Figure 33.4).

33.4.1 Strain Transfer: Tissue to Nucleus

Strain transfer to the nucleus from an applied mechanical load at a distant tissue surface can be measured as amplification and attenuation in local subnuclear regions by microscopy and hyperelastic warping. When cartilage explants undergo shear loading, there is higher tissue strain in the superficial zone that diminishes in the deep zone[37] (Figure 33.5). Likewise, compressed cartilage explants influence nuclei more near the articulating surface (superficial zone) and progressively less in the middle and deep zones.[38] These bulk nuclear volumetric strain results demonstrate a depth-dependent strain transfer from the applied tissues strain to the cell.

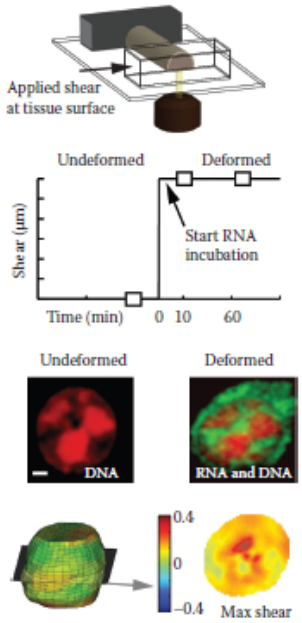

FIGURE 33.4
Experimental overview for methods to measure single-cell intranuclear mechanics and RNA synthesis. For articular cartilage, a tissue explant is created as a half cylinder from a cored osteochondral plug and placed in an electronically controlled deformation device that allows for single cells to be imaged within the deforming tissue using optical (e.g., confocal, multiphoton) microscopy. Immediately after shearing, newly synthesizing RNAs are labeled using a click chemistry-based incubation. The deformed nucleus is imaged at 10 min and then at the end of the incubation time (60 min), and the data are used for the measurement of intranuclear strain using hyperelastic warping. Images of the nucleus are taken from the center z-slice (red = DNA stain, green = RNA stain) (Scale bar = 1 μm).

However, more detailed intranuclear strains are resolved by using hyperelastic warping that shows amplification and attenuation of strain that the bulk measurement techniques do not reveal. The combined use of optical microscopy and hyperelastic warping provides a new method that gives 3D local nuclear deformations that were previously immeasurable by bulk measurement techniques.

33.4.2 Measuring Single-Cell 3D Intranuclear Time-Dependent Strain Fields

Single-cell intranuclear strain fields show complex strain patterns with time-varying magnitudes that are spatially correlated to DNA intensity. Confocal z-stack images of chondrocyte nuclei taken before and at 10 and

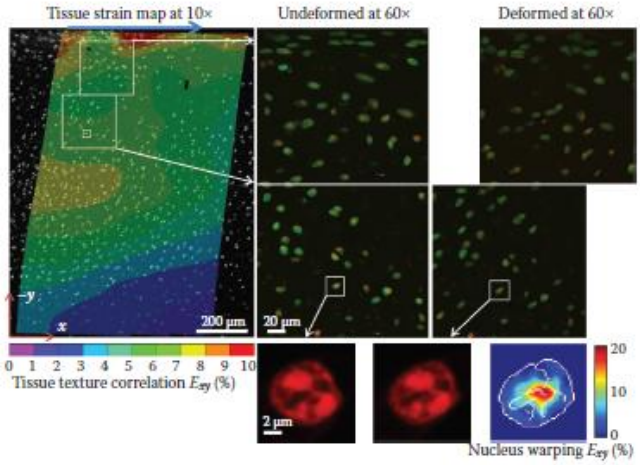

FIGURE 33.5
Strain transfer from the tissue surface to intranuclear regions. A shear load was applied at the articular cartilage surface (blue arrow), and texture correlation was used to measure the E_{xy} strain field for the tissue scale deformation (10× objective) using cells as fiducial markers. Hyperelastic warping was used to measure the strain fields of the nucleus highlighted by the smaller boxes in images acquired using 10× and 60× objectives. Depending on the intranuclear region, the measured tissue scale strain (5%–6%; i.e., tissue texture correlation E_{xy} [%] strain field) was amplified or attenuated when compared to the nucleus warping E_{xy} (%) strain field.

60 min after a shear load is applied to the articular surface of a cartilage explant show similar strain field patterns within a cell, although the magnitudes of the patterns at the two time points differ cell to cell.[24] The intranuclear strain field patterns are spatially complex, with brighter DNA intensity regions in specific cell populations studied typically corresponding to tensile strain regions. A current challenge remains to define mechanisms of strain transfer, including specific cytoskeletal elements responsible for load transmission *in situ*. Also, the role of directionally concentrated strains in the physical regulation of gene expression is not yet known. However, the hybrid methodology does provide high spatial resolution strain maps of the intranuclear space that will allow for future investigation of these questions.

33.4.3 Detecting Nascent RNA Synthesis in Single Cells

Combining measurements of intranuclear mechanics with biosynthesis assays, e.g., detection of nascent RNAs, facilitates analysis of mechanoregulated gene expression within the nuclei of single cells. Nascent RNA detection has been measured in cells embedded in their native ECM[24] using a commercially available global RNA detection kit (Click-iT® RNA Alexa Fluor® 488 Imaging Kit, Invitrogen, Carlsbad, California).[39,40] In previous studies, the incubation for nascent RNA detection began immediately after the deformation and lasted for 60 min, and the sample was subsequently fixed for fluorescent labeling (Figure 33.4). In the cell population studied, the RNA was located in the lower intensity DNA regions, i.e., the interchromatin space, where the DNA is less densely packed and thought to be highly active for transcription.[24,30,41] The spatial location of RNA was typically correlated with the more compressive nuclear regions. However, the spatial correlation of mechanics and biosynthesis should be interpreted with caution because it was observed that RNA was also transported outside of the nucleus during the incubation period. In a control study, with no tissue scale deformation applied, there were fewer nuclei (26%) with detectable RNA synthesis compared to the deformed nuclei results (59%). The mechanism for why the nuclei in the mechanically strained tissue had more detectable RNA nuclei has not been explained, but it is nevertheless important to employ methods that allow for direct spatial correlation of intranuclear strain fields and RNA synthesis in nuclei to help elucidate pathways for gene expression in single cells.

33.4.4 Specificity and Experimental Tradeoffs

There is still a need to increase the specificity of hybrid microscopy and hyperelastic warping methods to reveal

biophysical and biosynthesis actions at even smaller spatial and temporal scales. Labeling of genes related to disease pathogenesis or tissue regeneration may allow for the discovery of local mechanical factors that can alter clinically relevant gene transcription. One challenge is the development of high (e.g., super) resolution imaging to better reveal spatial patterns while also not sacrificing temporal resolution of the desired response. For example, an experimental protocol that captures time-consuming high-resolution images of cell nuclei and fast calcium signaling is affected by competing spatiotemporal factors. Calcium fluxes can occur on the order of seconds to milliseconds, a time duration that is faster than the time required for image acquisition depicting nuclei at high resolution. In contrast, biosynthesis processes like RNA transcription can occur over longer time durations and may be more appropriately combined with higher-resolution imaging to simultaneously provide intranuclear strain fields (Figure 33.4 and Table 33.1). However, the localization of specific gene activity or gene products is not often resolved in living single cells,[36] and it is likely that biotechnology advances for gene expression profiling, coupled with hybrid microscopy, will only improve our understanding of mechanotransduction overall.

33.5 Conclusion

This chapter has demonstrated that a hybrid method combining optical microscopy and hyperelastic warping provides detailed intranuclear strain patterns and represents a balanced approach to meet the competing acquisition factors of spatial and temporal resolutions. The measurement of nascent RNA synthesis was a fundamental step to show that intranuclear mechanics and gene expression-related events can be measured within the same nucleus maintained in a native 3D microenvironment. As research objectives turn toward targeting specific genes or profiling of mRNA expression in single cells, new approaches will be developed and will be easily included for spatial correlation of strain fields measured by hyperelastic warping.

Acknowledgments

The authors gratefully acknowledge funding from the Andrews Fellowship and Hugh W. and Edna M. Donnan Fellowship (JTH).

References

1. Goldman, R. D., Gruenbaum, Y., Moir, R. D., Shumaker, D. K. and Spann, T. P. Nuclear lamins: Building blocks of nuclear architecture. *Genes and Development* **16**, 533–547 (2002). doi:10.1101/gad.960502.
2. Gerace, L. and Huber, M. D. Nuclear lamina at the crossroads of the cytoplasm and nucleus. *Journal of Structural Biology* **177**, 24–31 (2012). doi:10.1016/j.jsb.2011.11.007.
3. Li, Q. S. and Lim, C. T. Structure–mechanical property changes in nucleus arising from breast cancer. *Cellular and Biomolecular Mechanics and Mechanobiology* **4**, 465–475 (2011). doi:10.1007/8415_2010_19.
4. Aigner, T., Kurz, B., Fukui, N. and Sandell, L. Roles of chondrocytes in the pathogenesis of osteoarthritis. *Current Opinion in Rheumatology* **14**, 578–584 (2002). doi:10.1097/01.bor.0000022355.07263.81.
5. Hou, H. W. et al. Deformability study of breast cancer cells using microfluidics. *Biomedical Microdevices* **11**, 557–564 (2009). doi:10.1007/s10544-008-9262-8.
6. Chalut, K. J. et al. Chromatin decondensation and nuclear softening accompany Nanog downregulation in embryonic stem cells. *Biophysical Journal* **103**, 2060–2070 (2012). doi:10.1016/j.bpj.2012.10.015.
7. Chuang, C. H. and Belmont, A. S. Moving chromatin within the interphase nucleus-controlled transitions? *Seminars in Cell and Developmental Biology* **18**, 698–706 (2007). doi:10.1016/j.semcdb.2007.08.012.
8. Trinkle-Mulcahy, L. and Lamond, A. I. Nuclear functions in space and time: Gene expression in a dynamic, constrained environment. *FEBS Letters* **582**, 1960–1970 (2008). doi:10.1016/j.febslet.2008.04.029.
9. Martins, R. P., Finan, J. D., Guilak, F. and Lee, D. A. Mechanical regulation of nuclear structure and function. *Annual Review of Biomedical Engineering* **14**, 431–455 (2012). doi:10.1146/annurev-bioeng-071910.
10. Teperino, R., Lempradl, A. and Pospisilik, J. A. Bridging epigenomics and complex disease: The basics. *Cellular and Molecular Life Sciences* **70**, 1609–1621 (2013). doi:10.1007/s00018-013-1299-z.
11. Banerjee, B., Bhattacharya, D. and Shivashankar, G. V. Chromatin structure exhibits spatio-temporal heterogeneity within the cell nucleus. *Biophysical Journal* **91**, 2297–2303 (2006). doi:10.1529/biophysj.105.079525.
12. Bhattacharya, D., Talwar, S., Mazumder, A. and Shivashankar, G. V. Spatio-temporal plasticity in chromatin organization in mouse cell differentiation and during drosophila embryogenesis. *Biophysical Journal* **96**, 3832–3839 (2009). doi:10.1016/j.bpj.2008.11.075.
13. Talwar, S., Kumar, A., Rao, M., Menon, G. I. and Shivashankar, G. V. Correlated spatio-temporal fluctuations in chromatin compaction states characterize stem cells. *Biophysical Journal* **104**, 553–564 (2013).
14. Haudenschild, D. R. et al. Vimentin contributes to changes in chondrocyte stiffness in osteoarthritis. *Journal of Orthopaedic Research* **29**, 20–25 (2011). doi:10.1002/jor.21198.